LOW TEMPERATURE SYNTHESIS OF DENSE REACTION-BONDED-MULLITE VIA TRANSIENT LIQUID

LOW TEMPERATURE SYNTHESIS OF DENSE REACTION-BONDED-MULLITE VIA TRANSIENT LIQUID

By

HANSOO KIM, B. Eng., M. Eng.

A Thesis

Submitted to the School of Graduate Studies

in Partial Fulfillment of the Requirements

for the Degree

Master of Engineering

McMaster University

MASTER OF ENGINEERING (2001) McMASTER UNIVERSITY
(Materials Science and Engineering) Hamilton, Ontario, Canada

TITLE: Low Temperature Synthesis of Dense Reaction-Bonded-Mullite via Transient Liquid

AUTHER: HanSoo Kim, M. Eng. (Ajou University, Korea)
B. Eng. (Ajou University, Korea)

SUPERVISOR: Professor Patrick S. Nicholson

NUMBER OF PAGES: xv, 139

ABSTRACT

A near-net-shape process for the production of mullite matrix ceramic composites below 1300 °C has been achieved by reaction bonding Al_2O_3, silicon, mullite seeds and a eutectic of Al_2O_3-SiO_2-mixed rare earth oxide. The roles of the transient liquid phase from the eutectic and the mullite seeds are examined. The approximate eutectic composition was estimated from the Al_2O_3-SiO_2-Y_2O_3 phase diagram as 22 wt % Al_2O_3/46 wt% SiO_2/32 wt% Y_2O_3. The fusion temperature of the mixed-rare-earth-based eutectic composition was lower (1175 °C vs. those of pure, rare earth oxides based eutectic composition; $Pr_6O_{11}/Al_2O_3/SiO_2$: 1224 °C, $Eu_2O_3/Al_2O_3/SiO_2$: 1259 °C and $Y_2O_3/Al_2O_3/SiO_2$: 1345 °C).

The densification characteristics of the reaction-bonded mullite (RBM) mixture were investigated. Density increased with eutectic, and decreased with mullite seed contents. Oxidation and volume expansions due to Si and mullite formation are examined by thermogravimetric analysis (TGA) and dilatometric measurement. The measured weight gain and maximum volume expansion were lower than theoretical values due to preoxidation of the Si powder. Dilatometric curves indicated sintering shrinkage is compensated by the oxidation-induced volume-expansion. Al_2O_3 + SiO_2 mixtures of the mullite composition exhibited shrinkage exclusively.

X-ray diffraction of the RBM sinters display major mullite peaks and minor residual α-Al_2O_3. Mullite develops with low residual Al_2O_3 when 7.5 wt% mixed-rare-

earth-oxide eutectic and 5 wt% mullite seeds are incorporated into the mix. The final sinter is > 90 % theoretical density, > 90 % mullite, and suffers 2.2 % sintering shrinkage. Transmission-electron-microscopy (TEM) and Energy dispersive X-ray spectra (EDX) were employed to follow mullite evolution.

Model samples were utilised to study diffusion-, and reaction-, rates. The highest reaction rates at the lowest temperature occur when the eutectic penetrates an Al_2O_3/Si layer. Bimodal pellets with and without eutectic (or with and without mullite seeds) directly illustrate their roles. Mullite seeds promote mullite formation, but the transient liquid accelerates Si oxidation, mullite formation and densification.

ACKNOWLEGEMENTS

The author would like to thank and glorify God whom made this happen.

The author wishes to express his sincere gratitude to Prof. P. S. Nicholson for his ideas, guidance, support and encouragement during the course of this study. Thanks are also extended to Mrs. Ena Nicholson for her thoughtful, generous and kind help.

I would like to thank Prof. D. S. Wilkinson and Prof. A. Petric for their fruitful suggestions and constructive criticism of my work.

The help of Connie, Sarah, Frank, Klaus, Fred, Andy and Ed was invaluable and much appreciated.

Sincere thanks are extended to Dr. Patel, Dr. Kuo, Dr. De, Dr. Fukada, Dr. Scott, Yahua, Nanda, Ewa and Waleed in the Ceramic Research Group and Tony for their company, friendship and helpful discussion.

I would also like to thank my parents, brother and sister for their support and interest.

Special thanks to my wife, Hee Jung, for her love, support and encouragement throughout the course of this work including some hard times and to my kids, Eunice and Enoch, for their smiles.

TABLE OF CONTENTS

	Page
ABSTRACT	iii
ACKNOWLEGEMENTS	v
TABLE OF CONTENTS	vi
LIST OF FIGURES	ix
LIST OF TABLES	xv
CHAPTER 1. Introduction	1
CHAPTER 2. Literature Review	3
2-1 Mullite	3
2-1-1 The Crystal Structure of Mullite	5
2-1-2 The Phase Diagram of Al_2O_3-SiO_2 and the Mullite Solid Solution Range	8
2-1-3 Reaction Mechanisms in the Al_2O_3-SiO_2 System	8
2-2 The Reaction Bonding Process	12
2-2-1 Sintering Shrinkage	12
2-2-2 Reaction-Bonded Ceramics for Zero Sintering Shrinkage	13
2-2-3 Reaction-Bonded Mullite (RBM)	14
2-3 The Degradation of Nextel 720 Fibre above 1300 °C	22
2-4 The Si Powder Oxidation Process	25
2-5 Mixed Rare Earth Oxide Eutectic	33
2-6 Low-Temperature Eutectics in Al_2O_3/SiO_2/Rare Earth Oxide Mixture compositions	33
2-7 Liquid Phase Sintering	35
2-7-1 The Process of Liquid Phase Sintering	35
2-7-1-1 The Driving Force for Liquid Phase Sintering	37

2-7-1-2 Solid-Particle Rearrangement in the Presence of a Liquid-Phase 42
2-7-1-3 The Solution-Precipitation Process during Liquid-Phase Sintering 43
2-7-2 Sintering in the presence of a Transient Liquid Phase 44
2-7-2-1 The Base Dissolves the Additive 45
2-7-2-2 The Base Reacts with the Liquid Additive 49

CHAPTER 3. Experimental 51

3-1 Materials Preparation 51
3-1-1 The Eutectic 51
3-1-2 Premixing of the Al_2O_3 and Si Powders 52
3-2 The Synthesis of Reaction-Bonded Mullite 52
3-3 Interface Reaction Couples of the MREO Eutectic and Mixtures of Al_2O_3, Si (or SiO_2) 54
3-4 Bilayer Pellets to Identify the Roles of the Eutectic and Mullite Seeds 56
3-5 Material Characterization 58
3-5-1 Specific Surface Area 58
3-5-2 Thermal Analysis 58
3-5-3 Dimensional Change Measurement 58
3-5-4 Phase Determination 58
3-5-5 Electron Microscopy 59
3-5-6 The Morphology of the Interfacial Reaction 59
3-5-7 The Compositional Profile of the Reaction Layer 59

CHAPTER 4. Results and Discussion 60

4-1. Reaction-Bonded-Mullite 60
4-1-1. Eutectic of Al_2O_3-SiO_2-MREO 60
4-1-2. The Densification Characteristics of Mixed-Reare-Earth Based Reaction-Bonded Mullite (RBM) 65
4-1-3. The Oxidation Characteristics and Volume Expansion of the Mixed-Rare-Earth-Based, RBM Mixtures 68

4-1-4. Phase Evolution in the RBM Mixes 77
4-1-5. Transmission Electron Microscope Observations of the Reactions in RBM Mixes 81
4-2 Thermodynamic Analysis of the RBM Reactions 85
4-3 Liquid Diffusion and Liquid Reaction Studies 86
4-3-1. The Morphology of the Interface between the Eutectic and Mixtures of Al_2O_3, SiO_2 and Si 86
4-3-2. SEM and EDX Line Profile Analyses of the Reaction Layers 93
4-3-3. The Growth Rate of the Reaction Layer in the Bilayer Laminates 101
4-3-4. Exploration of the Reaction Sequences during the Reaction Bonding of Mullite 108
4-3. Definition of the Roles of the Eutectic and the Mullite Seeds in the RBM Process 111
4-3-1. Definition of the MREO Eutectic Role in the RBM Protocol 111
4-3-2. Definition of the Role of Mullite Seeds in the RBM Protocol 111
4-3-3. The Combined Role of the Eutectic and the Mullite seeds in the RBM Protocol 113
CHAPTER 5. Conclusions 116
REFERENCES 119
APPENDIX 131

LIST OF FIGURES

Page

Fig. 2-1. Geological map of Britain and Ireland. (The Isle of Mull in the northern highlands of Scotland is marked as a site of past volcanic activity. Because of a occurrence of the compound $3Al_2O_3 \cdot 2SiO_2$ on this island as a reaction product of clays, the compound was named "mullite"). 4

Fig. 2-2. Projection along [001] direction of the ideal unit cell of mullite showing T to T^* transition of the cations. 6

Fig. 2-3. Crystal structure of mullite. 7

Fig. 2-4. Phase diagram of Al_2O_3–SiO_2 system. 9

Fig. 2-5. Relationship between the concentration profile for aluminum of a semi-infinite SiO_2-Al_2O_3 diffusion couple and the phase equilibrium diagram at 1950 °C. 11

Fig. 2-6. Microstructures of diffusion zones in couples of sapphire (bottom) and fused silica, annealed at 1900 °C for 15 mins, (A) quenched (B) cooled at a moderate rate, and (C) cooled slowly. 11

Fig. 2-7. Quantitative estimates of phases present at various temperatures along heating cycle. 16

Fig. 2-8. Heat treatment cycles: (a) without, and (b) with, oxidation holds for the SiC. 16

Fig. 2-9. Phase compositions of samples SC30c (coarse SiC) and SC30f (fine SiC) after sintering. 17

Fig. 2-10. TEM micrographs showing composition SC30f after sintering at 1550 °C for 1 h (a) without and (b) with hold at 1150 °C for 10 h (M: mullite, A: Al_2O_3, S: SiC, Z: ZrO_2). 17

Fig. 2-11. Dimensional change, degree of oxidation and oxidation rate. 19

Fig. 2-12. XRD traces of metal alloy, ceramic and precursor powder after various milling schedules. 19

Fig. 2-13. XRD diagram of the AM35Z15 specimen after heat-treatment at 1100 °C for 20 hrs. 21

Fig. 2-14. XRD diagram of the AM35Z15 specimen after heat-treatment at 1580 °C for 2 hrs. 21

Fig. 2-15. Temperature-dependent weight-change curves of undoped and doped RBM samples. 23

Fig. 2-16. Temperature-dependent length-change curves of undoped and doped RBM samples. 23

Fig. 2-17. XRD patterns of undoped and doped RBM samples. 24

Fig.2-18. Strength vs. thermal exposure temperature for Nextel 720. 26

Fig. 2-19. Model for the oxidation of silicon. 27

Fig. 2-20. Oxidation of silicon in wet oxygen (95 °C H_2O). 31

Fig. 2-21. Oxidation of silicon in dry oxygen (760 Torr). 31

Fig. 2-22. Evaluation of the rate constants for Si oxidation in wet oxygen (95 °C H_2O). 32

Fig. 2-23. Evaluation of the rate constants for Si oxidation in dry oxygen (760 Torr). 32

Fig. 2-24. Phase diagram of the Al_2O_3-SiO_2-Y_2O_3 system. 36

Fig. 2-25. The classic stages of liquid phase sintering. 38

Fig. 2-26.Spherical particles held together by liquid capillary pressure. 38

Fig. 2-27. Two spheres with pendular liquid ring and definition of variables. 40

Fig. 2-28. Two binary phase diagrams which could form the basis for transient liquid. 46

Fig. 2-29. An example of the heating rate effect on transient liquid phase sintering. 46

Fig. 2-30. SEM photography of the intermetallic envelope formed around an Al particle in an Fe-Al powder compact heated to 635 °C. 48

Fig. 2-31. A binary phase diagram for reactive liquid phase sintering of the AB compound from mixed A and B powder. 48

Fig. 2-32. Typical sequence of events in reactive sintering. 48

Fig. 3-1. Heat treatment cycles of reaction bonded mullites. 55

Fig. 3-2. The configurations of the stacked specimens. 55

Fig. 3-3. Schematic diagram of the vacuum impregnation. 57

Fig. 3-4. The configurations of bimodal pellets. 57

Fig. 4-1. Differential thermal analysis and thermogravimetric analysis curves for eutectic composition of Al_2O_3-SiO_2-Pr_6O_{11} system. 62

Fig. 4-2. Differential thermal analysis and thermogravimetric analysis curves for eutectic composition of Al_2O_3-SiO_2-Eu_2O_3 system. 63

Fig. 4-3. Differential thermal analysis and thermogravimetric analysis curves for eutectic composition of Al_2O_3-SiO_2-MREO system. 64

Fig. 4-4. Density and shrinkage vs. sintering temperature for RBM mixtures1-4. 66

Fig. 4-5. Density and shrinkage vs. sintering temperature for RBM mixtures 5-9. 67

Fig. 4-6. Thermogravimetric analysis (TGA) for RBM 1-4 Samples. 69

Fig. 4-7. Thermogravimetric analysis (TGA) for RBM 5-9 Samples. 70

Fig. 4-8. Dilatometric measurement curves of RBM 1-4 samples (The straight line segment plot is the time/temperature profile of the apparatus, Dotted box is shown in Fig. 4-10). 73

Fig. 4-9. Dilatometric measurement curves of RBM 5-9 samples (The straight line segment plot is the time/temperature profile of the apparatus). 74

Fig. 4-10. Shrinkage vs. $t^{1/3}$ plots of RBM 1-4 samples. 76

Fig. 4-11 X-ray diffraction patterns of RBM 2 Samples quenched from the indicated temperatures (■: Mullite, ◉: α-Al_2O_3, △: Cristobalite). 78

Fig. 4-12. X-ray diffraction patterns of RBM 1-4 samples after heating at 1300°C for 5 hrs (■: Mullite, ◉: α-Al_2O_3, △: Cristobalite). 79

Fig. 4-13. X-ray diffraction patterns of RBM 5-9 samples after heating at 1300°C for 5 hrs (■: Mullite, ◉: α-Al_2O_3, △: Cristobalite, ◇: REO). 80

Fig. 4-14. Transmission electron micrographs of samples quenched at (a) 1250°C (inset electron diffraction pattern of Al_2O_3/mullite), (b) 1270°C, (c) 1290°C, and (d) RBM sample sintered at 1300°C for 5 hrs (inset electron diffraction pattern of mullite). 82

Fig. 4-15. Transmission electron micrograph of RBM 2 sample sintered at 1300°C for 5 hrs. 83

Fig. 4-16.The reaction interface between eutectic composition (top) and Al_2O_3 + SiO_2 (S1) (bottom) or Al_2O_3 + Si (S2) (bottom) after heating at 1250 °C for indicated time (Diffusion layer arrowed). 88

Fig. 4-17. The reaction interface between eutectic composition (top) and Al_2O_3 + SiO_2 (S1) (bottom) or Al_2O_3 + Si (S2) (bottom) after heating at 1300 °C for indicated time (Diffusion layer arrowed). 89

Fig. 4-18. The reaction interface between eutectic composition (top) and Al_2O_3 + SiO_2 (S1) (Bottom) or Al_2O_3 + Si (S2) (Bottom) after heating at 1350 °C for indicated time (Diffusion layer arrowed). 90

Fig. 4-19. The reaction interface between eutectic composition (top) and Al_2O_3 + SiO_2 (S1) (Bottom) or Al_2O_3 + Si (S2) (Bottom) after heating at 1400 °C for indicated time (Pt particles arrowed). 92

Fig. 4-20. SEM micrographs of interlayer heat-treated at 1300 °C for 90 mins. in (a) S1, (b) S2, (c) S3 and (d) S4 94

Fig. 4-21. SEM micrographs and corresponding elemental profiles for Al, Si, La, Ce for the interlayer heat-treated at 1300 °C for 90 mins. in (a) S1, (b) S2, (c) S3 and (d) S4 97

Fig. 4-22.The penetration of liquid phase at 1250 °C into each sample. 102

Fig. 4-23.The penetration of liquid phase at 1300 °C into each sample. 103

Fig. 4-24.The penetration of liquid phase at 1350 °C into each sample. 104

Fig. 4-25.The penetration of liquid phase at 1400 °C into each sample. 105

Fig. 4-26. Diffusivity of liquid phase in each sample with temperature. 107

Fig. 4-27. Schematic of the reaction sequence of RBM via Al_2O_3/Si/eutectic composition with mixed rare earth oxide, and mullite seeds. 109

Fig. 4-28. X-ray diffraction patterns (a) Al_2O_3 + Si and (b) Al_2O_3 + Si + eutectic layers after heating at 1300°C for 5 hrs (■: Mullite, ◉: α-Al_2O_3, △: Cristobalite, ◆: Si, ◇: REO). 112

Fig. 4-29. X-ray diffraction patterns (a) Al_2O_3 + Si, (b) Al_2O_3 + Si + mullite seeds after heating at 1300°C for 5 hrs and (c) Ground (a) + mullite 114

seeds (■: Mullite, ◉: α-Al_2O_3, △: Cristobalite, ◆: Si).

Fig. 4-30. X-ray diffraction patterns (a) Al_2O_3 + Si + mullite seeds and (b) Al_2O_3 + Si + eutectic + mullite seeds layers after heating at 1300°C for 5 hrs (■: Mullite, ◉: α-Al_2O_3, △: Cristobalite). 115

Fig. C-1. The reaction interface between eutectic composition (top) and Al_2O_3 + SiO_2 (S1) (Bottom) or Al_2O_3 + Si (S2) (Bottom) after heating at 1175 °C for indicated time (Diffusion layer arrowed). 134

Fig. C-2. The reaction interface between eutectic composition (top) and Al_2O_3 + SiO_2 (S1) (Bottom) or Al_2O_3 + Si (S2) (Bottom) after heating at 1200 °C for indicated time (Diffusion layer arrowed). 135

Fig. C-3. The reaction interface between eutectic composition (top) and Al_2O_3 + SiO_2 + seeds (S3) (Bottom) or Al_2O_3 + Si + seeds (S4) (Bottom) after heating at 1250 °C for indicated time (Diffusion layer arrowed). 136

Fig. C-4. The reaction interface between eutectic composition (top) and Al_2O_3 + SiO_2 + seeds (S3) (Bottom) or Al_2O_3 + Si + seeds (S4) (Bottom) after heating at 1300 °C for indicated time (Diffusion layer arrowed). 137

Fig. C-5. The reaction interface between eutectic composition (top) and Al_2O_3 + SiO_2 + seeds (S3) (Bottom) or Al_2O_3 + Si + seeds (S4) (Bottom) after heating at 1350 °C for indicated time (Diffusion layer arrowed). 138

Fig. C-6.The reaction interface between eutectic composition (top) and Al_2O_3 + SiO_2 + seeds (S3) (Bottom) or Al_2O_3 + Si + seeds (S4) (Bottom) after heating at 1400 °C for indicated time (White line is Pt foil, Diffusion layer arrowed). 139

LIST OF TABLES

	Page
Table 2-1 The properties of Nextel 720	26
Table 2-2 The distribution oxides in mixed rare earth oxide	34
Table 2-3 Invariant points of the system Y_2O_3-Al_2O_3-SiO_2	36
Table 3-1 Chemicals used in the project	53
Table 3-2 Chemical compositions of RBM mixtures explored	53
Table 3-3 The oxide compositions of the top and bottom layer of the layered pellets	55
Table 3-4 The compositions of the layers in bimodal pellets	57
Table 4-1 Differences between theoretical and observed weight gains	71

CHAPTER 1

Introduction

Mullite ($3Al_2O_3 \cdot 2SiO_2$) is an important high temperature structural material with excellent high-temperature stability, strength, low thermal expansivity and high creep-, and thermal-shock-, resistance. Thus it is an ideal matrix for continuous, fibre-reinforced, oxide/oxide ceramic composites for structural applications at elevated temperatures such as thermal protection of combustion chambers in aircraft- and stationary- gas turbines.

Sintering-induced shrinkage in a composite with a volume-stable dispersant/ sintering-powder-matrix, results in component shape distortion and cracking. The non-shrinkage of the dispersed-phase limits densification and induces residual stresses. Therefore, mullite-fiber reinforced, mullite-matrix composites suffer fiber damage and matrix cracking during sintering because the matrix shrinks and the fibres do not.

Reaction bonding is a potential solution to this sintering shrinkage problem. Near-zero-shrinkage, monolithic mullite (0.11 % shrinkage) has been made by reaction bonding. Reaction bonding involves a competing shrinkage/expansion protocol wherein one component of the sintering (shrinking) mixture is simultaneously oxidising (expanding).

Conventional reaction bonded mullites are sintered $\approx$ 1500 °C, but these temperatures are too high for commercial mullite-fibre such as the newly-developed

Nextel 720. Degradation thereof above 1300 °C is abrupt so processing temperatures involving it in a composite must be less than 1300 °C.

Recently, reaction-bonded-mullite was sintered at 1350 °C by including Y_2O_3 or CeO_2 to induce the rare-earth-oxide/Al_2O_3/SiO_2, low temperature eutectic in the sintering mixture. 1350 °C is still too high for Nextel 720, but this use of a rare-earth oxide eutectic pointed the way for the present work.

This thesis concerns development of a reaction-bonding protocol for sintering mullite to > 90 % theoretical density and > 90 % mullite, at temperatures below 1300 °C.

CHAPTER 2

Literature Review

2-1 Mullite

Mullite ($3Al_2O_3 \cdot 2SiO_2$) is a strong candidate for advanced structural applications at high temperatures because it has high strength at high temperature, low thermal expansion, good chemical stability and high creep and thermal shock resistance (Schneider et al. 1994). These properties make mullite one of the most important materials in ceramic science and technology.

Oschartz and Wächter (1847) interpreted the crystallization processes in the glassy phase of porcelains as the formation of acicular sillimanite. Sillimanite-like crystals with formula $11Al_2O_3 \cdot 8SiO_2$ were described by Vernadsky (1890). Shepherd et al. (1909) published the first phase diagram of the Al_2O_3-SiO_2 system. They believed sillimanite ($Al_2O_3 \cdot SiO_2$) was the single binary compound. Bowen and Greig (1924) pointed out that the stable aluminum-silicate compound had a 3:2 ($3Al_2O_3 \cdot 2SiO_2$) ratio rather than 1:1 ($Al_2O_3 \cdot SiO_2$) and Bowen named this 3:2 aluminum silicate, "mullite" because crystals of the same compound exist exclusively in the natural rocks of the Island of Mull (Fig. 2-1).

Fig. 2-1. Geological map of Britain and Ireland. (The Isle of Mull in the northern highlands of Scotland is marked as a site of past volcanic activity. Because of a occurrence of the compound $3Al_2O_3 \cdot 2SiO_2$ on this island as a reaction product of clays, the compound was named "mullite") (Aksay et al. 1991).

2-1-1 The Crystal Structure of Mullite

Mullite is a defect sillimanite, $Al_2O_3 \cdot SiO_2$ (Aksay et al. (1991)). The mullite stoichiometry is achieved by substituting Al^{3+} for Si^{4+} on the tetrahedral sites of alternating aluminum-oxygen columns in sillimanite. This compositional variation leads to composition-dependent oxygen vacancies (□), ie;

$$2Si^{4+} + O^{2-} \rightarrow 2Al^{3+} + \square$$

The crystal structure is orthorhombic with general formula $Al_{4+2x}\ Si_{2-2x}\ O_{10-x}$ where x is the number of possible oxygen atoms missing per average unit cell. x varies between 0.17 and 0.59 (Cameron (1977)). When x=0, the composition represents the three polymorphic modifications sillimanite, andalusite, and kyanite (Al_2SiO_5), which are partially related to mullite in terms of structure. x = 1 is the chemical composition of the ι-Al_2O_3 phase (Saalfeld (1962)). x = 0.25 for 3:2 mullite.

In the structure (Fig. 2-2), chains of aluminum oxygen octahedra with common oxygen-oxygen edges run parallel to the c axis. The octahedra are linked by double chains of aluminum-oxygen and silicon tetrahedra in random sequence (Burnham (1964)). The tetrahedral chains of mullite are disturbed such that some pairs of tetrahedra are misorientated with removal of some oxygen at the c site (O(c)) (see Figure 2-2) from the structure. So two adjacent tetrahedral (T-cation) sites are displaced to T* positions. Substitutional replacement of tetrahedral silicon by aluminum also takes place, as shown in Fig 2-2. The crystal structure of mullite is stereographically simulated in Fig. 2-3. The structure is such the macroscopic crystals are acicular (needle-like).

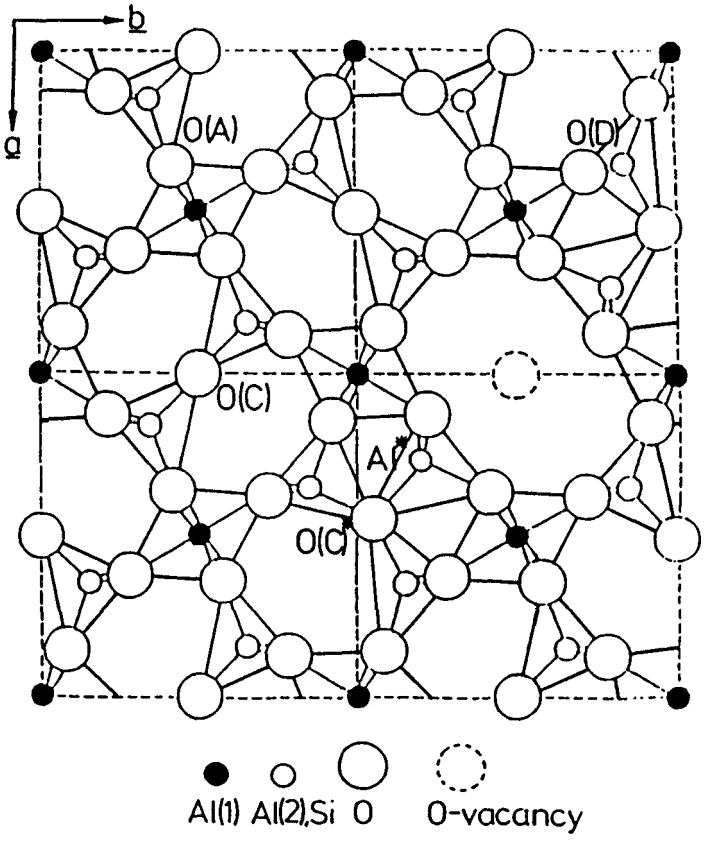

Fig. 2-2. Projection along [001] direction of the ideal unit cell of mullite showing T to T^* transition of the cations (Schneider 1990).

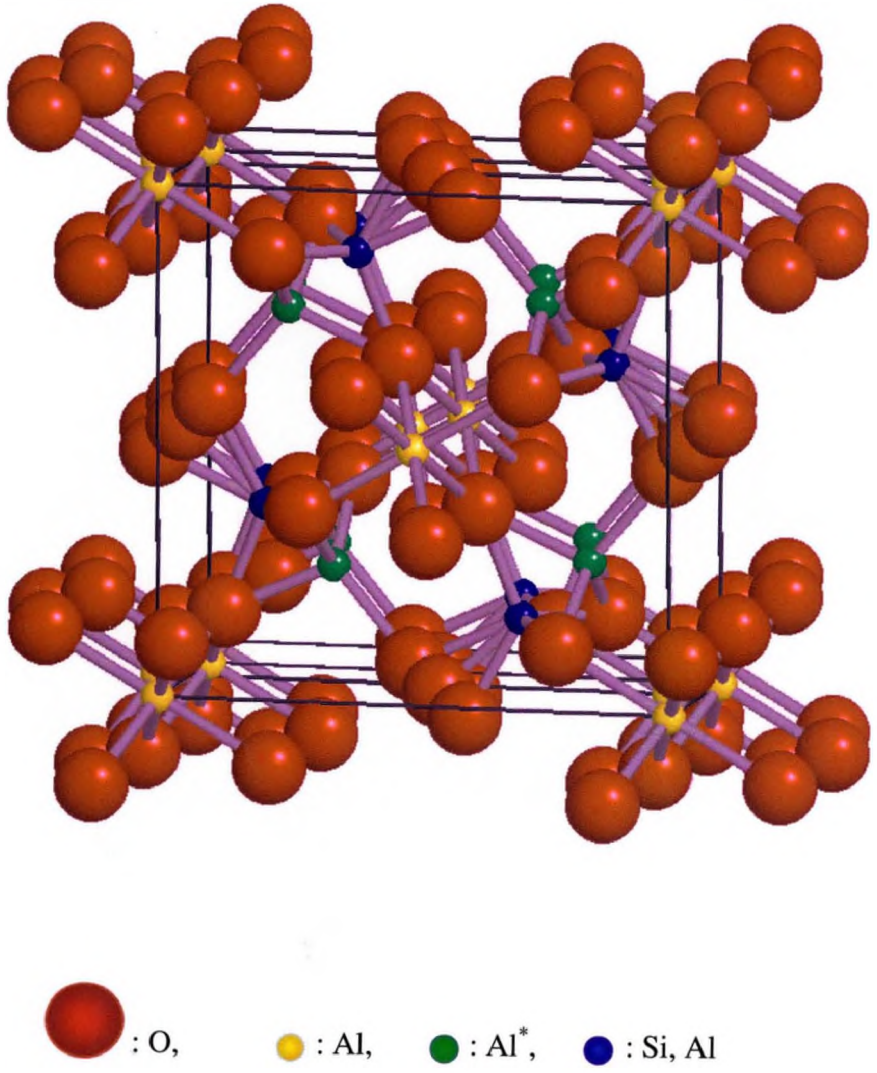

Fig. 2-3. Crystal structure of mullite (simulated by Xtaldraw).

2-1-2 The Phase Diagram of Al_2O_3-SiO_2 and the Mullite Solid Solution Range

Mullite is the solitary compound in the Al_2O_3-SiO_2 system (Fig 2-4) (Aksay and Pask (1974) (1975)). Stable mullite has a 3:2 (Al_2O_3-SiO_2) composition instead of a 1:1 (Al_2O_3-SiO_2) under normal atmospheric pressure. The eutectic between mullite and cristobalite occurs at 1587 °C to give liquid containing ≅ 95 mol% SiO_2. The peritectic (Al_2O_3 + L → mullite) occurs at 1828 °C.

This Al_2O_3-SiO_2 phase diagram is controversial vis à vis the congruent or incongruent melting of mullite. Aramaki and Roy (1962) published a diagram with mullite congruently melting with a solid solution range, 71.8-74.3 wt% Al_2O_3. Davis and Pask (1972) determined the solid solution range of mullite to be 71.0-74.0 w/o Al_2O_3 with an incongruent melting point. Prochazka and Klug (1983) published a diagram with congruent melting and a solid solution range shifted to higher Al_2O_3 contents. Klug et al. (1987) modified the location of the Al_2O_3 liquidus sufficiently to result in incongruent melting of the mullite.

In the present study, mullite formation must be induced below 1300 °C due to the limited stability of the fibres it is required to encapsulate. The Al_2O_3-SiO_2 phase diagram at low temperatures is featureless.

2-1-3 Reaction Mechanisms in the Al_2O_3-SiO_2 System

The reaction between corundum (Al_2O_3) and cristobalite (SiO_2) in mixtures has

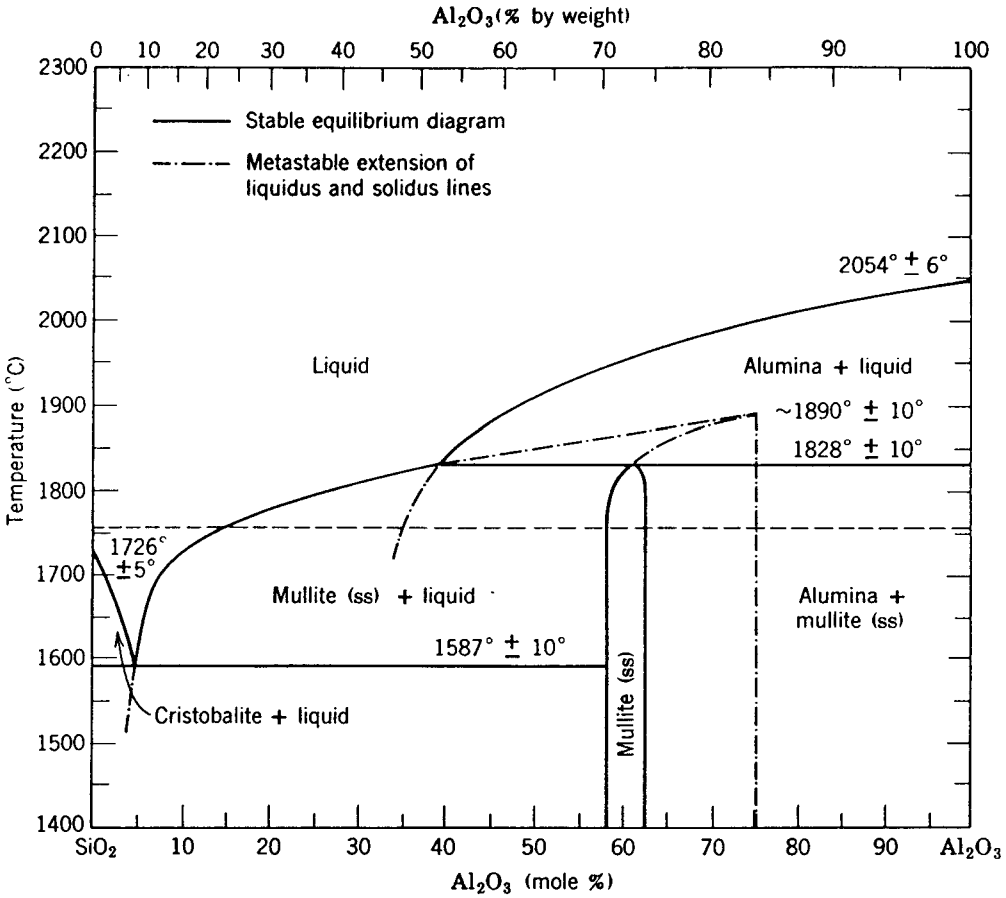

Fig. 2-4. Phase diagram of Al_2O_3–SiO_2 system (Aksay and Pask 1974).

been studied extensively. Though mullite can be formed by various synthesis methods involving additives, all mullite synthesis must be based on the reaction of Al_2O_3 and SiO_2.

De keyser (1965) studied reactions between Al_2O_3 and SiO_2 at high temperature by examining the contact surfaces between SiO_2 and Al_2O_3 pellets. He found a liquid phase forms around the cristobalite grains and this SiO_2-rich liquid penetrates the Al_2O_3 pellet. The liquid phase initiates mullite formation on penetration. Staley and Brindley (1969) studied the reaction at 1500 °C and 1550 °C using pressed pellets of cristobalite in contact with single crystals or pressed pellets of Al_2O_3 and concluded the formation of an amorphous phase was essential to the reaction.

Davis and Pask (1972) wrote the failure of nucleated mullite to grow to an observable thickness at lower temperatures is because its growth rate is slower than its dissolution rate in the SiO_2 liquid. Staley and Brindley (1969) showed that mullite growth does not occur until the liquid phase is saturated with Al_2O_3.

Schneider et al (1994) discussed the solid-state reaction mechanism at the interface of an α-Al_2O_3/SiO_2 diffusion couple. SiO_2 dissolves Al_2O_3 (see Al_2O_3 composition profile Fig 2-5) (Aksay and Pask 1975). The driving force is a reduction of the internal free energy of the fused SiO_2 (glass) as Al_2O_3 molecules are incorporated into the liquid's atomic structure. Al_2O_3 enters by breaking bonds. Summations of the step reactions are;

$$SiO_2 + x\ Al_2O_3 \rightarrow SiO_2 \cdot x\ Al_2O_3 \qquad -\Delta G_I$$

$$\alpha\text{-}Al_2O_3 \rightarrow x\ Al_2O_3 + (1\text{-}x)\ \alpha\text{-}Al_2O_3 \qquad +\Delta G_{II}$$

$$\text{Net: } SiO_2 + \alpha\text{-}Al_2O_3 \rightarrow SiO_2 \cdot x\ Al_2O_3 + (1\text{-}x)\ \alpha\text{-}Al_2O_3 \qquad \Delta G^*$$

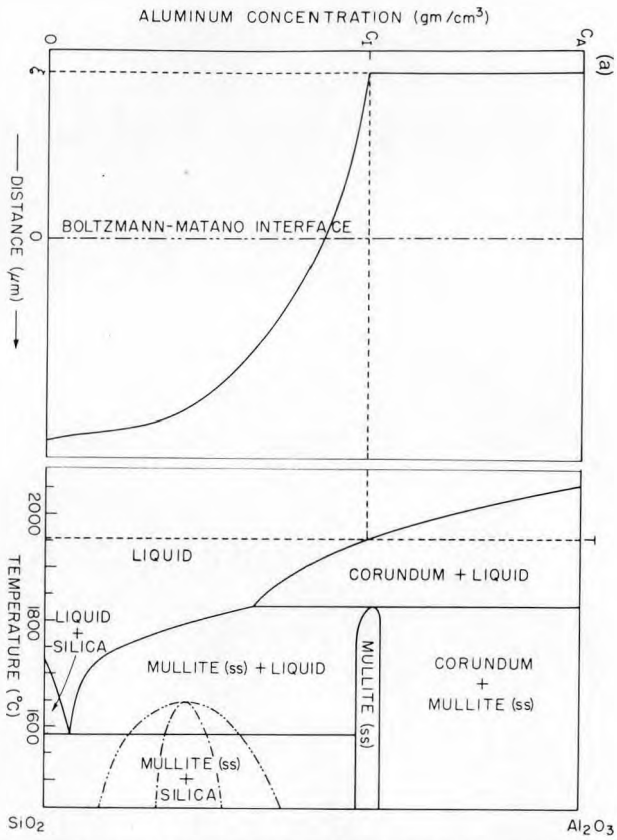

Fig. 2-5. Relationship between the concentration profile for aluminum of a semi-infinite SiO_2-Al_2O_3 diffusion couple and the phase equilibrium diagram at 1950 °C (Schneider et al. 1994).

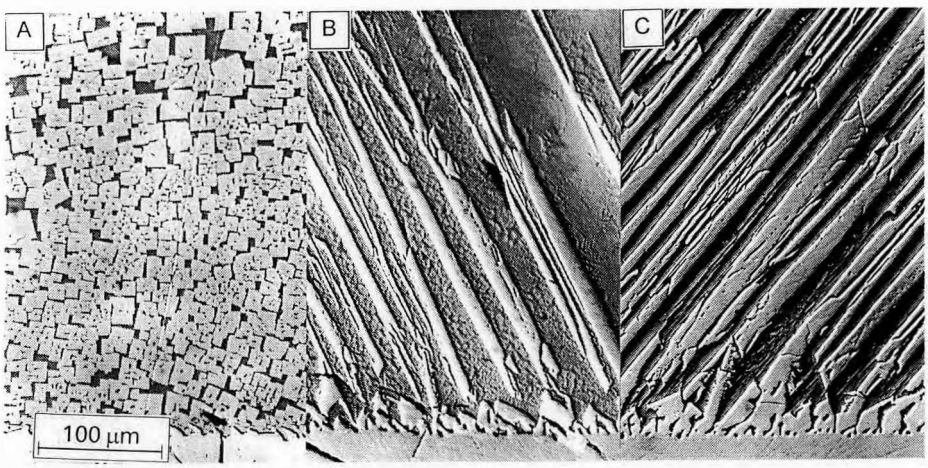

Fig. 2-6. Microstructures of the diffusion zones in couples of sapphire (bottom) and fused silica, annealed at 1900 °C for 15 mins., (A) quenched, (B) cooled at a moderate rate, and, (C) cooled slowly (Aksay and Pask 1975).

If $\Delta G_I > \Delta G_{II}$, the net ΔG^* is negative and the reaction will proceed, that is, the energy released as the Al_2O_3 is absorbed into the silica liquid structure is sufficient to dissociate the α-Al_2O_3. If $\Delta G_I < \Delta G_{II}$, the reaction will not proceed because ΔG^* is positive. When $\Delta G_I = \Delta G_{II}$, $\Delta G^* = 0$, the total Al_2O_3 dissolved into the silica is the equilibrium amount relative to α-Al_2O_3. Aksay and Pask (1975) showed the importance of the cooling rate of specimens from high temperature. Diffusion couples of sapphire and fused silica were heated together at 1900 °C for 15 min., then cooled by turning off the furnace and flowing He gas. Fig 2-6 shows polished cross sections of the three specimens (Sapphire is along the base of the micrographs). Fig 2-6 (a), which was quenched, shows precipitates of mullite in the liquid. Micrograph (c), which was cooled the slowest, shows the precipitates of Al_2O_3. Micrograph (b), which was cooled at an intermediate rate, shows large mullite precipitates with small crystals of α-Al_2O_3 in the glass phase.

2-2 The Reaction Bonding Process

2-2-1 Sintering Shrinkage

Strong, dense ceramics are made by sintering powders. The sintering process changes grain size and shape and eliminates pores. The driving force for sintering is the free-energy change that accompanies decrease in system surface area by elimination of

solid-vapor interfaces. Therefore, sintering is accompanied by shrinkage. This shrinkage changes the dimension of initially "green" samples. This shrinkage is a serious problem in composites including components with different shrinkage characteristics, i.e.; the shrinkage introduces residual stresses. This is especially the case for fiber-reinforced, ceramic-matrix composites. These suffer matrix cracking or fiber damage because, during fabrication, the fibres are rigid and the matrix shrinks. Therefore intensive efforts have been made to develop protocols for zero-shrinkage, i.e., "near-net-shape," processing capability.

2-2-2 Reaction-Bonded Ceramics for Zero Sintering Shrinkage

"Reaction-bonding," is a process of powder densification that involves concurrent sintering and chemical reaction.

Haggerty and Chiang (1990), Chiang et al. (1989) and Claussen et al. (1989), (1990) developed reaction-bonded ceramics with low sintering shrinkage. The latter is associated with coincident volume increase during nitridation, carbonization or oxidation of one component of the mix. These expansile processes counter sintering shrinkage.

The reaction bonding of aluminum oxide (RBAO) was the first system extensively studied (Wu et al. (1991), (1992), (1993), Holz et al. (1994), Claussen et al. (1991), (1994), (1995)). Al, Al_2O_3 and ZrO_2 (for toughness) were mixed, the Al level determined to give balancing oxidation expansion. The dimensional change between the green and

fully reaction-bonded states depends on the Al/Al_2O_3 ratio, the green density and the heating cycle.

The RBAO process proceeds by solid/gas and liquid/gas reactions. The reaction rate is controlled by oxygen diffusion and follows a parabolic relationship. It also depends strongly on the Al particle size. Claussen and coworkers (Wu and Claussen (1991), (1994), Holz et al. (1996), Lathabai et al. (1996), and Scheppokat et al. (1998), (1999)) extended RBAO technology to other ceramics.

2-2-3 Reaction-Bonded Mullite (RBM)

Lathabai et al. (1996) examined the fabrication of dense, low shrinkage, mullite/ZrO_2 composites, based on Al, Al_2O_3 and zircon. It is reported that mullite can be toughened by incorporation of ZrO_2 particles so Lathabai et al. and others used zircon to produce ZrO_2 and SiO_2 (Pena et al. (1983), Orange et al. (1985), Srikrishna et al. (1988), Leriche et al. (1988), Boch and Giry (1985), (1990), Prochazka et al. (1983), De Portu (1984), Moya and osendi (1983), (1984), Rincon et al. (1987), Ismail et al. (1988), Rundgren et al. (1990), Kamiaka et al (1990), Shiga et al (1991), Kubota et al (1994), and Koyama et al. (1994)). Al oxidizes to Al_2O_3 which reacts with the zircon to give mullite/ZrO_2 composites (Claussen and Jahn (1980), Di Rupo and Anseau (1980), Wallace et al. (1984)). The reactions are;

$$4\ Al + 3\ O_2 \rightarrow 2\ Al_2O_3$$

$$3\ Al_2O_3 + 2\ ZrSiO_4 \rightarrow 3\ Al_2O_3\ 2SiO_2 + 2\ ZrO_2.$$

A low heating rate (1 °C/min) was used to 1100 °C, then 10 °C/min to 1550 °C, followed by a hold for 2 hrs. The amount of zircon, α-Al_2O_3, mullite and total ZrO_2 (the sum of t- and m-ZrO_2) are plotted in Fig 2-7 as a function of the temperature of extraction. The first traces of mullite appear at 1400 °C and it increases to 20 w/o at 1450 °C, 31 w/o at 1475 °C and 63.5 w/o at 1500 °C. Concomitant is the zircon and α-Al_2O_3 decrease and ZrO_2 increase. The latter indicates zircon dissociation and mullite formation are proceeding. Traces of zircon remain at 1500 °C. The final product is 63.8 w/o mullite, 30.7 ZrO_2 and 5.5 w/o α-Al_2O_3, with 8 % shrinkage.

Holz et al. (1996) fired Al, Al_2O_3, SiC and ZrO_2 (included to induce toughness) at 1550 °C for 1 h. The Al oxidizes to Al_2O_3 at 300-900 °C, and thereafter SiC converts to SiO_2 (900-1200°C). Products react to form mullite ($3Al_2O_3 \cdot 2SiO_2$) above 1400 °C with the following reactions;

$$4\,Al + 3\,O_2 \rightarrow 2\,Al_2O_3 \qquad (300\text{-}900\ ^\circ C)$$

$$2\,SiC + 5\,O_2 \rightarrow 2\,SiO_2 + CO \qquad (900\text{-}1200^\circ C)$$

$$3\,Al_2O_3 + 2\,SiO_2 \rightarrow 3Al_2O_3 \cdot 2SiO_2 \qquad (> 1400\ ^\circ C)$$

The heating cycle utilised is shown in Fig 2-8. It includes steps for Al oxidation (slow heating 400 °C to 800 °C), SiC oxidation (dwell at 1150 °C) and final densification (dwell at 1550 °C). Though sintered under the same conditions, the % mullite produced is a function of initial particle size and heating schedule, i.e. samples with fine-particles develop more mullite and samples held at 1150 °C form more mullite (Fig. 2-9).

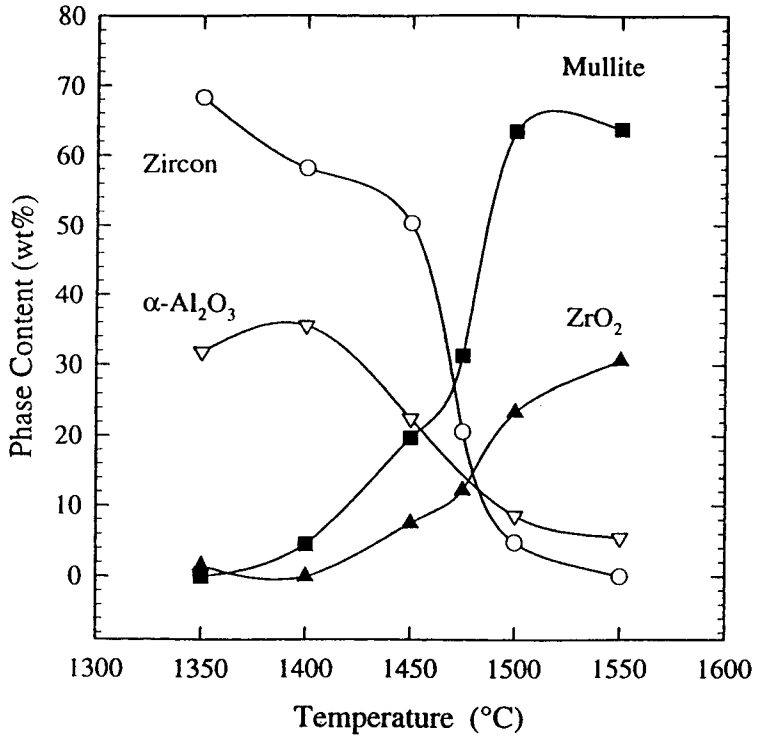

Fig. 2-7. Quantitative estimates of phases present at various temperatures along heating cycle (Lathabai et al. 1996).

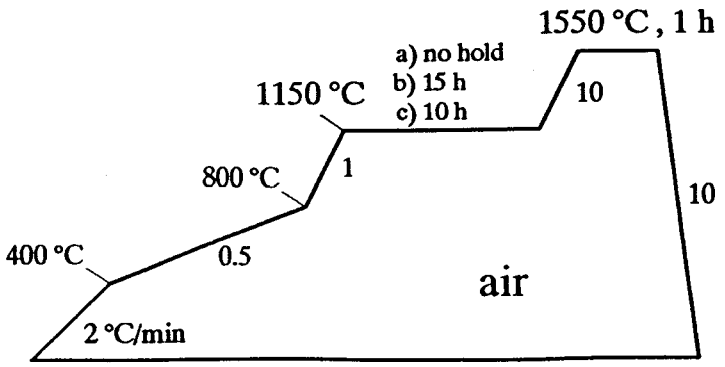

Fig. 2-8. Heat treatment cycles: (a) without, and (b) with, oxidation holds for the SiC (Holz et al. 1996).

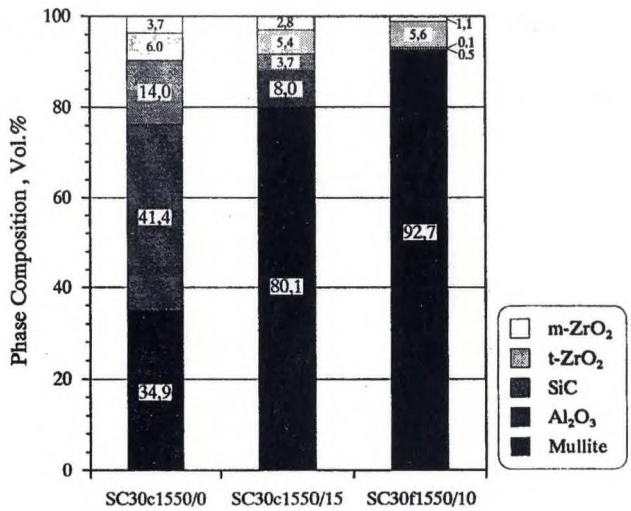

Fig. 2-9. Phase compositions of samples SC30c (coarse SiC) and SC30f (fine SiC) after sintering (SC30c1550/0, SC30c stands for coarse SiC 30 vol%, 1550 means sintering temperature, 0 is the dwell period at 1150 °C) (Holz et al. 1996).

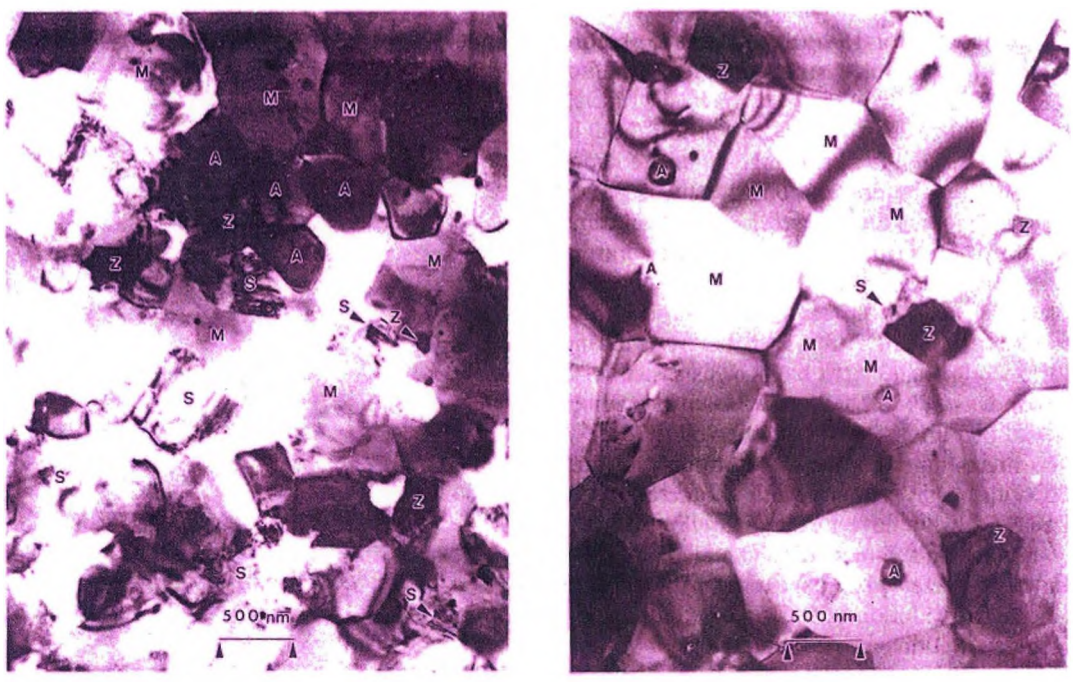

(a) (b)

Fig. 2-10. TEM micrographs showing composition SC30f after sintering at 1550 °C for 1 h (a) without and (b) with hold at 1150 °C for 10 h (M: mullite, A: Al_2O_3, S: SiC, Z: ZrO_2 (Holz et al. 1996).

Fig. 2-10 shows the microstructural difference between 'no' hold and hold at 1150 °C (for SiC oxidation). The latter develops the most mullite because the SiC has oxidized (Fig 2-10(b)). The density of this mullite/ZrO_2 sample is higher (96 %TD) than that shown in Fig. 2-10(a) (94.5 %TD). This increase is due to residual SiC which hinders the fast densification of the Al_2O_3 (Nakahira and Niihara (1992), Stearns et al. (1992)). The overall shrinkage of the sample is shown in Fig 2-10(b) and is 0.6 %. Scheppokat et al. (1998) further evolved this system to a final product with 94.6 %TD, 0.11 % sintering shrinkage and a strength of 250 MPa. The latter is lower than that of mullite, even with ZrO_2, however the shrinkage is very close to zero.

Brandt and Lundberg (1996) attempted to produce RBM from an Al-Si alloy, mullite seeds, Al_2O_3 and MgO sintered at 1430-1600 °C for 1 h. The dimensional change, oxidation rate, and heating schedule are shown in Fig 2-11. The slow heating rate (2 °C/min) provides oxidation with no temperature holds (see bottom graph). The oxidation rate data show two Al-oxidation and one Si-oxidation peaks. The degree of oxidation markedly increases around the oxidation peak. Dilatometric analysis is consistent therewith. The final volume change is + 3% (80.2 %TD).

Saruhan et al. (1996) employed an Al-Si alloy, Al_2O_3, Si and mullite precursors in their RBM protocol. They sintered greenware at 1500 °C for 1 h. The heating rate was 5 °C/min with holds at 900 °C for 5h, 1200 °C for 5 h, and 1500 °C for 1h. These steps promoted volume oxidation of the Al and Si particles and the reaction bonding process, respectively.

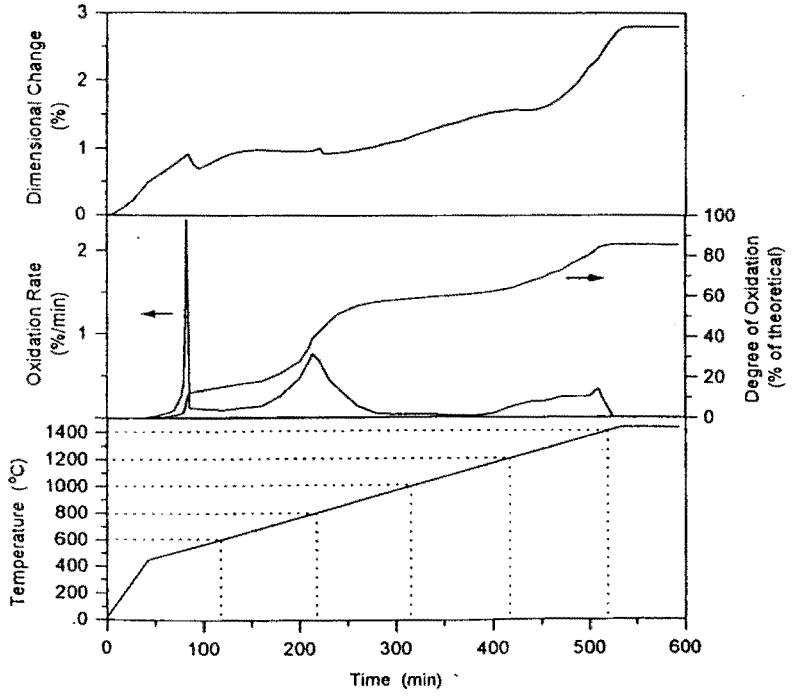

Fig. 2-11. Dimensional change, degree of oxidation and oxidation rate (Brandt and Lundberg 1996).

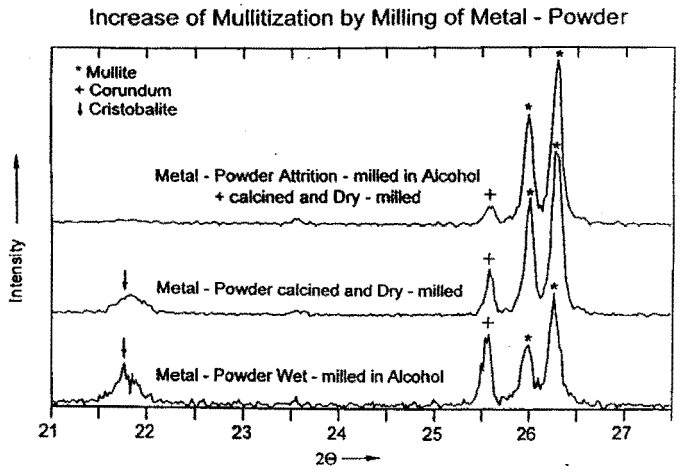

Fig. 2-12. XRD traces of metal alloy, ceramic and precursor powder after various milling schedules (Saruhan 1996).

Mullitization differed with the type of milling employed (Fig. 2-12), i.e.; attrition milling and reaction bonding at 1500 °C, produced high mullite (84 %) with low residual corundum (16 %) whereas dry-, and wet-milling gave lower mullite/corundum ratios and remnant cristobalite.

She et al. (2001) developed high density RBM using Al, Al_2O_3, SiC and ZrO_2. Samples were heat-treated at 1100 °C for 20 hrs to oxidise the SiC and the X-ray diffraction trace is shown in Fig. 2-13. No Al or SiC peaks appear indicating Al and SiC have almost completely oxidized. The absence of SiO_2 peaks suggests the oxidation-derived SiO_2 is amorphous. The possible oxidation reactions are;

$$4\ Al + 3\ O_2 \rightarrow 2\ Al_2O_3$$

$$SiC + 2\ O_2 \rightarrow SiO_2 + CO_2.$$

The specimen was further heated to 1500 °C for 2 hrs after which substantial mullite and trace of zircon were detected (Fig. 2-14). The formation of zircon is the result of reaction between ZrO_2 and SiO_2;

$$ZrO_2 + SiO_2 \rightarrow ZrSiO_4.$$

This zircon can further react with Al_2O_3 to form mullite (Scheppokat (1999));

$$2\ ZrSiO_4 + 3\ Al_2O_3 \rightarrow 3Al_2O_3{\cdot}2SiO_2 + 2\ ZrO_2.$$

The final density attained was 97.4 %TD with 9.6 % shrinkage.

Thus, though different starting materials have been employed in RBM protocols, the sintering temperatures are too high for Nextel 720 fiber-reinforced composites receiving attention in the present work.

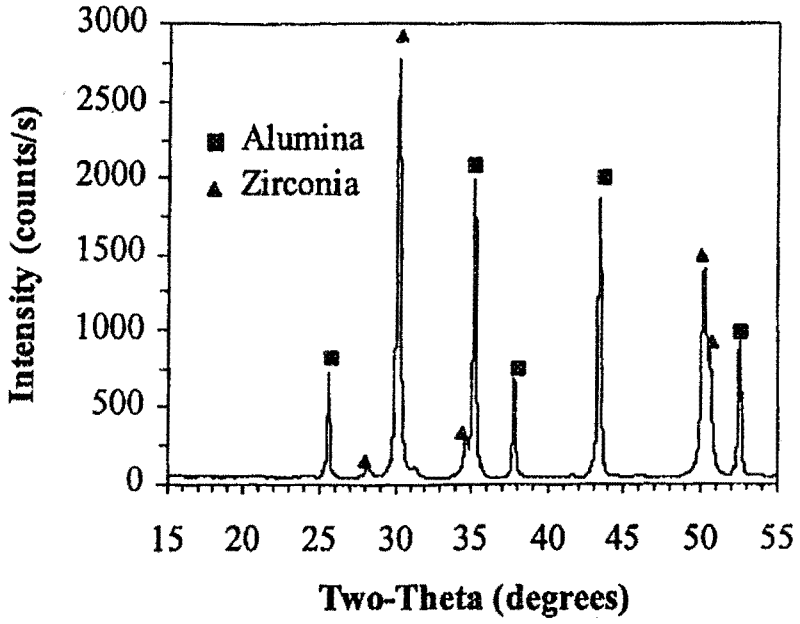

Fig. 2-13. XRD diagram of the AM35Z15 specimen after heat-treatment at 1100 °C for 20 hrs (She et al. 2001).

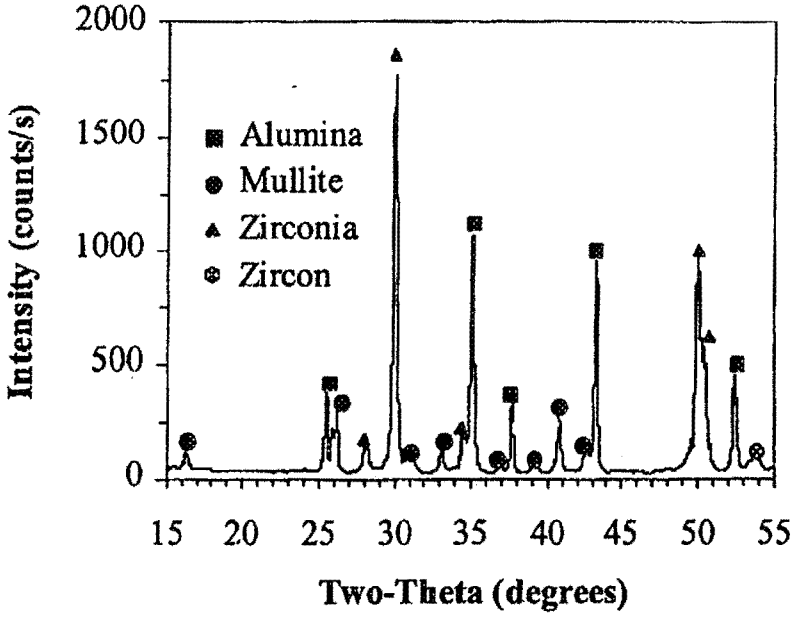

Fig. 2-14. XRD diagram of the AM35Z15 specimen after heat-treatment at 1580 °C for 2 hrs (She et al. 2001).

Recently, Mechnich et al. (1998), (1999) used mixed powders of Al_2O_3, Si, mullite seeds and Y_2O_3 (or CeO_2) at 1350 °C for 5 hrs to induce RBM. The aim was to use the lower-temperature eutectic transient liquid phase to develop mullite on sintering. They proposed that Si oxidation is promoted by CeO_2 and Y_2O_3 (Fig. 2-15). All the RBM specimens initially displayed the Si-oxidation-related length increase (starting at 700 °C) that maximises at 1100 °C (Fig. 2-16). The length increase achievable corresponds to silicon content. All samples exhibited sintering shrinkage above 1100 °C with 2.5-5 % final shrinkage. CeO_2-, and Y_2O_3-doped RBM resulted in a higher mullite content than the undoped mixes (X-ray diffraction patterns, Fig. 2-17). Mullite seeds were included to promote mullite formation. Y_2O_3 (or CeO_2) facilitates Si oxidation and mullite formation via the Al_2O_3/SiO_2/rare-earth-oxide eutectic liquid. The sintering temperatures employed were lower than those of previous RBM studies, but still too high for the Nextel 720 as its strength degrades above 1300 °C (Petry and Mah (1999)). However this work suggested an approach for the production of a high-mullite (more than 90 %), high density (more than 90 % theoretical) matrix for Nextel 720-reinforced, mullite-matrix composites.

2-3 The Degradation of Nextel 720 Fibre above 1300 °C

Oxide-fiber, oxide-matrix composites are being developed for high temperature oxidizing environments. Nextel 720 is a mullite fiber developed by 3M, capable of sustaining below 1300 °C and is relatively cheap.

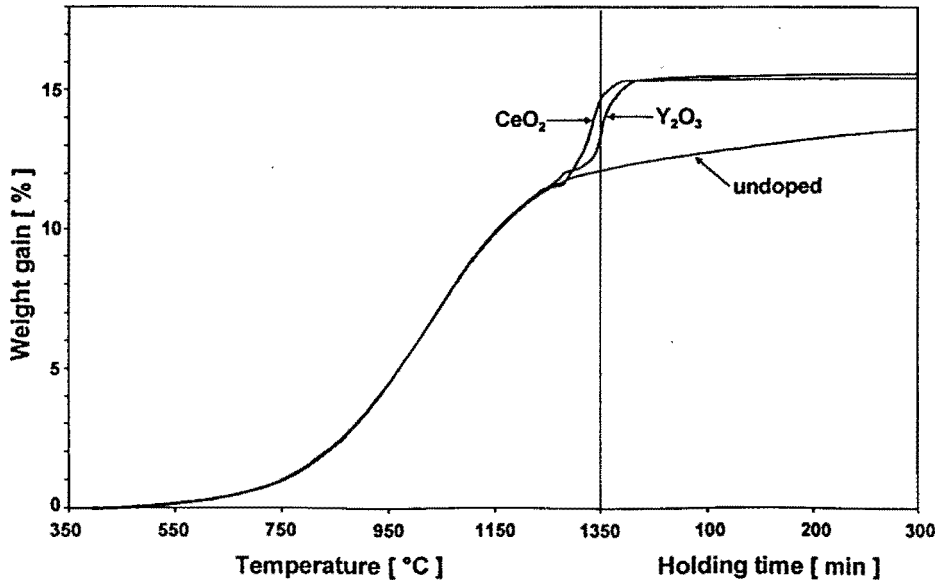

Fig. 2-15. Temperature-dependent weight-change curves of undoped and doped RBM samples (Mechnich et al. 1998).

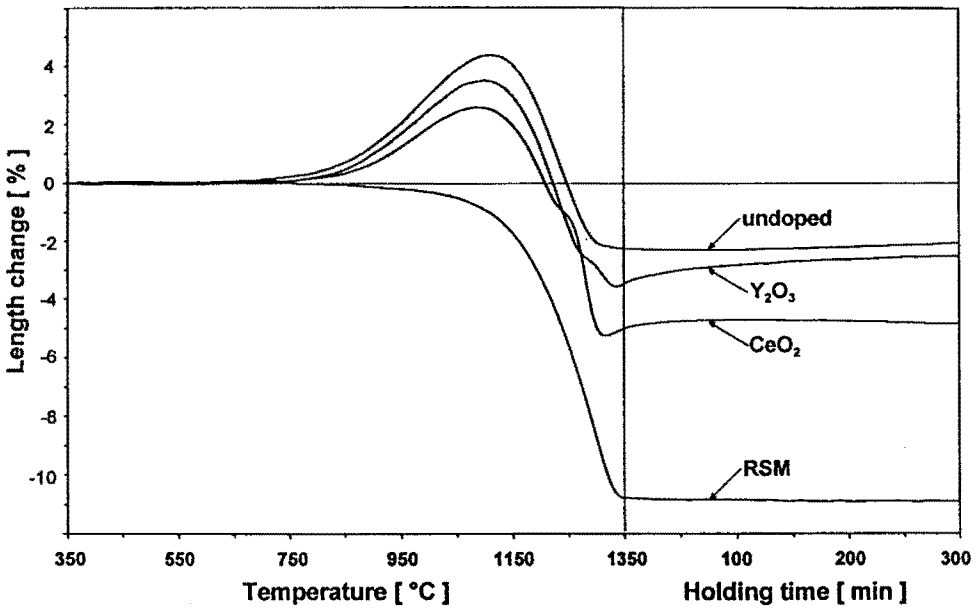

Fig. 2-16. Temperature-dependent length-change curves of undoped and doped RBM samples (Mechnich et al. 1998).

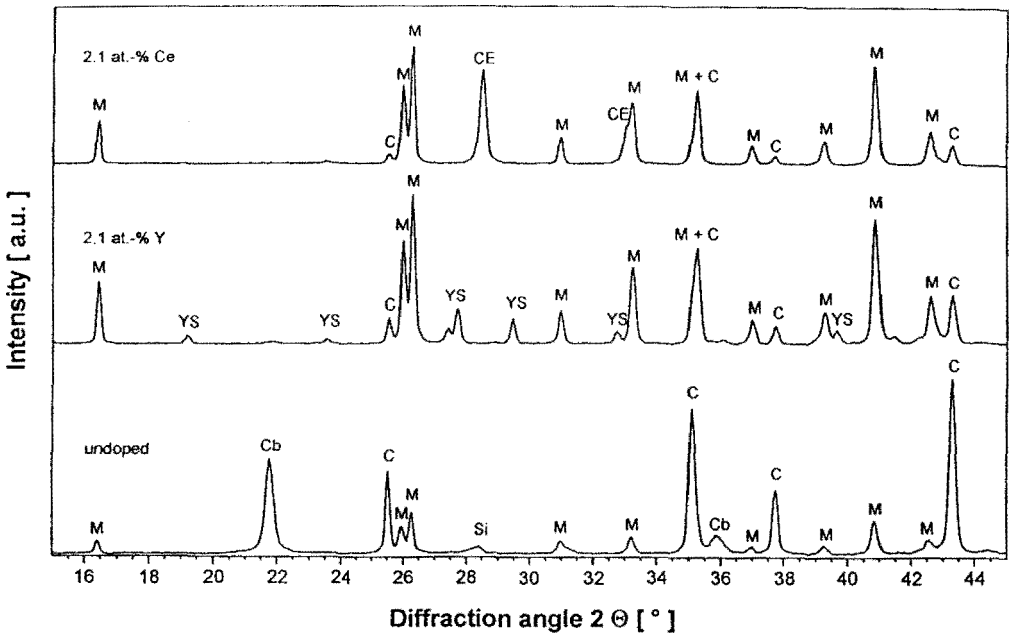

Fig. 2-17. XRD patterns of undoped and doped RBM samples (Mechnich et al. 1998).

Efforts have been made to use Nextel 720 in fiber-reinforced, mullite-matrix composites (Westby et al. (1999) and Kooner et al. (2000)), but so far inferior properties have resulted. Nextel 720 is 85 wt% Al_2O_3 and 15 wt%SiO_2, ie; mullite and Al_2O_3 and typical properties are listed in Table 2-1.

Wilson et al. (1995), (1997), Göring and Schneider (1997) have investigated the high temperature mechanical properties of Nextel 720. Though this fibre exhibits excellent properties at high temperature, these degrade appreciably above 1300 °C. Recently, Petry and Mah (1999) demonstrated the degradation of Nextel at temperature (Fig 2-18). If the triangle motifs that designate the strengths-in-air are connected, the degradation rate is tracked by the slope of the line. The slope is relatively low up to 1300 °C, but increases markedly thereafter. Processing temperatures for Nextel-containing composites, must therefore, be less than 1300 °C.

2-4 The Si Powder Oxidation Process

The thermal kinetics of silicon oxidation are based on a simple model of oxidation occurring at the two boundaries of the oxide layer and the diffusion involved.

Deal and Grove (1965) considered silicon covered by an oxide layer of thickness x_o (Fig. 2-19) and assumed oxidation proceeds by the inward movement of oxidant rather than the outward movement of silicon (Atalla (1960), Ligenza and Spitzer (1960), Jorgensen (1962) and Pliskin and Gnall (1964)). The oxidant requires three transportation

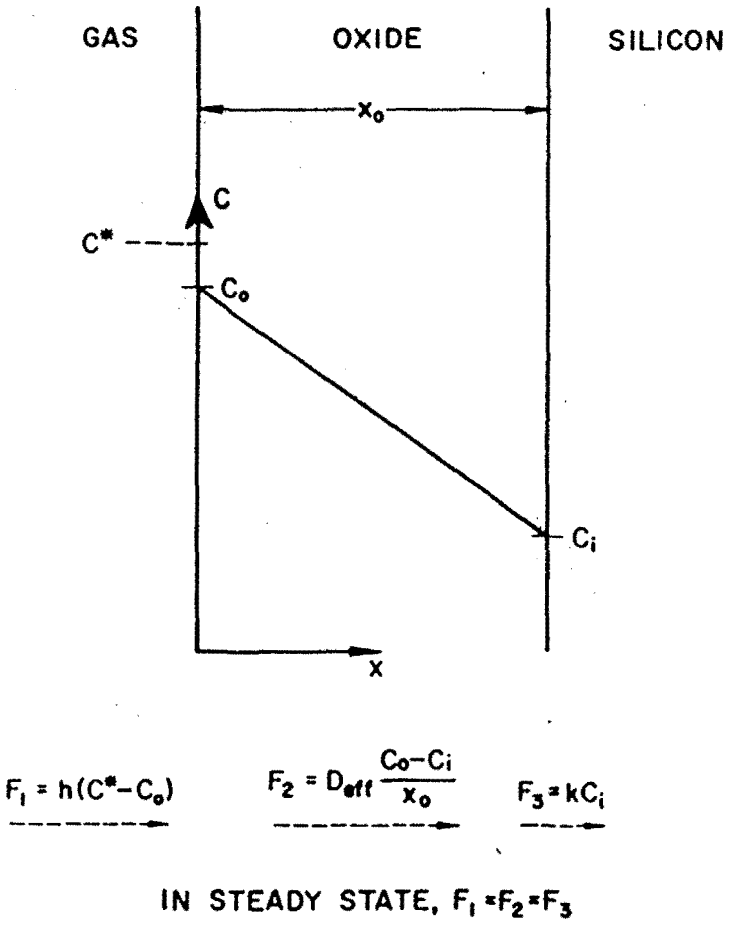

Fig. 2-19. Model for the oxidation of silicon (Deal and Grove 1965).

Table 2-1 The properties of Nextel 720 (Nextel, 3M 1997)

Properties	Nextel 720
Use temperature	1255 °C
Filament diameter	10 ~ 12 μm
Crystal Size	>500 nm
Crystal type	Alpha Al_2O_3 + mullite
Density	3.4 g/cm^3
Tensile strength	2100 Mpa
Chemical composition	85 % Al_2O_3, 15 % SiO_2
Thermal expansion	6.0 ppm/°C

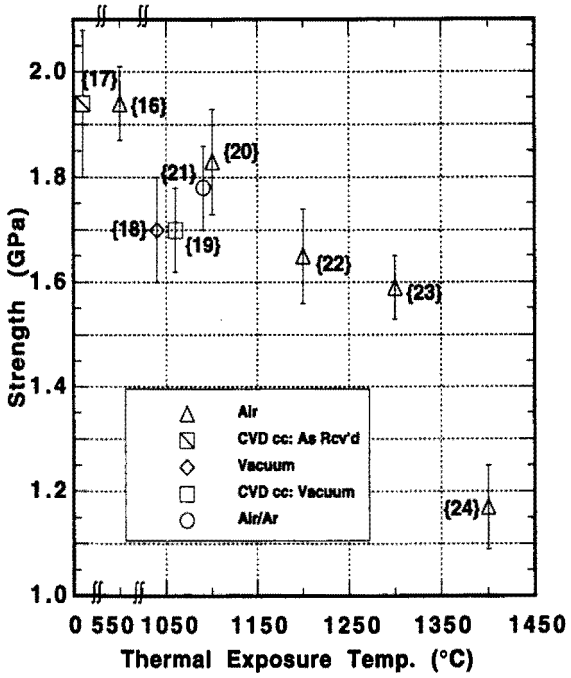

Fig.2-18. Strength vs. thermal exposure temperature for Nextel 720 (Petry and Mah 1999).

stages;

(1) From the gas to the outer Si surface.

(2) Across the SiO_2 film to the Si.

(3) Reaction at the Si surface to form new SiO_2.

It is assumed that the oxidant flux in the three steps is identical. The flux of the oxidant from the outer surface is;

$$F_1 = h(C^* - C_o) \tag{2-1}$$

where h is gas phase transport coefficient, C_o the oxidant concentration at the outer surface, and C^* the equilibrium concentration of the oxidant in the oxide.

Fick's law gives the flux of the oxidant across the oxide layer as;

$$F_2 = -D(dc/dx), \tag{2-2}$$

where D is the effective diffusion coefficient and dc/dx the concentration gradient. Since the concentration of oxidant in the oxide layer is linear, Flux 2 is given by;

$$F_2 = -D(C_o - C_i)/x_o, \tag{2-3}$$

where C_i is the oxidant concentration near the oxide-Si interface and this is the same as the oxidant concentration in the Si. Finally, the flux of oxygen in the Si oxidation is

$$F_3 = kC_i, \tag{2-4}$$

where k is the surface reaction rate constant.

$F_1 = F_2$, and $F_2 = F_3$ due to steady state conditions. Determining C_i and C_o in terms

of C^* then;

$$C_i = \frac{C^*}{1+\frac{k}{h}+\frac{kx_o}{D}} \quad \text{and}$$

$$C_o = \frac{(1+\frac{kx_o}{D})C^*}{1+\frac{k}{h}+\frac{kx_o}{D}} . \tag{2-5}$$

The above equations show the effect of diffusivity, D, on the O_2 concentration in the oxide layer. When D is very small, $C_i \rightarrow 0$, $C_o \rightarrow C^*$, then $F_2 \rightarrow 0$. This condition is commonly referred to as "diffusion-controlled." When D is large, $C_i = C_o = C^*/(1+k/h)$. The flux is given by;

$$F = F_1 = F_2 = F_3 = \frac{kC^*}{1+\frac{k}{h}+\frac{kx_o}{D}} \tag{2-6}$$

on elimination of C_i and C_o.

When the number of O_2 molecules per a unit volume involved in the growth rate of the oxide layer is N, the growth rate of the oxide layer can be calculated by

$$F = N\frac{dx_o}{dt} = \frac{kC^*}{1+\frac{k}{h}+\frac{kx_o}{D}} . \tag{2-7}$$

For the general initial conditions, an initial oxide layer thickness, x_i, might be present on the Si prior to initiation of oxidation. Thus initial conditions require $x_o = x_i$ at $t = 0$.

Bardeen et al. (1946) found an initial oxide layer may form by mechanisms involving

fields and space charges within an oxide layer.

Solution of the differential equation 2-7 is;

$$x_o^2 + Ax_o = Bx_o + x_i^2 + Ax_i \tag{2-8}$$

which can be rewritten in the form;

$$x_o^2 + Ax_o = B(t+\tau) \tag{2-9}$$

where $A = 2D(1/k + 1/h)$ (2-9a)

$$B = 2DC^*/N \tag{2-9b}$$

and $\tau = (x_i^2 + Ax_i)/B$. (2-9c)

τ is the time required for growth of the x_i layer. Evans (1924), (1960) proposed this mixed parabolic relationship. If equation 2-9 were solved further, it yields;

$$\frac{x_o}{A/2} = [1 + \frac{t+\tau}{A^2/4B}]^{1/2} - 1. \tag{2-10}$$

At relatively long times, i.e.; $t >> A^2/4B$ and $t >> \tau$, Equation 2-10 becomes $x_o^2 = Bt$, where B is the parabolic rate constant. For relatively small oxidation times, i.e.; $t << A^2/4B$, equation 2-10 becomes $x_o = B/A\ (t+\tau)$, where B/A is a linear rate constant. The oxide layer-forming model explains the experimental results for thermal oxide layer formation on Si. Figs. 2-20 and 2-21 show the oxidation process for Si in wet and dry oxygen. To check how equation 2-9 fits the data, Figs. 2-20 and 2-21 are replotted in

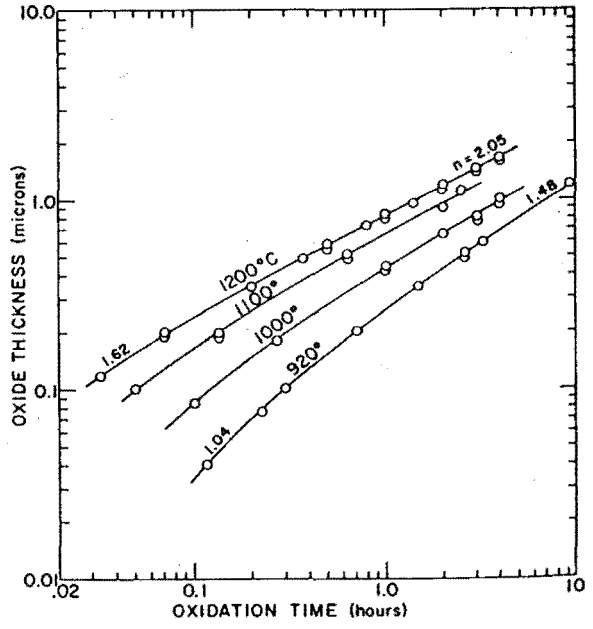

Fig. 2-20. Oxidation of silicon in wet oxygen (95 °C H_2O) (Deal and Grove 1965).

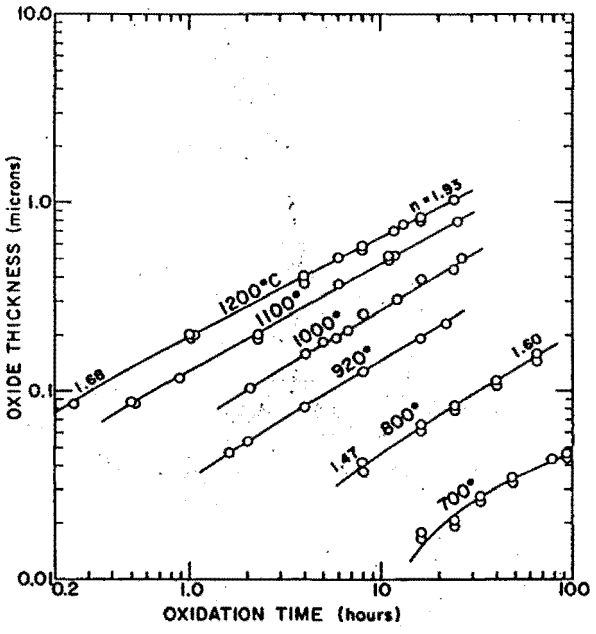

Fig. 2-21. Oxidation of silicon in dry oxygen (760 Torr) (Deal and Grove 1965).

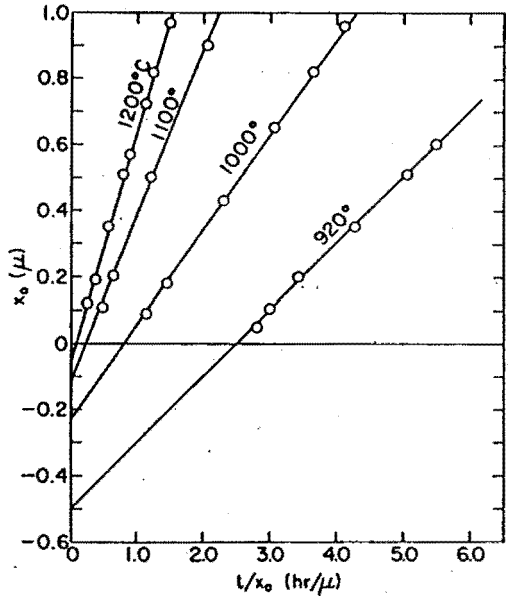

Fig. 2-22. Evaluation of the rate constants for Si oxidation in wet oxygen (95 °C H_2O) (Deal and Grove 1965).

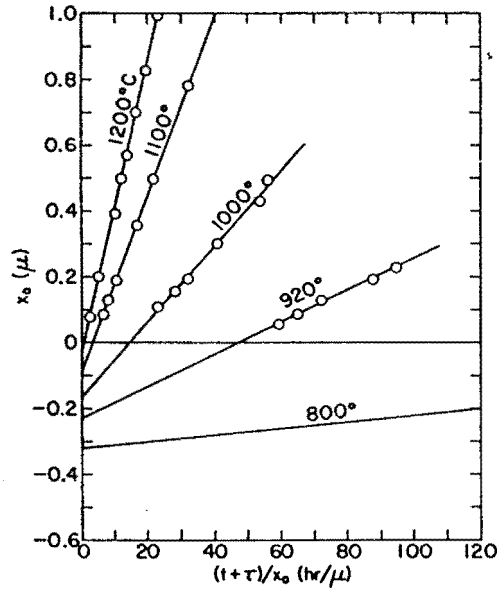

Fig. 2-23. Evaluation of the rate constants for Si oxidation in dry oxygen (760 Torr) (Deal and Grove 1965).

Figs. 2-22 and 2-23.

Thus experimental results fit the general oxidation equation. Oxidation in wet O_2 is faster than in dry O_2. The pre-existence of an oxide layer does not influence subsequent oxidation. This result makes prediction of the oxide layer thickness easy. In the present work, a pre-existent layer of SiO_2 on the Si is detected via the TGA results.

2-5 Mixed Rare Earth Oxide Eutectic

Mixed-rare-earth-oxide contains several rare earth oxides. The MREO product is termed Lanthanide oxide by Molycorp Inc. and the main oxides are CeO_2 and La_2O_3. The composition of the mixed-rare-earth-oxide used in the present study is listed in Table 2-2.

The objective of this study is to lower the processing temperatures for the synthesis of mullite. Commercially-available MREO yields a low eutectic temperature with Al_2O_3 and SiO_2. It is also cheap as it is mined directly as a natural mineral.

2-6 Low-Temperature Eutectics in Al_2O_3/SiO_2/Rare-Earth-Oxide Mixture Compositions

The Al_2O_3-SiO_2-Y_2O_3 phase equilibrium diagram (Fig. 2-24) (Bondar and Galakhov 1964) provides the approximate eutectic composition for $Al_2O_3/SiO_2/Pr_6O_{11}$, $Al_2O_3/SiO_2/Eu_2O_3$ and Al_2O_3/SiO_2/mixed-rare-earth.

Table 2-2 The distribution oxides in mixed rare earth oxide

Oxides	Content (wt%)
CeO_2	49
La_2O_3	33
Nd_2O_3	13
Pr_6O_{11}	4
Sm_2O_3	0.5
Gd_2O_3	0.2
Eu_2O_3	0.1
Others	0.2

The diagram for Y_2O_3-Al_2O_3–SiO_2 contains eight invariant points, ie, two eutectics and six peritectics. Table 2-3 lists the compositions and temperatures of these invariant points. The eutectics are at 1840 °C and 1345 °C. The lower one was used by Mechnich et al. (1998) for reaction-bonding and sintering. This composition is 22 wt% Al_2O_3, 46 wt% SiO_2 and 32 wt% rare earth oxide.

2-7 Liquid Phase Sintering

2-7-1 The Process of Liquid Phase Sintering

Sintering is the process whereby packed powders densify at high temperatures. The driving force is the reduction of system surface area, i.e.; free energy. This occurs via atomic motion at sintering temperatures. Sintering can be accomplished with or without liquid phase. As the necessary mass transport occurs by diffusion (Kuczynski (1949), Hoge and Pask (1973) and Coble (1961)), liquid phase accelerates sintering. Kingery (1959) studied densification during sintering in the presence of a liquid phase. Usually the liquid wets the solid, i.e.; it has solubility for the solid so the wetting liquid surrounds the solid particles and isolates porosity and reduces the interfacial energy.

Fig. 2-25 shows a schematic sequence of the steps (German (1985), (1996)) involved in liquid phase sintering. Three steps are suggested in the changing microstructure (Lenel (1948), Cannon and Lenel (1953), Kingery (1959)). First is

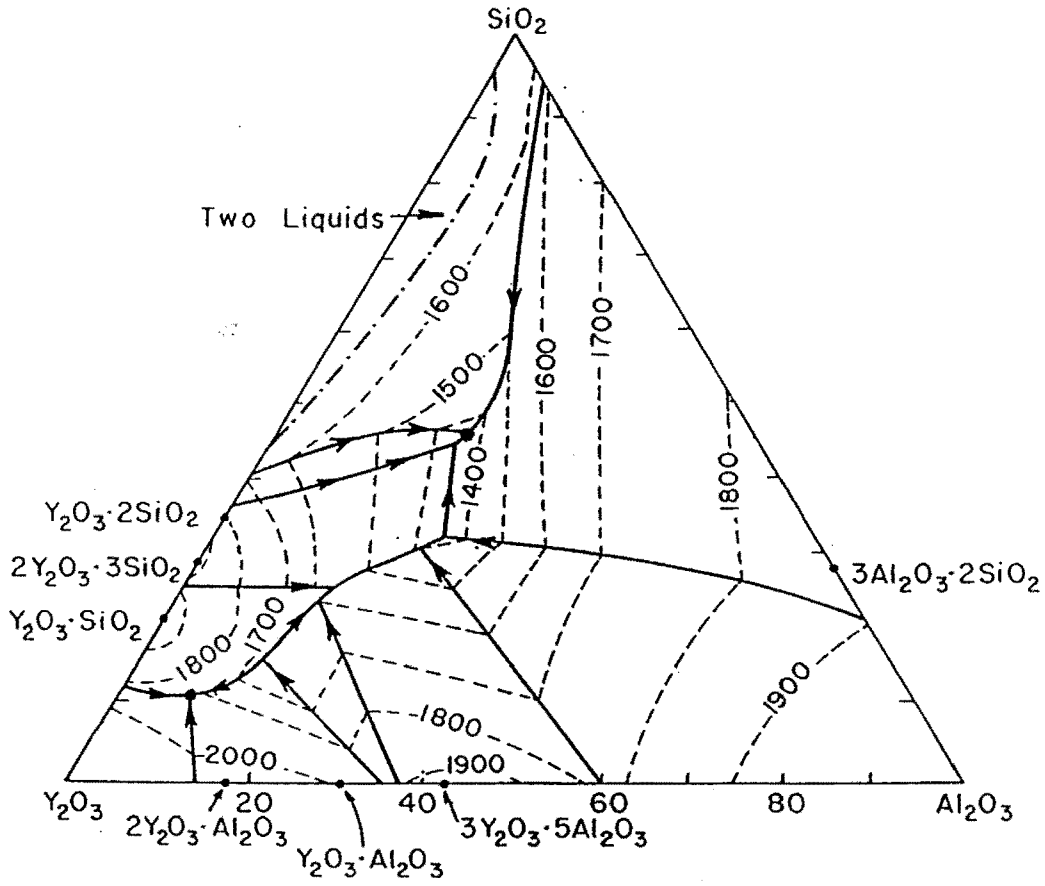

Fig. 2-24. Phase diagram of the Al_2O_3-SiO_2-Y_2O_3 system (Bondar and Galakhov 1964).

Table 2-3 Invariant points of the system Y_2O_3-Al_2O_3-SiO_2 (Bondar and Galakhov 1964)

Phase	Process	Temp (°C)	Composition % by weight		
			Y_2O_3	Al_2O_3	SiO_2
$Y_2O_3 + 2Y_2O_3{\cdot}Al_2O_3 + Y_2O_3{\cdot}SiO_2$ + liquid	Eutectic	1840	80.5	8.5	11.0
$2Y_2O_3{\cdot}Al_2O_3 + Y_2O_3{\cdot}SiO_2 + Y_2O_3{\cdot}Al_2O_3$ + liquid	Peritectic	1680	70.0	14.0	16.0
$Y_2O_3{\cdot}Al_2O_3 + 3Y_2O_3{\cdot}5Al_2O_3 + Y_2O_3{\cdot}SiO_2$ + liquid	Peritectic	1600	60.0	16.6	23.4
$Y_2O_3{\cdot}SiO_2 + 2Y_2O_3{\cdot}3SiO_2 + 3Y_2O_3{\cdot}5Al_2O_3$ + liquid	Peritectic	1565	56.5	18.2	25.3
$3Y_2O_3{\cdot}5Al_2O_3 + 2Y_2O_3{\cdot}3SiO_2 + Al_2O_3$ + liquid	Peritectic	1400	45.0	24.5	30.5
$Al_2O_3 + 3Al_2O_3{\cdot}2SiO_2 + 2Y_2O_3{\cdot}3SiO_2$ + liquid	Peritectic	1385	41.4	25.8	32.8
$3Al_2O_3{\cdot}2SiO_2 + Y_2O_3{\cdot}2SiO_2 + 2Y_2O_3{\cdot}3SiO_2$ + liquid	Peritectic	1360	34.5	21.5	44.0
$3Al_2O_3{\cdot}2SiO_2 + Y_2O_3{\cdot}2SiO_2 + SiO_2$ + liquid	Eutectic	1345	32.0	22.0	46.0

formation of a wetting liquid phase and flow thereof to facilitate rearrangement of the "wet" solid particles, i.e.; the rearrangement process. Second is an increase of density by dissolution and reprecipitation of solid phase- the "solution –precipitation" process. The third process is densification by formation of a solid skeleton. This process is referred to as the "coalescense process". These processes are discussed later in this section.

2-7-1-1 The Driving Force for Liquid Phase Sintering

Surface energy reduction is the major factor determining sintering. The surface energy relationship for the wetting of a solid;

$$\gamma_{SV} > \gamma_{LV} > \gamma_{SS} > 2\gamma_{SL} \qquad (2\text{-}11)$$

where γ is the surface energy and S, V and L are solid, vapour and liquid respectively, i.e. solid/liquid interfaces are preferred. When "wetting" liquid first forms it completely coats the solid particles, eliminating solid-vapor surfaces. Thus pores are isolated in the liquid phase. The result is a decrease of liquid-vapor surface area, i.e., the surface energy reduction that drives densification. Within each pore there is a negative pressure given by

$$P_o = \frac{-2\gamma_{LV}}{r_p} \qquad (2\text{-}12)$$

where r_p is the pore radius, P_o the pressure and γ_{LV} the liquid/vapour surface energy. This "suction" pressure initially rearranges particles to give maximum packing. Then

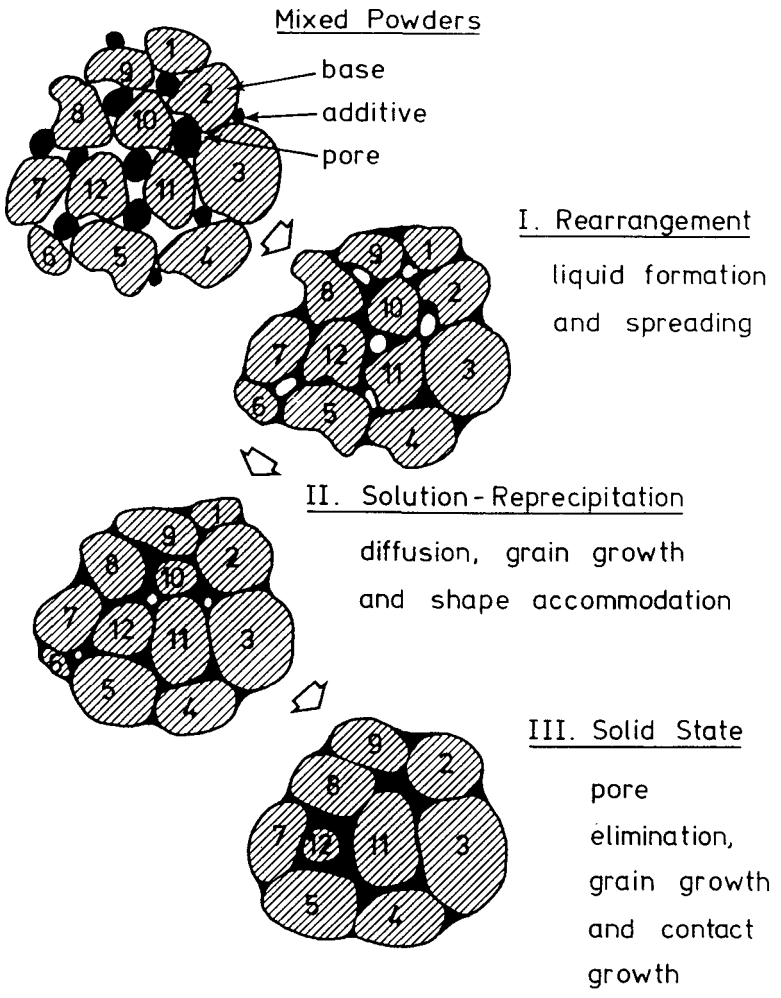

Fig. 2-25. The classic stages of liquid phase sintering (German 1985).

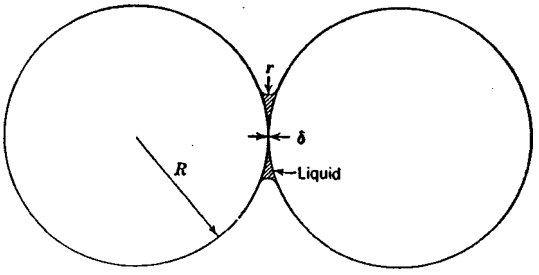

Fig. 2-26.Spherical particles held together by liquid capillary pressure (Kingery 1959).

compressive stresses develop via the thin liquid film between the solid solid-particle contact points which can be visualized as two spheres separated by the liquid (Fig. 2-26). These spheres suffer pressure by capillary action (Kingery (1959)), i.e.;

$$P = \frac{-\gamma_{LV}}{r}. \tag{2-13}$$

Heady and Cahn (1970) developed an expression for the capillary pressure. When two solid spheres are held together by the interparticle force due to capillary pressure of a liquid contact, the interparticle force has two contributions, one due to the surface tension itself and the other due to the pressure difference caused by surface curvature.

Using the two sphere model illustrated in Fig. 2-27, the pressure difference between the liquid meniscus and the vapor is given by the Laplace equation (Gillespie and Settineri (1967)). The excess pressure, ΔP, across a curved liquid surface depends on the two radii of curvature (R_1 and R_2) and the surface energy, is given by;

$$\Delta P = \gamma_{LV}\left[\frac{1}{R_1} + \frac{1}{R_2}\right]. \tag{2-14}$$

The radii of curvature of the liquid depends on the liquid contact angle, the particle separation and the particle size. The force between the two spheres is given by summing the pressure and the surface energy contribution (Derjaguin (1968), Princen (1968), Heady and Cahn (1970) and Emi et al. (1979)).

Three forces are considered by cutting the system through any plane, z=k, and making a force balance in the z direction across the cut, i.e.;

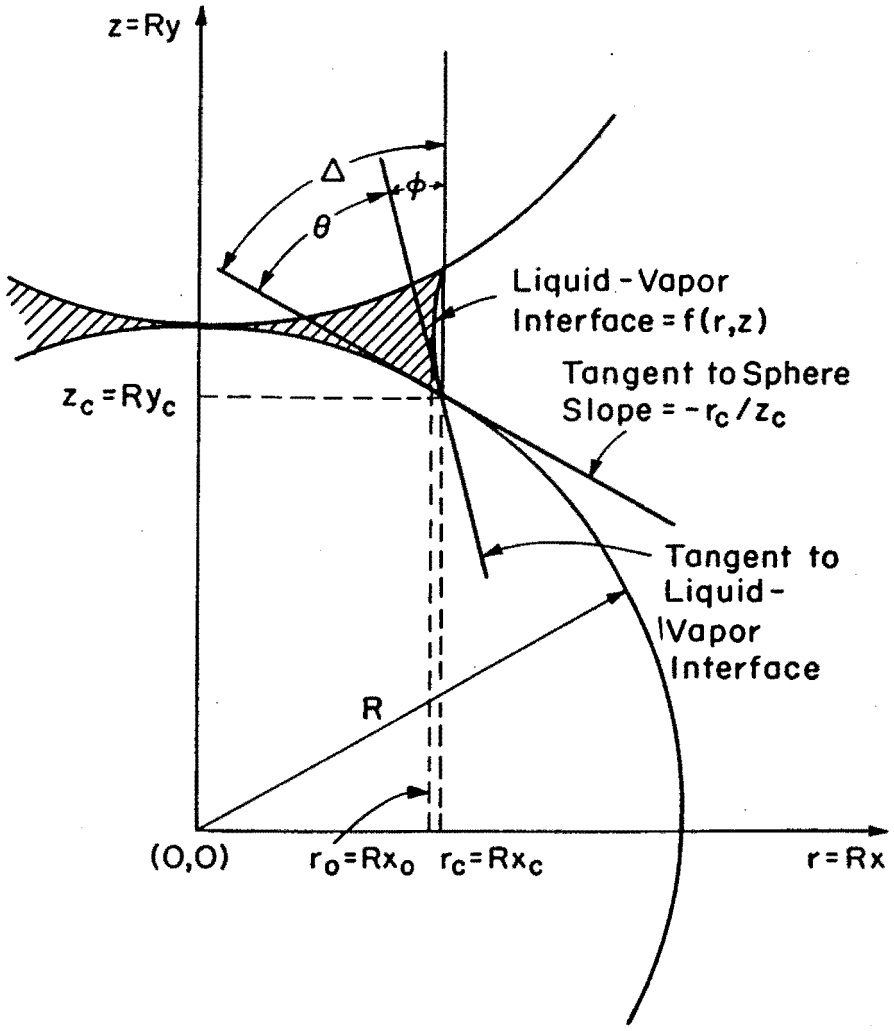

Fig. 2-27 Two spheres with pendular liquid ring and definition of variables (Heady and Cahn 1970).

(1) $\gamma_{LV}\, 2\pi r\cos\phi$ (due to surface tension)

(2) $\pi(r^2 - r_s^2)\Delta P$ (due to the pressure difference ΔP = (P_{liquid} - P_{vapor}) resulting from the liquid-vapor interface

(3) $\int_A \sigma dA$ (due to the stress in the solid).

r is the radius of curvature on the liquid-vapor interface in Fig. 2-27. r_s is the radius of circular section of the sphere exposed when cut by plane z = k. σ is the component of the stress on the sphere perpendicular to the plane of area, A. If gravity is ignored, the pressure in the liquid is equal and $\int_A \sigma dA$ must be $\pi r_s^2 \Delta P - F$ where F is the force across the solid-solid contact. Hence

$$F = 2\pi r\gamma_{LV}\cos\phi + \pi r^2 \Delta P \qquad (2\text{-}14)$$

The capillary pressure induces substantial compressive force at the contact area and results in an increase of chemical potential (or activity) of the solid phases at the contact, i.e.;

$$\mu - \mu_o = RT\ln(\frac{a}{a_o}) = \Delta P V_o \qquad (2\text{-}15)$$

$$\ln(\frac{a}{a_o}) = \frac{K2\gamma_{LV}V_o}{r_p RT} \qquad (2\text{-}16)$$

Where K is a constant relating the maximum contact area pressure to the overall hydrostatic pressure. The activity at the contact points is increased dramatically and this

provides the driving force for particle material transfer into the liquid in such a way that the particle centers move together and density increases.

The sintering rate is determined by the diffusion coefficient of the dissolving species in the liquid. Diffusivities of solid and liquid are very different. For instance, Frischat (1975) showed the Si diffusion data in liquid and solid slag glass is 1.1×10^{-7} ~ 4.7×10^{-8} cm^2/s vs. 1.0×10^{-13} ~ 6.7×10^{-15} cm^2/s. Thus diffusivity in liquid is much larger than in solid.

$$D_{solid} << D_{liquid}$$

Therefore, it is important that liquid phase be present if low temperature reactions are required.

2-7-1-2 Solid-Particle Rearrangement in the Presence of a Liquid-Phase

Liquids may form in a system when solid particles react. By definition such liquids "wet," so penetrate the solid particles as a film. Capillary forces develop and squeeze the solids together ($P=-\gamma L_V/r$). Residual stresses remain in powder compacts following green shaping and the first liquid relieves these stresses, i.e. the particles rearrange. The capillary pressure also rearranges the particles to maximum packing and minimum porosity. The three steps involved are melting, spreading and penetration and the shrinkage dependence with time is:

$$\frac{\Delta L}{L_o} \propto r^{-1} t^{1+y} \qquad (2\text{-}17)$$

where L_o is the initial size, ΔL the change of size on sintering, r is the solid particle radius, and (1+y) is slightly larger than unity. This equation assumes the strain ($\Delta L/L_o$) is directly proportional to time. The surface energy in the system is assumed to remain constant. Actually, the porosity and capillary pore size continually decrease during the solid particle rearrangement process.

2-7-1-3 The Solution-Precipitation Process during Liquid-Phase Sintering

Densification by rearrangement is slow, so solubility and diffusivity effects dominate densification in the presence of a liquid phase. The liquid dissolves the solid particles at the pressure points and this pressure-driven dissolution induces the liquid to dissolve more solid than under stress-free conditions, i.e. the liquid at the points of contact supersaturates. Thus a concentration gradient develops and the excess diffuses from the solid contact points, to precipitate in stress-free region. This process is termed solution-precipitation and results in the sharp edges of particles being removed and the particles move closer (the compact densifies). The stress-free regions are pores so precipitates fill them in. Smaller particles dissolve faster so microstructural coarsening occurs. Solution-precipitation involves two steps: dissolution and diffusion in the liquid. When limited by the rate of mass transfer from the source to the sink, the process is "diffusion" limited. Alternatively, if transport is controlled by dissolution the reaction is said to be "dissolution limited."

Kingery (1959) derived functional relationships between the densification rate for sintering in the presence of a liquid phase and parameters such as sintering time and particle size for diffusion and dissolution-controlled shrinkage, as;

$$\frac{\Delta L}{L_o} \propto r^{-4/3} t^{1/3} \quad \text{(diffusion-controlled shrinkage)} \tag{2-18}$$

where L_o is the original length, ΔL the change of length, r the particle size and t the time. i.e.; shrinkage is proportional to the one-third power of time and inversely proportional to the four-thirds power of the initial particle size.

For dissolution-controlled shrinkage, he found;

$$\frac{\Delta L}{L_o} \propto r^{-1} t^{1/2} \tag{2-19}$$

i.e. the shrinkage is proportional to the square root of time and inversely proportional to the initial particle size. The diffusion-controlled process is thus more sensitive to particle size than the dissolution-controlled process.

2-7-2 Sintering in the presence of a Transient Liquid Phase

Liquid phases enhance sintering because they increase system ionic mobility. However, for high temperature service (eg. turbine components), liquid formation can be detrimental. Thus liquid phases that persist in sintered microstructures, ruin high temperature integrity. To avoid the latter, yet have liquid phase present for sintering, powders of different composition are mixed such that one (or more) form a liquid which

then reacts with neighboring components to give a solid of the required composition. If the other components of the system are termed the "base," and the liquid-forming phase the "additive," there are two options:

2-7-2-1 The Base Dissolves the Additive

Phase diagrams predict the composition of precursors for this case. Fig 2-28 illustrates two systems that produce a transient liquid. In the first, the liquid forms by eutectic reaction, i.e.; a powder of this composition is included in the powder mix. This liquid disappears as it reacts with the other solid neighbors to produce solid of desired final composition. In the second case, the additive melts and, being soluble in the base, disappears with time.

The benefits of transient liquid phase are easy compaction and sintering, however, swelling occurs when the liquid forms as it is less dense than when solid.

A common application of transient liquid phase sintering is dental amalgam, Ag powder and liquid Hg. Ag powder is mixed with liquid Hg and the slurry compressed into the dental cavity. The mixture sets as Ag dissolves the Hg. Jangg (1964) reviewed several variants of this amalgamation reaction. Another example used in the modern world is self-lubricating bronze bearings. Mixtures of Cu and Sn powders are pressed, the Sn melts and dissolves in the Cu leaving pores into which oil permeates (Kohno and Koczak (1982), Berry (1972) and Peissker (1974)).

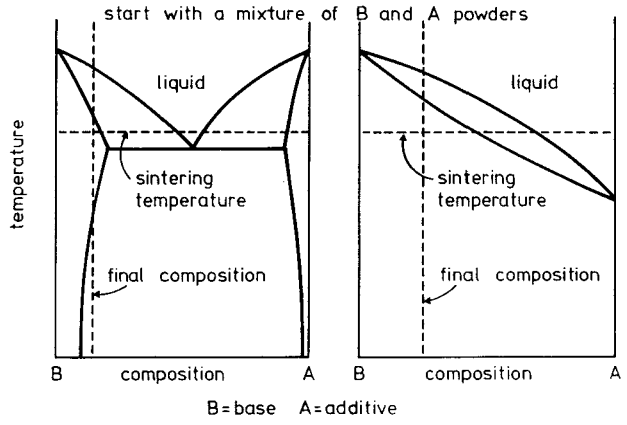

Fig. 2-28. Two binary phase diagrams which could form the basis for transient liquid (German 1985).

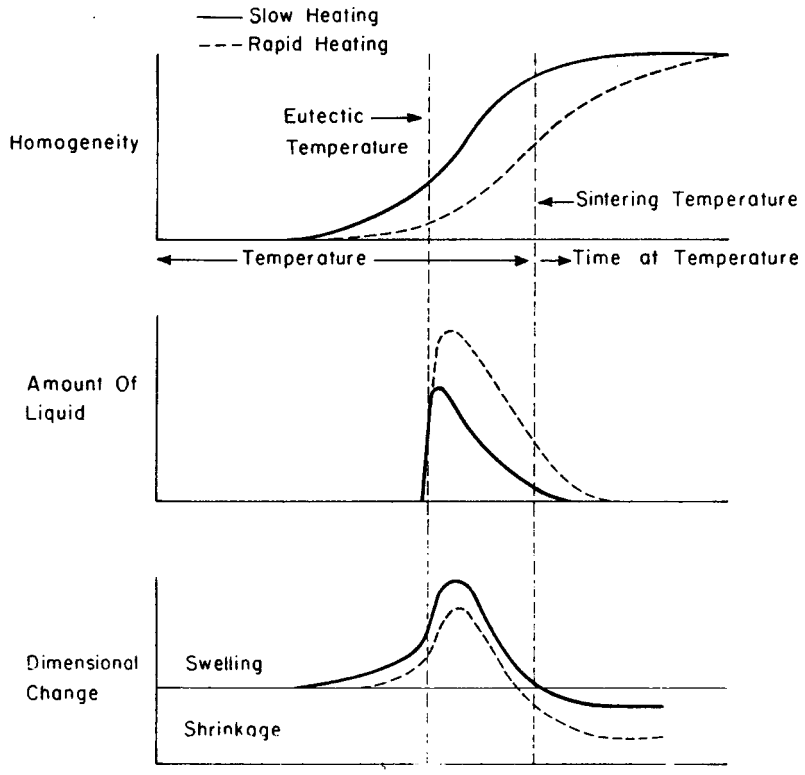

Fig. 2-29. An example of the heating rate effect on transient liquid phase sintering (German 1985).

The requirement of this process is mutual solubility between the components and existence of the final composition within a single, solid-phase field. Moreover, the liquid must wet the solid to give a high diffusion path of the ions therein. The observed steps were suggested by Kehl and Fischweister (1980), Banerjee et al (1980) and Lee and German (1985): i.e.; (1) swelling; (2) melt formation; (3) spreading of the melt and generation of pores; 4) melt penetration along solid-solid contact boundaries; 5) rearrangement of the solid grains; 6) solution-reprecipitation induced densification; 7) diffusional homogenization; (8) loss of melt by reaction, and finally; (9) the formation of a rigid structure.

Heating rate is important in transient-liquid-phase-sintering (Fig 2-29). Swelling occurs at low heating rates but, may be helpful for the zero-shrinkage required by reaction-bonding. The volume fraction liquid, V_L, is proportional to the additive concentration, C_A, and the heating rate, x, i.e.;

$$1-(\frac{V_L}{fC_A})^{1/3} = \kappa(\frac{T_L}{x})^{1/2} \qquad (2\text{-}20)$$

where f and κ are proportionality constants and T_L the liquid formation temperature. Solid-state diffusion can give an intermediate compound as the surrounding envelope develops (Fig. 2-30). This envelope can inhibit subsequent diffusion (Baek (1985)). The thickness, W, of the intermediate compound that forms initially, increases with time, (t), as follows (Albano-Muller et al. (1973));

$$W \propto (Dt)^{1/2} \qquad (2\text{-}21)$$

where D is the controlling diffusion rate within the compound layer.

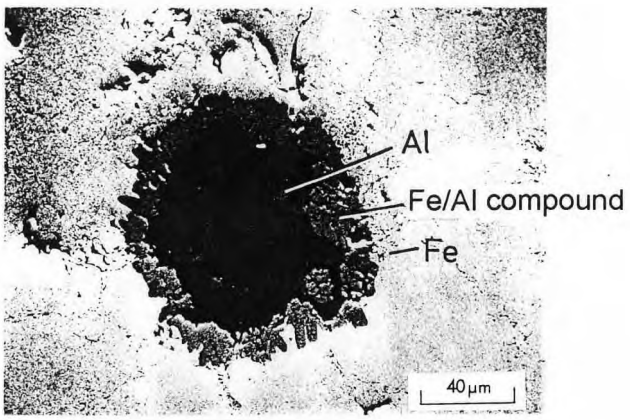

Fig. 2-30. SEM photography of the intermetallic envelope formed around an Al particle particle in an Fe-Al powder compact heated to 635 °C (Lee and German 1985).

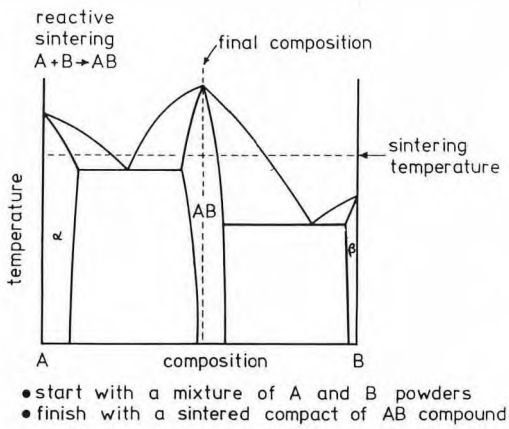

Fig. 2-31. A binary phase diagram for reactive liquid phase sintering of the AB compound from mixed A and B powder (German 1985).

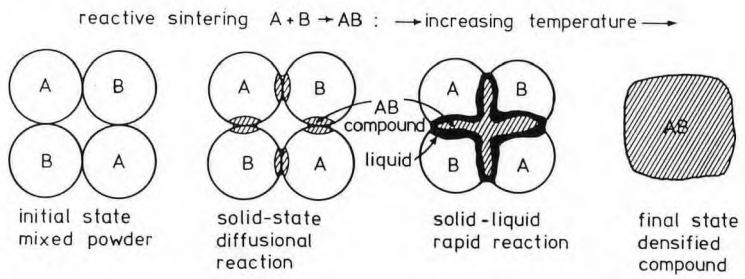

Fig. 2-32. Typical sequence of events in reactive sintering (German 1985).

2-7-2-2 The Base Reacts with the Liquid Additive

This is called "reactive-sintering". It can involve more than one liquid (Coble (1982)). Fig 2-31 illustrates the phase diagram for reactive sintering. A and B form compound AB and a liquid forms. The stages of sintering are shown in Fig 2-32.

The liquid front progresses with time to give solid AB. The product is now a compound rather than a solid solution. The time of liquid residence in the system is important because it confers rapid diffusion, i.e.; rapid sintering. The liquid reacts away with time, however, and the relative densities of the liquid and solid can result in residual porosity. Most reactions involved are exothermic and can cause microstructural damage. Swelling due to short-time-liquid-duration, is a problem.

Mechnich et al (1998), (1999) discussed the role of transient liquid phase in RBM processing. The liquid composition involved is not mentioned but, during reactions, a liquid phase is assumed present. The components, Al_2O_3, Si, CeO_2/Y_2O_3 and mullite seeds were mixed and, during heat treatment, the Si oxidizes to SiO_2 which reacts with the Al_2O_3 and CeO_2 to form liquid phase of eutectic composition. This liquid accelerates mullite formation and pellet densification. The Al_2O_3 and SiO_2 in the eutectic phase precipitates mullite and the CeO_2 / Y_2O_3 aluminosilicate precipitates on the mullite grain boundaries. The liquid forms after Si oxidation so its duration in the system is relatively short and affects mullite formation and densification. However, if liquid forms prior to Si oxidation, it would reside longer and would influence the Si oxidation rate.

Consequently, earlier liquid formation could induce more rapid reactions and sintering. Thus processing temperatures could be lowered.

In the present study, the eutectic powder was formulated from Al_2O_3, SiO_2 and mixed-rare-earth-oxide. The latter was employed, as the eutectic with Al_2O_3 and SiO_2 is lower than for the pure rare earth oxides (Y_2O_3, CeO_2, Pr_6O_{11} and Eu_2O_3). Al_2O_3, Si, MREO eutectic and mullite seeds are mixed together so transient liquid appears at lower temperatures. Its role in the RBM synthesis process is discussed in Chapter 4.

CHAPTER 3

Experimental

3-1 Materials Preparation

3-1-1 The Eutectic

Mixed rare earth oxide (Lanthanide oxide) and two pure rare earth oxides (Pr_6O_{11} and Eu_2O_3) are used to make eutectic compositions with Al_2O_3 and SiO_2. The pure rare earth oxides were used to allow comparison with the mixed-rare-earth-oxide case (MREO). The approximate eutectic composition was estimated from the Al_2O_3-SiO_2-Y_2O_3 phase diagram (Fig. 2-21). The lowest temperature eutectic composition therein is 32 wt% rare earth oxide, 22 wt% Al_2O_3 and 46 wt% SiO_2. Differential thermal analysis (DTA) (5 °C/min) was conducted to determine the precise eutectic temperature for MREO/Al_2O_3/SiO_2. A large sample thereof was then "melted" in a platinum crucible, quenched, ground fine and used as the source of the MREO eutectic for the RBM mixtures.

3-1-2 Premixing of the Al_2O_3 and Si Powders

Mechnich et al. (1998) showed the degree of oxidation is a function of the mean particle size of the silicon powder. The oxidation rate is highest for fine Si powders. Scheppokat et al. (1999) also concluded that mullitization during the synthesis of their reaction-bonded mullite (RBM) depends on the SiC particle size. Smaller particles gave mullitization at lower temperatures.

In the present study, the Si powder is coarser than the Al_2O_3 (Specific surface area of Al_2O_3 and Si are 14.5 m^2/g and 2.0 m^2/g respectively). Thus Al_2O_3 and Si were pre-vibro-milled together in alcohol for 10 days. The surface area of the vibromilled mixture was 15.7 m^2/g and this more reactive powder was employed. Mullite seeds were calcined at 1350 °C for 2 h before mixing into the starting materials. All chemicals used are listed in Table 3-1.

3-2 The Synthesis of Reaction-Bonded Mullite

The starting materials (Al_2O_3, Si, MREO eutectic and calcined mullite seeds) were weighed to give the requisite compositions. Specimens contained differing levels of MREO eutectic and mullite seeds, i.e.; 5 to 10 wt%, though starting materials were formulated to give stoichiometric mullite ($3Al_2O_3{\cdot}2SiO_2$) on sintering.

Table 3-1 Chemicals used in the project

Name	Manufacture	Purity	Remarks
Al_2O_3	Taimei Kagaku Kougyou Co. Ltd.	99.99 %	TM-DAR
Si	Alfar Aesar	99.9985 %	·
SiO_2	PCR	99.9 %	·
Mullite seeds	Degussa, Inc.	·	Calcined at 1350 °C for 2 hrs
Mixed REO	Molycorp, Inc.	·	Lanthanide oxide
Pr_6O_{11}	Cerac	99.9 %	·
Eu_2O_3	Cerac	99.9 %	·

Table 3-2 Chemical compositions of RBM mixtures explored

Sample Name	Composition (wt%)				
	MREO	Mullite seeds	Al_2O_3	SiO_2*	Si
RBM 1	5	5	72.80	7.19	10.01
RBM 2	7.5	5	69.08	10.78	7.64
RBM 3	7.5	7.5	66.97	10.78	7.25
RBM 4	5	7.5	70.69	7.19	9.62
RBM 5	10	5	65.34	14.38	5.28
RBM 6	10	7.5	63.23	14.38	4.89
RBM 7	5	10	68.43	7.19	9.38
RBM 8	7.5	10	64.85	10.78	6.87
RBM 9	10	10	61.12	14.38	4.5

* In the eutectic powder

The chemical compositions of the RBM mixtures explored are listed in Table 3-2. The starting mixes were vibro-milled in ethanol for 24 hrs with alumina balls. After drying they were uniaxially pressed at 15 MPa and isostatically pressed at 200 MPa to pellets 8 mm diameter. 25×5×3 mm bars were also made for dilatometry. Specimens were fired 1200 - 1300 °C for 5 hrs in air employing the following heating cycle: Room temperature to 700 °C (5°C/min), 1200~1300 °C (1 °C/min, 5 hrs hold), cooling to room temperature (10 °C/min). Silicon oxidation initiates ≅ 700 °C (Mechnich et al 1998), so a slow heating rate (1 °C/min) was used thereabout. The heating schedule employed is illustrated in Fig 3-1.

3-3 Interface Reaction Couples of the MREO Eutectic and Mixtures of Al_2O_3, Si (or SiO_2)

To investigate the reaction morphology and the mechanism of RBM reaction, layered specimens were made. Four compositions of Al_2O_3 and Si (or SiO_2) were formulated (Table 3-3). S1-S4 were vibro-milled for 1 day. The layered specimens were pressed of Al_2O_3, Si (or SiO_2)/Pt paste/MREO eutectic/Pt foil/Al_2O_3, Si (or SiO_2). Sample composition schematics are presented in Fig. 3-2. The Pt paste acts as a marker and the Pt foil as an isolation layer to compare reactions between the S1-S4 composition and the MREO eutectic.

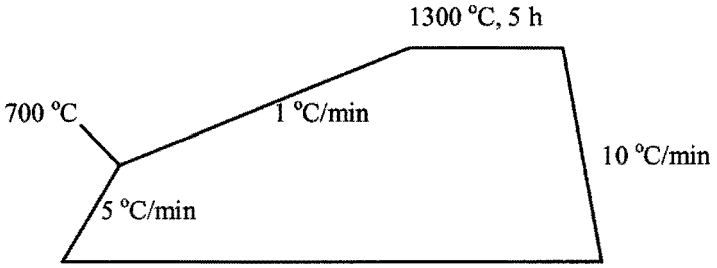

Fig. 3-1. Heat treatment cycles of reaction bonded mullites.

Table 3-3 The oxide compositions of the top and bottom layer of the layered pellets

Sample name	Al_2O_3	SiO_2	Si	Mullite seeds
S1	71.8	28.2	·	·
S2	89.3	·	10.7	·
S3	75.0	19.2	·	5.8
S4	83.5	·	9.6	6.5

S1
Pt foil
MREO Eutectic
Pt paste
S1

S2
Pt foil
MREO Eutectic
Pt paste
S2

S3
Pt foil
MREO Eutectic
Pt paste
S3

S4
Pt foil
MREO Eutectic
Pt paste
S4

Fig. 3-2. The configurations of the stacked specimens.

The top and bottom layers, are compared after heat treatment. Samples S1-S4 were pressed and Pt paste spread on the top of each S1-S4 layer. The MREO eutectic was then pressed onto the Pt paste and Pt foil placed thereon. Now the same composition minus the MREO eutectic was introduced onto the Pt foil and each sample again pressed. During stacking, a small uniaxial pressure (15 MPa) was applied followed by isostatic pressing at 200 MPa. The layered specimens were heat-treated in air at 1175, 1200, 1250, 1300, 1350 and 1400 °C for 5, 10, 30 and 90 mins then quenched. Specimens were mounted and vacuum impregnated with epoxy (Fig. 3-3). Samples were then cut in half, the cutting surface ground and polished with SiC paper to allow observation by optical microscope.

3-4 Bilayer pellets to Identify the Roles of the Eutectic and the Mullite Seeds

Bilayer pellets were constructed with Pt foil in the centre. The composition of each layer is listed in Table 3-4. The configurations of the pellets investigated are illustrated in Fig. 3-4. Pellets were prepared by the same procedure. Sintering was carried at 1300 °C for 5 hrs in air. X-ray diffraction patterns were taken of each layer and the densities of the resultant specimen were measured.

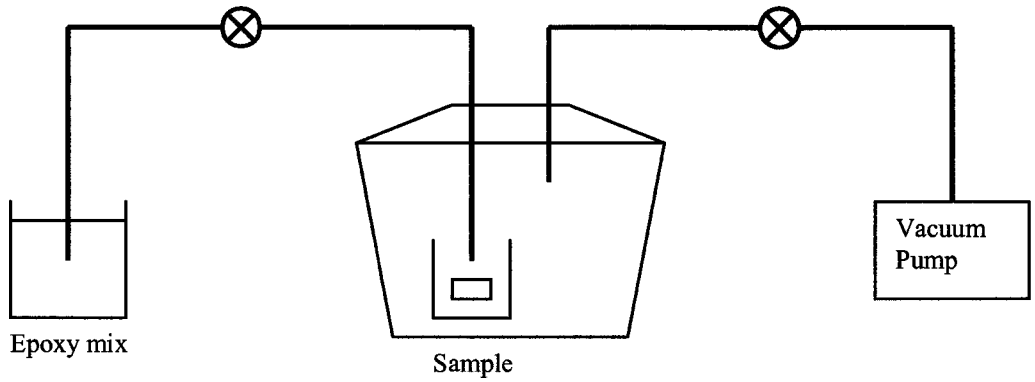

Fig. 3-3. Schematic diagram of the vacuum impregnation.

Table 3-4 The compositions of the layers in bimodal pellets

Layer	Al_2O_3	Si	Eutectic	mullite seeds
Al_2O_3/Si	84.5	15.5	·	·
Al_2O_3/Si/eutectic	67.7	8.1	24.8	·
Al_2O_3/Si/seeds	79.7	8.9	·	5.8
Al_2O_3/Si/eutectic/seeds	63.9	7.7	23.4	5

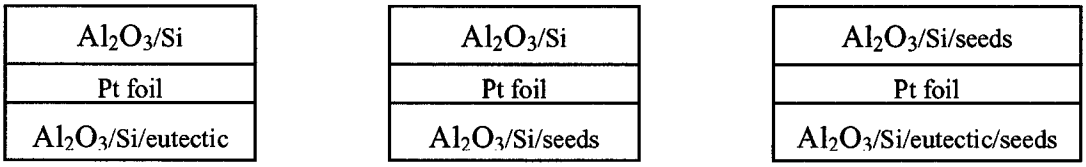

Fig. 3-4. The configurations of bimodal pellets.

3-5 Material Characterization

3-5-1 Specific Surface Area

The specific surface area was determined by the BET method (Autosorb Automated Gas Adsorption System).

3-5-2 Thermal Analysis

Differential thermal analysis (DTA) and thermogravimetric analysis (TGA) were performed on powder samples using a Netzsch Thermal Analyzier. The heating rate utilised was 5 °C/min and 1 °C/min. The same heating schedule was used for RBM sintering.

3-5-3 Dimensional Change Measurement

Shrinkage was measure with a micrometer (± 0.001 mm). Dimensional change (linear length) was recorded by dilatometer (Theta Dilatronic). The heating cycle employed was the same as for RBM.

3-5-4 Phase Determination

The phases present in the sintered sample pellets were determined by X-ray diffraction using copper K_α radiation (Rigaku Miniflex). A slow scan (0.5 °/min) was used to provide data for calculation of the quantitative level of mullite and α-Al_2O_3 present.

3-5-5 Electron Microscopy

The phase development in the RBM mixtures was observed by transmission electron microscopy (Philips CM12, 120 kV). The final sintered morphology was explored by TEM.

3-5-6 The Morphology of the Interfacial Reaction

The interface morphology of the reaction between the MREO eutectic and Si (or SiO_2) was followed by optical microscopy (Leitz Wetzlar).

3-5-7 The Compositional Profile of the Reaction Layer

Interface reaction profiles were defined by a Philips Environmental SEM system 2020. The compositional line profiles through the interface reaction layer were determined via Energy Dispersive X-ray Spectra (EDX).

CHAPTER 4

Results and Discussion

4-1. Reaction-Bonded-Mullite

4-1-1. Eutectic of Al_2O_3-SiO_2-MREO

Pure, rare-earth oxides, Y_2O_3 or CeO_2 accelerate the reaction-bonding of mullite (Rundgren et al. (1988), (1990), Ishibashi et al. (1989), Kurihira et al. (1989) and Mechnich et al. (1998), (1999)). The latter used Y_2O_3 or CeO_2 and discussed the role of transient liquid phase via the reaction between Y_2O_3 and Al_2O_3/SiO_2 or CeO_2 and Al_2O_3/SiO_2 after Si oxidation. This liquid phase promoted mullite formation and densification, but the liquid-formation temperature is high (1345 °C for Y_2O_3 from the phase diagram of Y_2O_3-Al_2O_3-SiO_2 system). Petry and Mah (1999) showed the degradation of Nextel on thermal exposure increases above 1300 °C. The Si oxidation temperature (maximum ≅ 1150 °C) is lower than their liquid formation temperature (1345°C) so this temperature is not necessary to induce Si oxidation. When the liquid forms residual Si is oxidised. The present work is predicated on RBM processing below

1300 °C. So commercially-available, mixed-rare-earth oxide was employed to produce a lower eutectic temperature.

Pure-rare-earth-oxides (Pr_6O_{11} and Eu_2O_3) and mixed-rare-earth-oxide were mixed with Al_2O_3 and SiO_2 in eutectic proportion and differentially thermal analysed to locate the eutectic point precisely (Fig. 4-1, 4-2 and 4-3). The endothermic onset temperatures observed were 1200 °C, 1240 °C and 1133 °C for Pr_6O_{11}, Eu_2O_3 and mixed-rare-earth-oxide (with Al_2O_3/SiO_2), respectively. And actual melting temperatures are 1224 °C, 1259°C and 1175 °C, respectively. As expected, the mixed-rare-earth-oxide eutectic temperature is lower. Liquid phase formation during Si oxidation could enhance the process and reduce the RBM temperature. The particle size of the raw eutectic mixture is important as reaction rate depends thereupon. For example, the silicon dioxide thickness on Si particles increases with time at constant temperature, thus fine Si particles will oxidise faster than coarse ones. The as-received Si particles utilised were larger than the other starting powder materials so they were vibro-milled with the Al_2O_3 for 10 days before use.

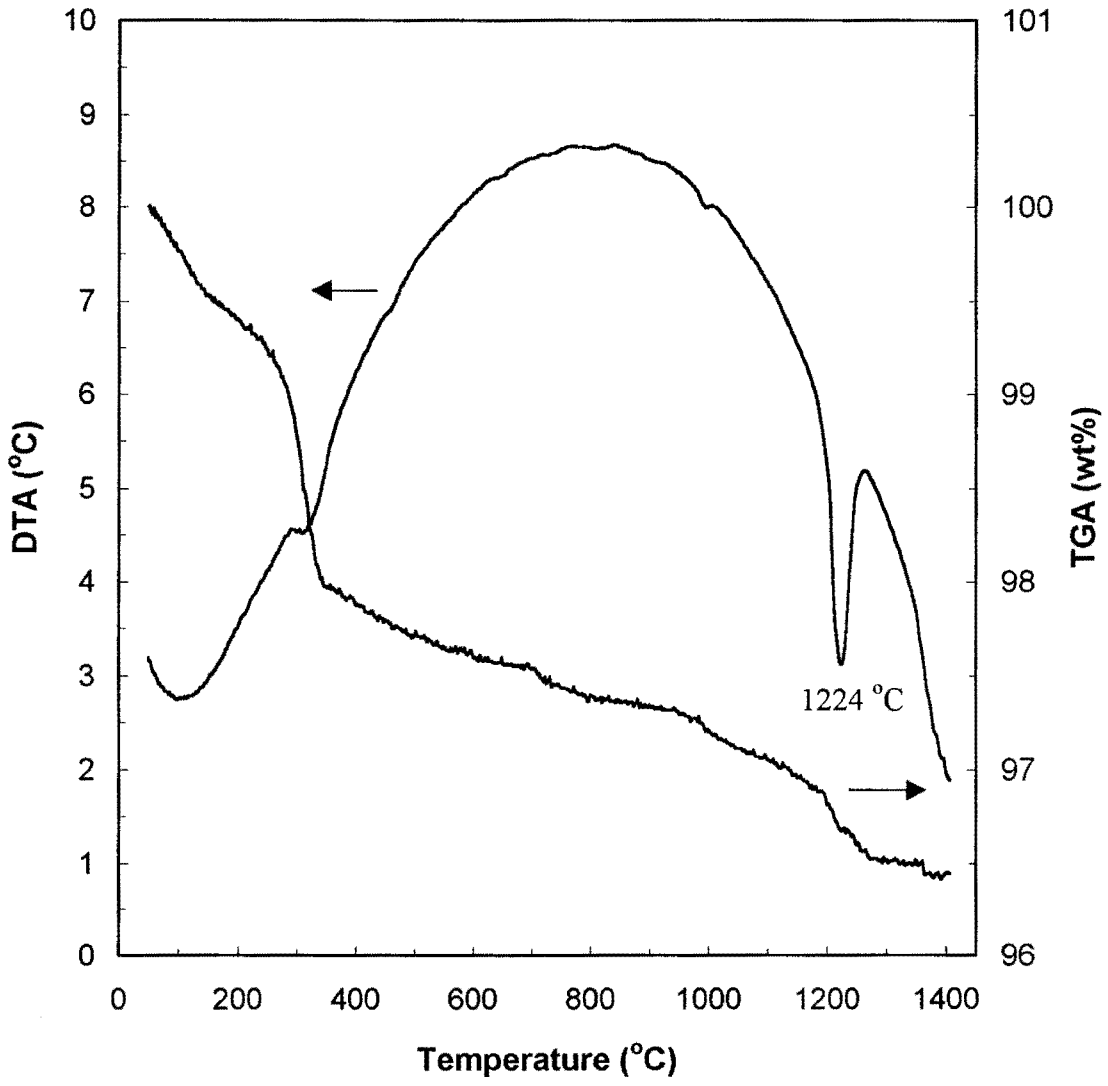

Fig. 4-1. Differential thermal analysis and thermogravimetric analysis curves for eutectic composition of Al_2O_3-SiO_2-Pr_6O_{11} system.

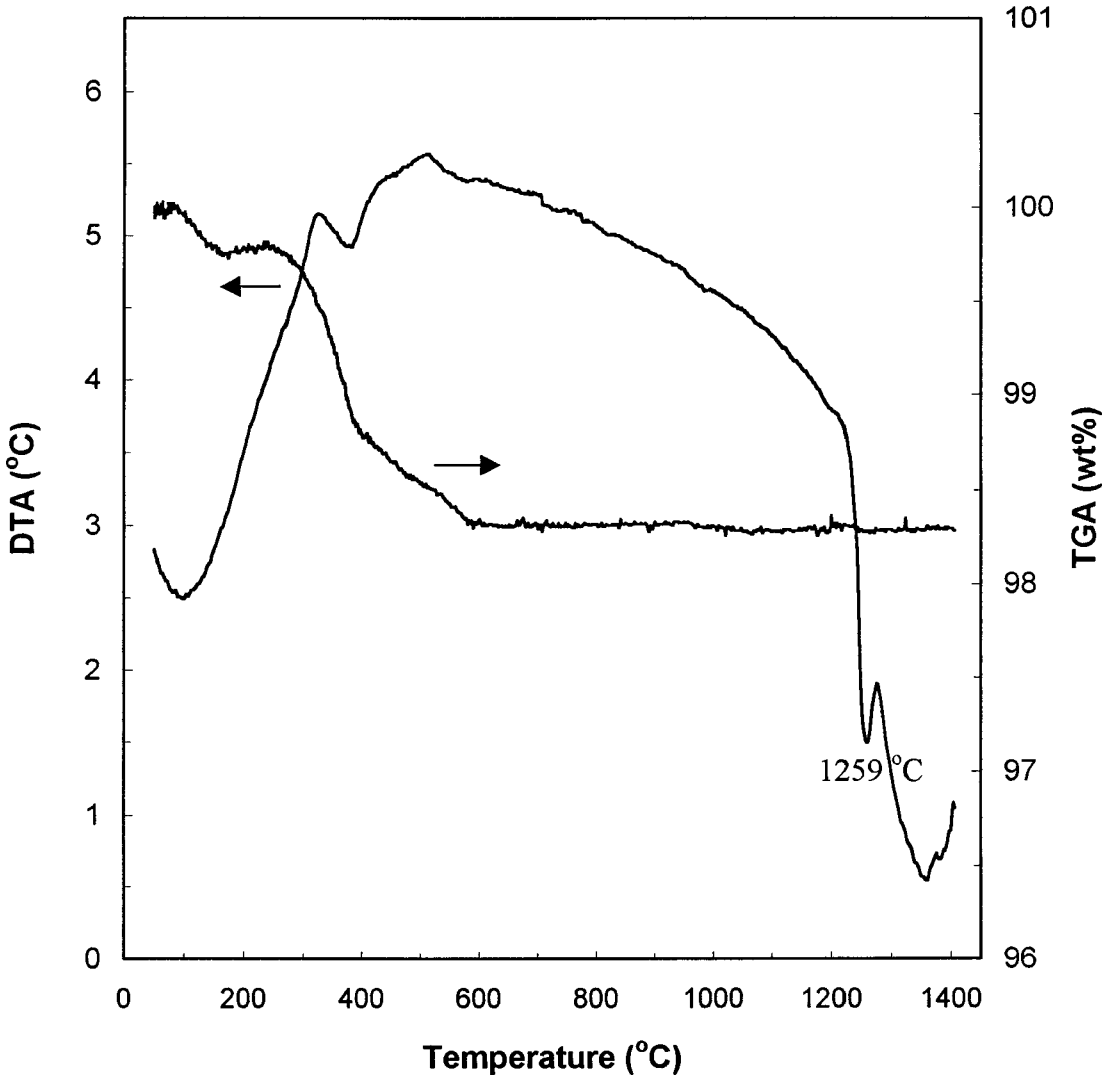

Fig. 4-2. Differential thermal analysis and thermogravimetric analysis curves for eutectic composition of Al_2O_3-SiO_2-Eu_2O_3 system.

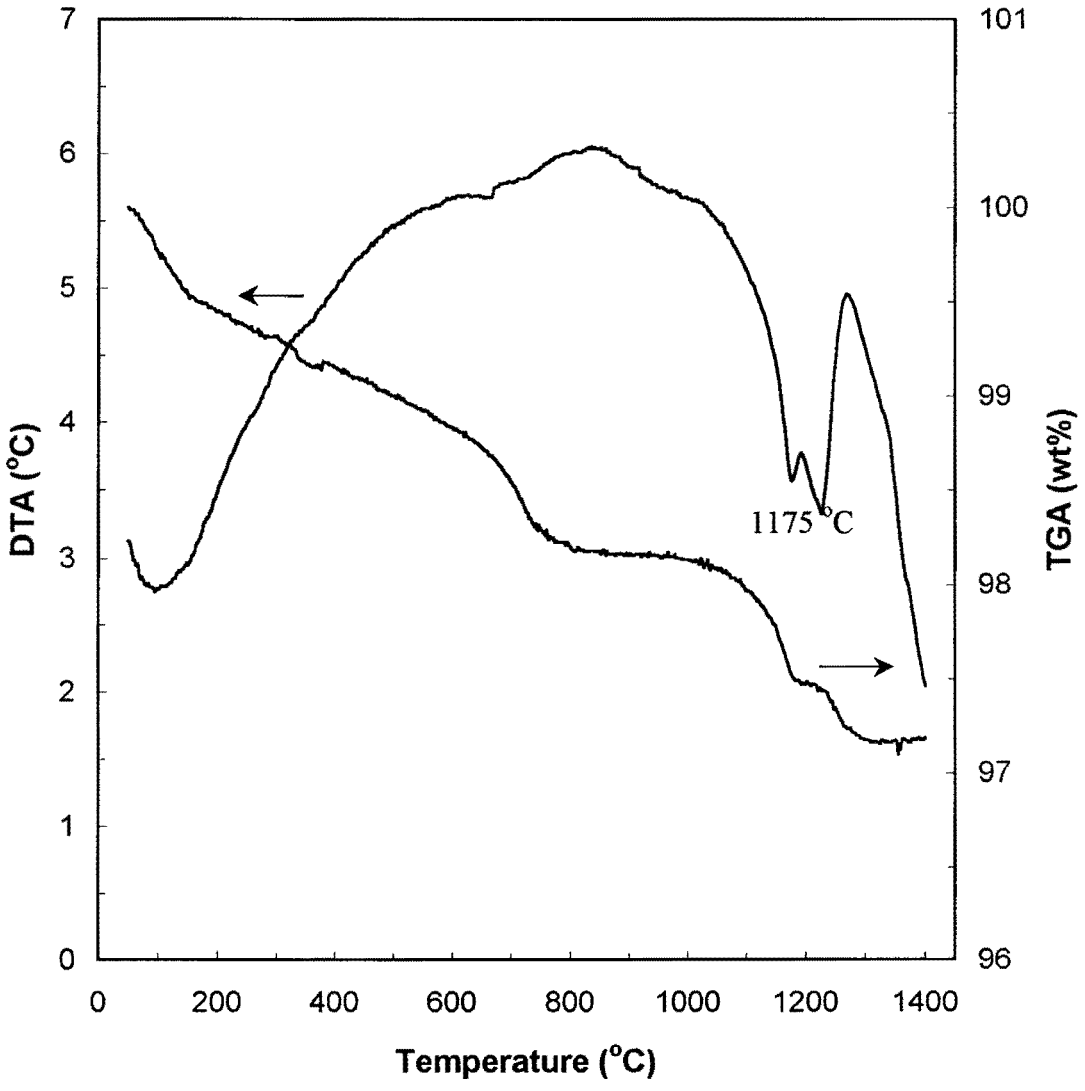

Fig. 4-3. Differential thermal analysis and thermogravimetric analysis curves for eutectic composition of Al_2O_3-SiO_2-MREO system.

4-1-2. The Densification Characteristics of Mixed-Rare-Earth Based Reaction-Bonded Mullite (RBM)

Fig. 4-4 shows the density (% theoretical) vs. sintering temperature for the RBM mixtures explored (1-4) (see Table 3.2 for compositions). The densities of RBM 2 and 3 (7.5 w/o mixed-rare-earth-oxide (MREO)) increase with temperature to an optimum ≅ 1250 °C. The density of RBM 2 is 90 % theoretical. This is the best density reported for RBM ceramics fired < 1300 °C.

Higher % MREO resulted in higher density (RBMs 2 and 3 vs. 1 and 4) as the increased liquid phase accelerates Si oxidation, mullite formation and sample densification. Samples containing higher % mullite-seeds exhibited lower density (RBM 3 vs. 2, and 4 vs. 1) as the seeds promote acicular mullite formation and growth rather than densification, ie; they rendered the sinter more refractory. The net shrinkage was 0.99~2.2 %, i.e.; close to net-shape sintering. Thus sintering shrinkage was compensated by Si-oxidation and mullite formation.

Schppokat et al. (1998) obtained 94 %TD for RBM with Al and SiC as an oxidant at 1500 °C. Though the final density is better, the sintering temperature is too high for Nextel fibre. Mechnich et al. (1998) lowered the sintering temperature to 1350 °C but didn't mention the final density of their RBM. They mentioned the porosity was 15 %. In the present study, RBM 2 has 11 % porosity and 91 %TD when sintered at 1300°C.

Fig. 4-5 (density vs. sintering temperature for the RBM mixtures 5-9) supports the results for RBM 1-4. RBM 5 and 6 (10 w/o MREO) have density > 90 % theoretical.

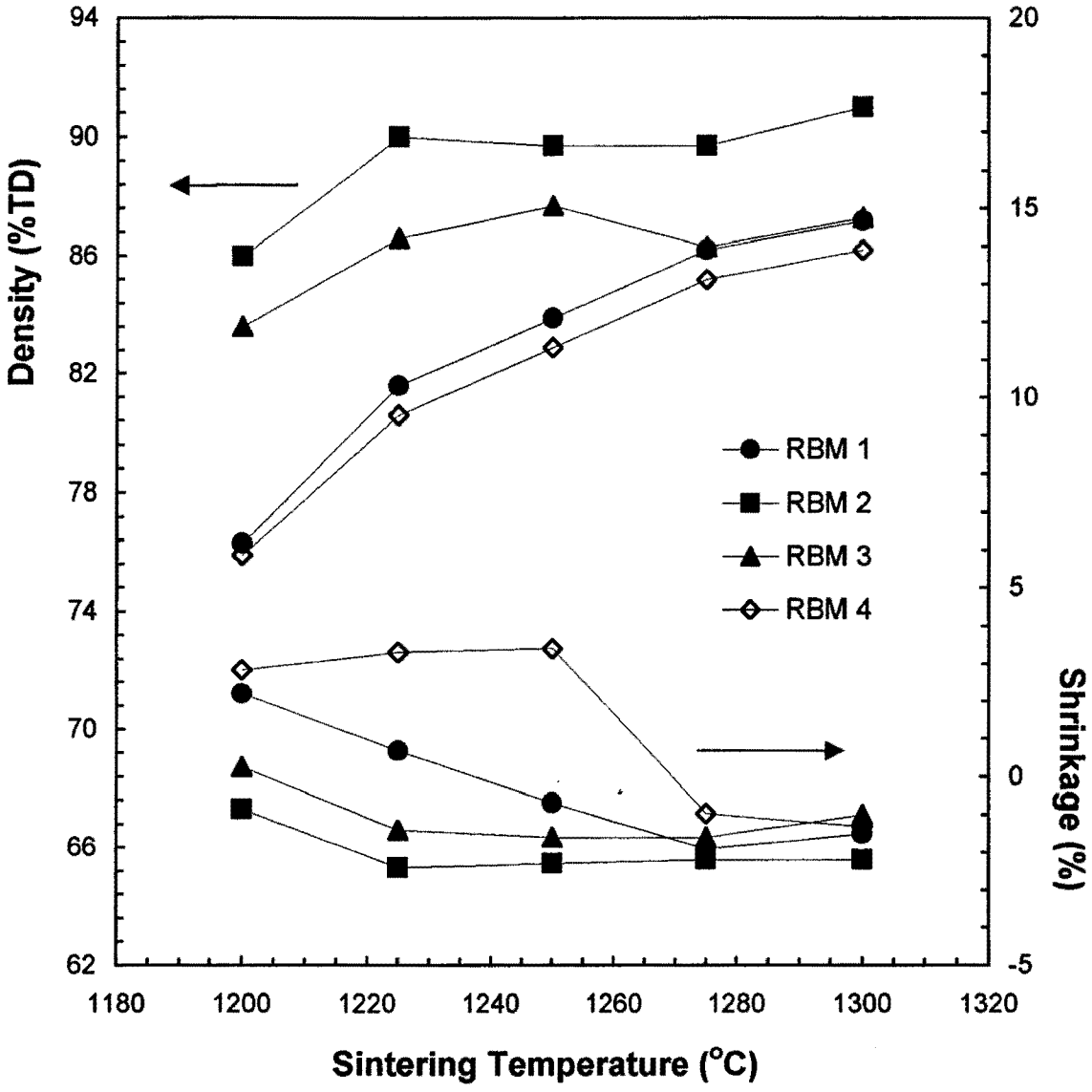

Fig. 4-4. Density and shrinkage vs. sintering temperature for RBM mixtures1-4.

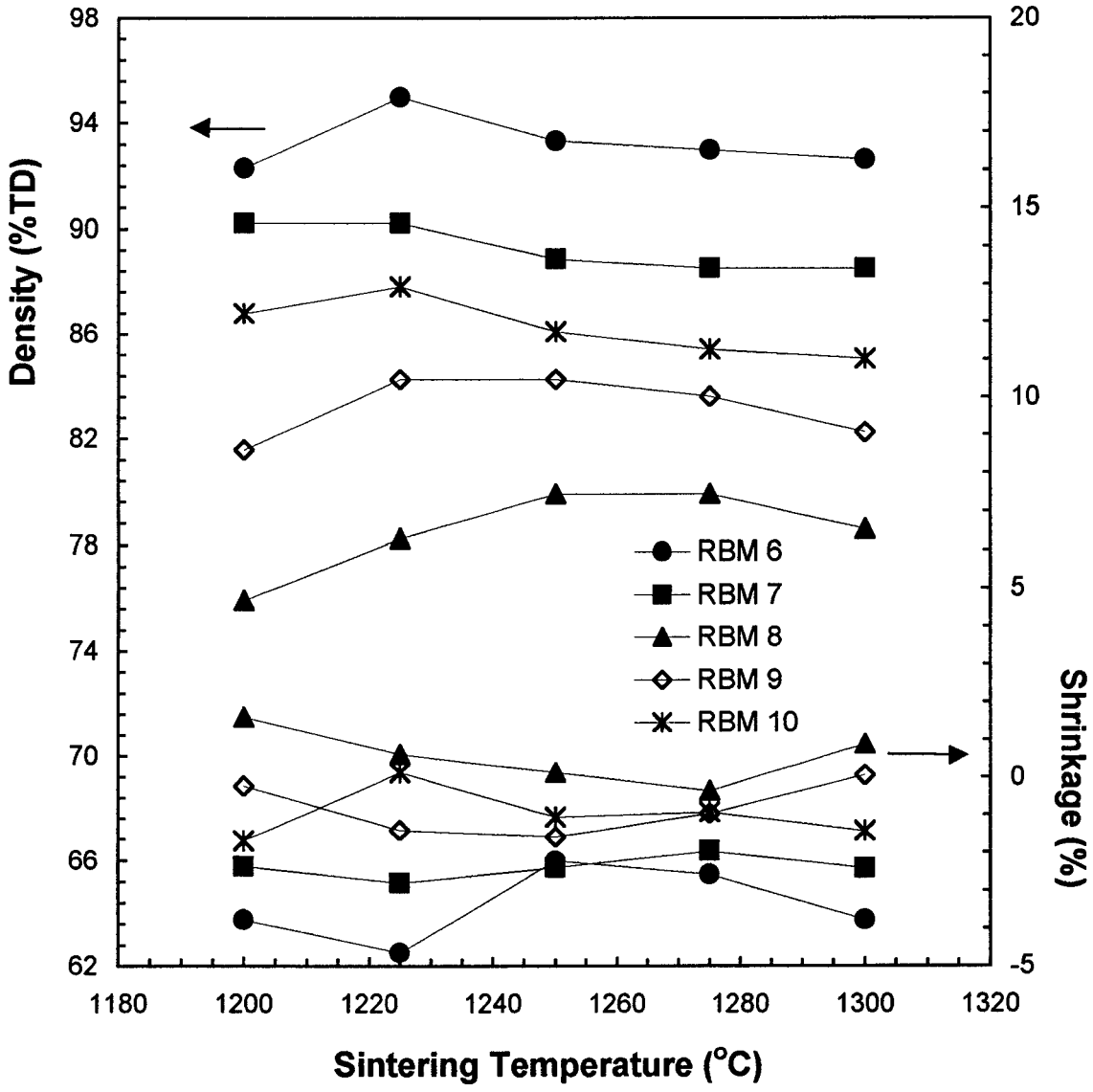

Fig. 4-5. Density and shrinkage vs. sintering temperature for RBM mixtures 5-9.

RBM mixtures 7-9 (10 w/o mullite seeds) exhibit lower density (< 90 %) and shrinkage from +0.88 ~ -3.76 %. RBM 6 and 7 have higher density than RBM 2, but higher shrinkage than RBM 2. Thus, protocol RBM 2 was chosen as optimum for near-zero shrinkage.

4-1-3. The Oxidation Characteristics and Volume Expansion of the Mixed-Rare-Earth-based, RBM Mixtures

TGA results for mixtures RBM 1, 2, 3, and 4 are shown in Fig. 4-6, and for RBM 5,6,7,8, and 9 in Fig. 4-7. Silicon oxidation is responsible for the weight gain with temperature. The average particle size of Si is 0.63 μm. From the oxidation results of Si by Deal and Grove (1965), the Si need at least 3 hrs for oxidation at 1200 °C. Almost complete oxidation is achieved after 1300 °C for 5 hrs. The final weight gain should equal that due to the oxidation of the Si content. The final weight gains observed and those calculated via

$$Si + O_2 \rightarrow SiO_2 \text{ (113.9 \% weight increase)}$$

are summarised in Table 4-1. The differences are 0.3-1.47 w/o. The observed values are lower than the theoretical ones because the initial Si powder is partially oxidised. RBM 5-9 are less oxidised than RBM 1-4, as the Si powder of the former oxidise more than the latter before mixing. The less the SiO_2 on the Si powder, the better for RBM, as expansion is optimised.

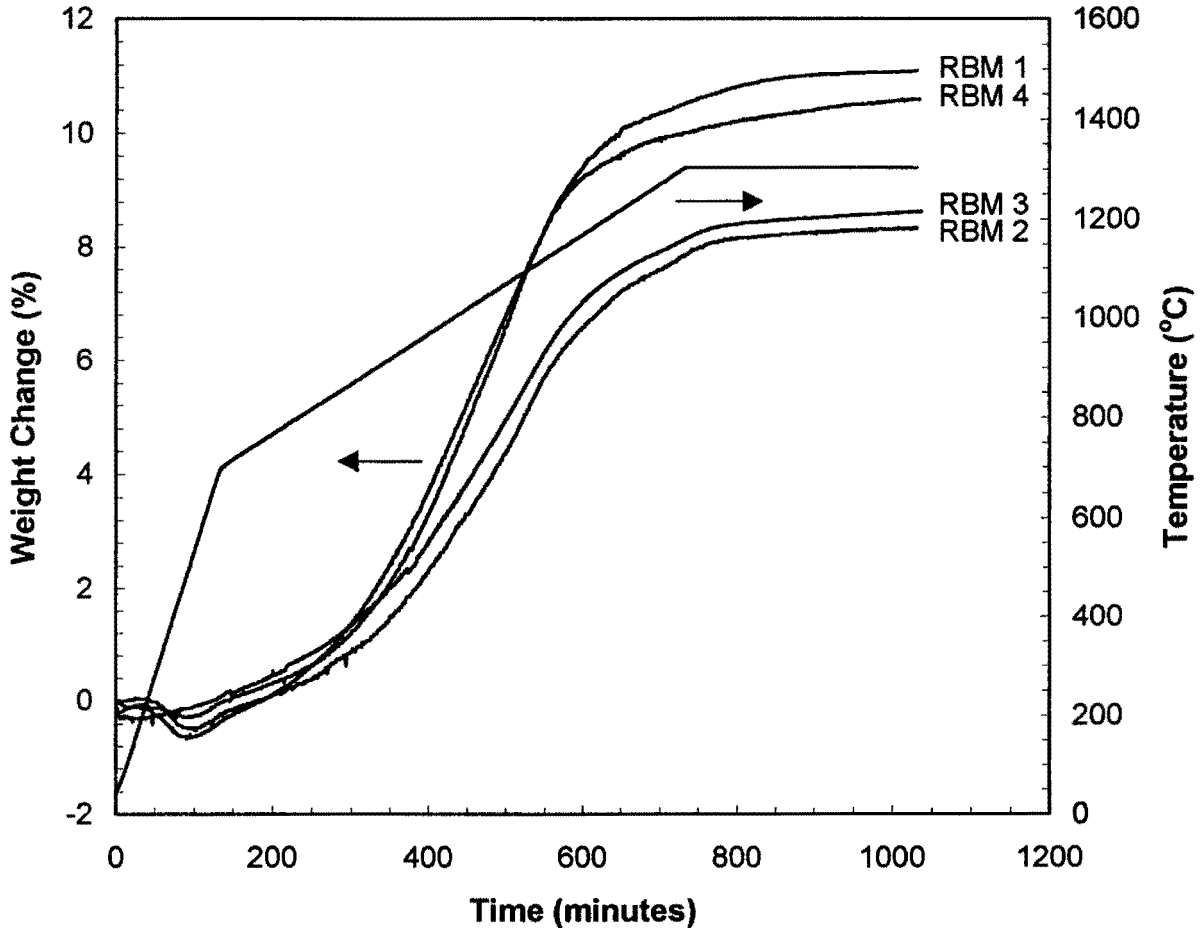

Fig. 4-6. Thermogravimetric analysis (TGA) for RBM 1-4 Samples.

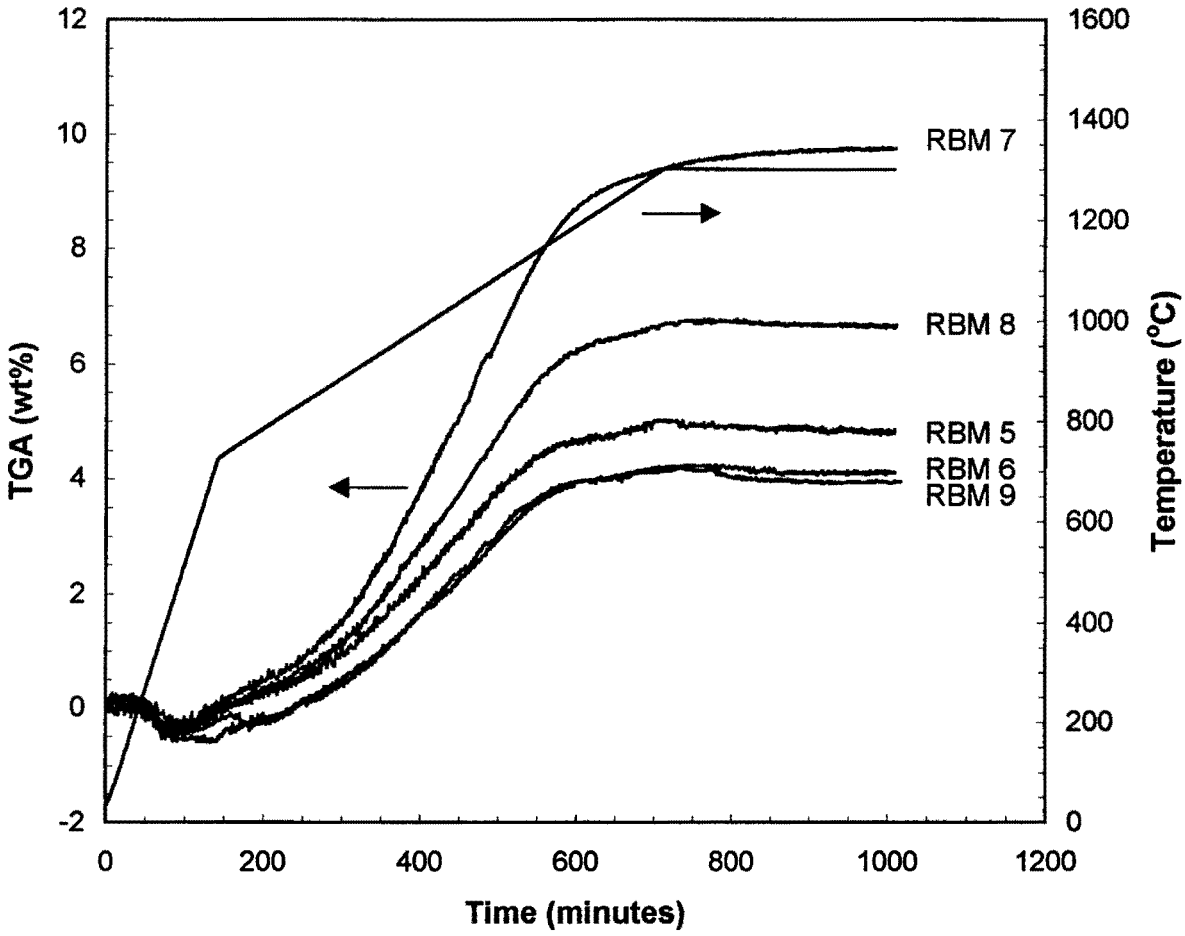

Fig. 4-7. Thermogravimetric analysis (TGA) for RBM 5-9 Samples.

Table 4-1 Differences between theoretical and observed weight gains

Specimen	Si content (wt%)	Theoretical weight gain (wt%)	Observed weight gain (wt%)	Degree of oxidation (% of theoretical)
RBM 1	10.01	11.40	11.1	97.4
RBM 2	7.64	8.70	8.4	96.6
RBM 3	7.25	8.26	8.6	95.9
RBM 4	9.62	10.96	10.59	96.6
RBM 5	5.28	6.01	4.9	81.5
RBM 6	4.89	5.57	4.1	74.0
RBM 7	9.39	10.66	9.8	91.9
RBM 8	6.87	7.82	6.7	86.0
RBM 9	4.50	5.126	4.0	78.0

Mechnich et al. (1998) detected a sudden weight gain for Y_2O_3- and CeO_2-doped samples near sintering temperatures. TGA in this study did not show this. The sudden weight gain is explained by the Si not oxidising until near the sintering temperature when liquid phase forms. This liquid phase thus enhances the Si oxidation, so a sudden weight gain is observed when the liquid forms (1345 °C for the Y_2O_3). No sudden weight gain was observed in the present work, though complete oxidation was achieved. This is because the onset melting temperature of the mixed-rare-earth-eutectic (1133 °C) is lower than the sintering temperature (1300 °C) so liquid phase appears and promotes Si oxidation continuously from the lower temperature.

Dimensional changes for the RBM samples were determined by dilatometer (Figures 4-8 and 4-9) and compared with the data for reaction sintered mullite (RSM). All RBM specimens exhibit a length increase followed by sintering shrinkage. The RSM sample exhibited shrinkage alone. Thus, in RBM, the sintering shrinkage is compensated by the expansion. The latter involves Si oxidation and mullite formation from the Al_2O_3 and "SiO_2". Silicon oxidation is the main contributor to the expansion as its magnitude is much higher than that due to mullite formation, i.e.;

$$Si + O_2 \rightarrow SiO_2 \text{ (116 \% volume expansion)}$$

$$3Al_2O_3 + 2SiO_2 \rightarrow 3Al_2O_3 \cdot 2SiO_2 \text{ (4.2 \% volume expansion).}$$

RBM 1 and 4 display the maximum length increase (5.88 % and 5.93 % at 1145 °C and 1141 °C respectively). RBM 2 and 3 have 4.94 % and 5.02 % length gain at 1124 °C and 1120 °C respectively. The maximum expansion for RBM 2 and 3 occurs at lower

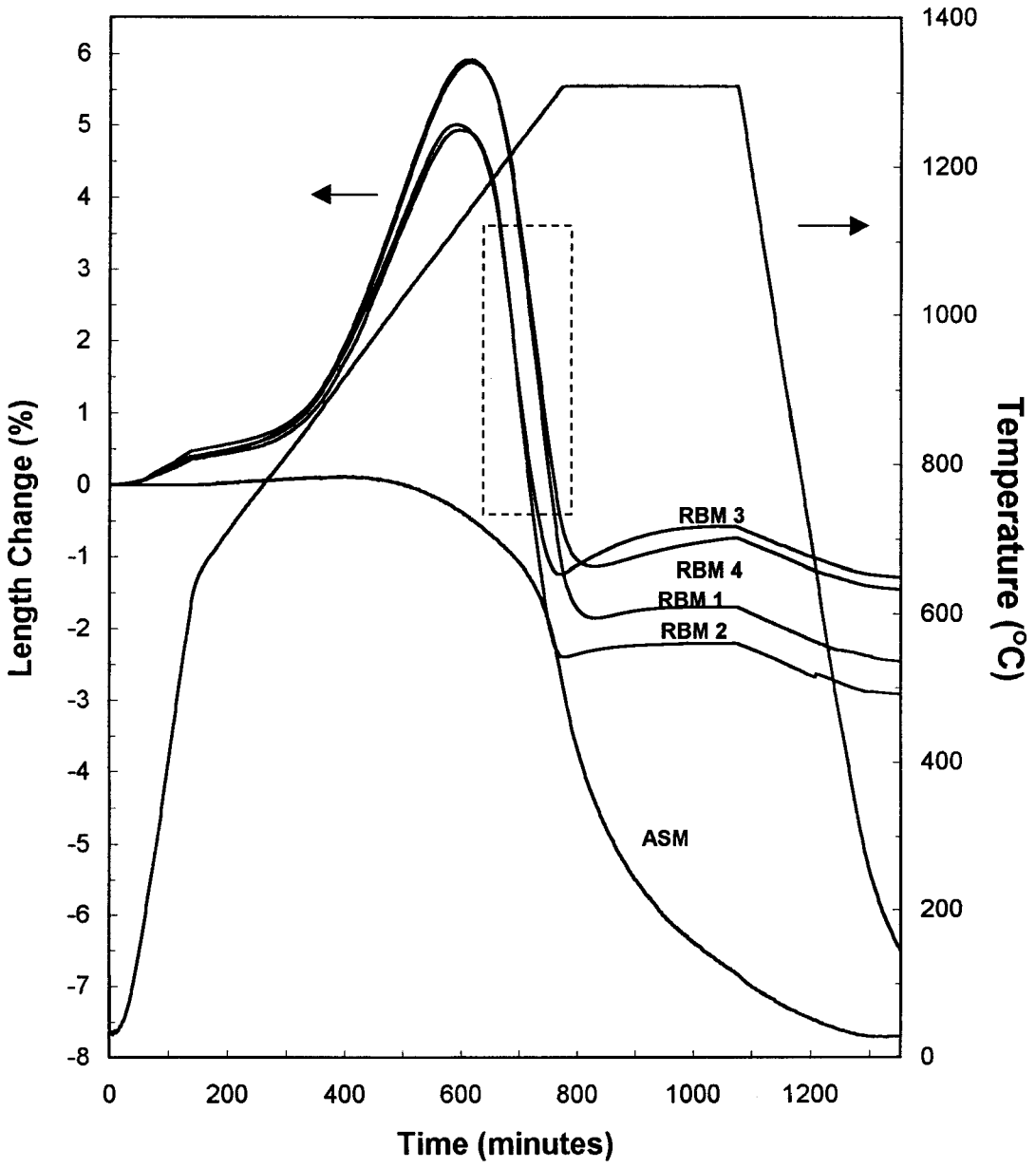

Fig. 4-8. Dilatometric measurement curves of RBM 1-4 samples (The straight line segment plot is the time/temperature profile of the apparatus, Dotted box is shown in Fig. 4-10).

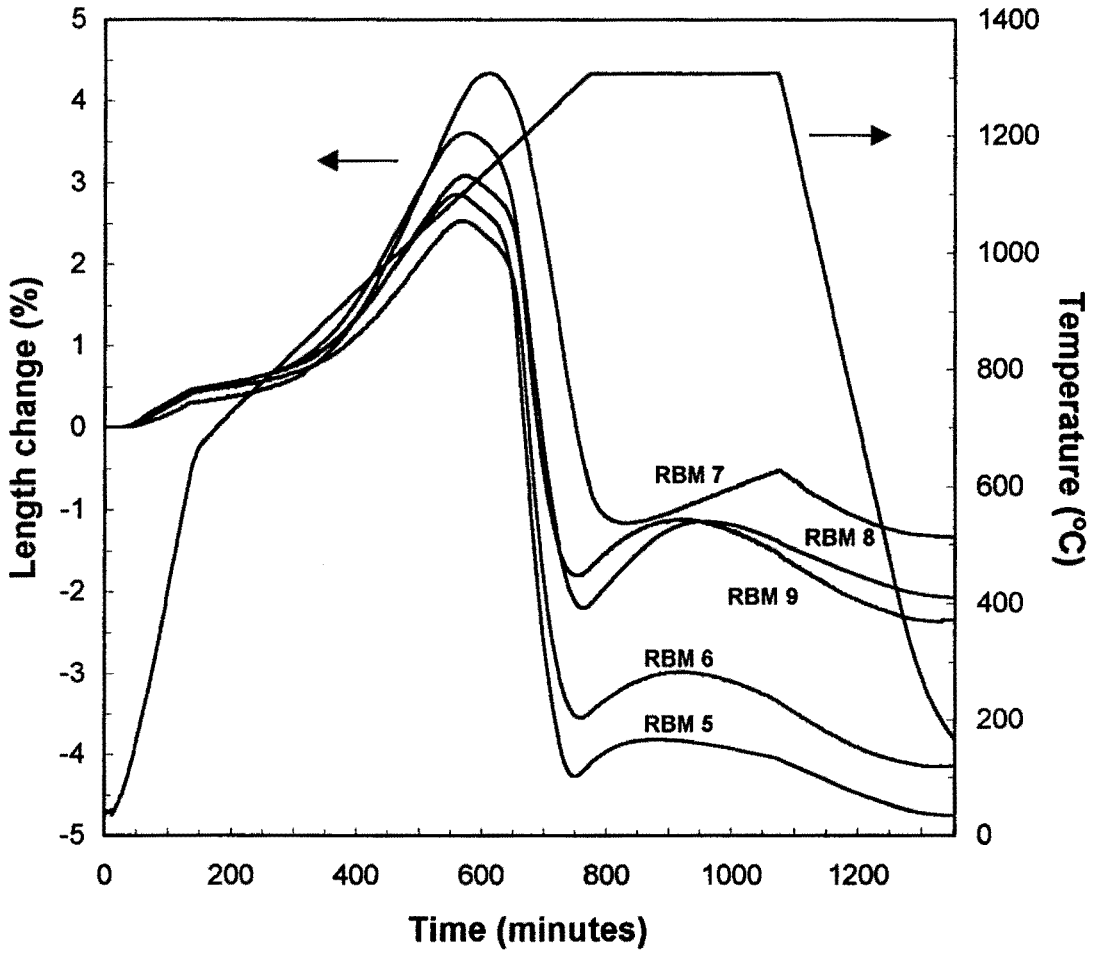

Fig. 4-9. Dilatometric measurement curves of RBM 5-9 samples (The straight line segment plot is the time/temperature profile of the apparatus).

temperatures than for RBM 1 and 4 as the former contain more mixed-rare-earth-oxide, so the more liquid that forms the more enhanced is the Si oxidation at lower temperatures. All samples sinter after maximum expansion but RBM 2 and 3 cease to shrink before RBM 1 and 4.

Al_2O_3 and SiO_2 react to form mullite with 4.2 % volume expansion. RBM 1 and 4 exhibit smaller length increases than RBM 2 and 3 and their length is still increasing at the end of the sintering temperature hold. RBM 2 and 3, on the other hand, exhibit an initially fast length change but finally flat-line, ie. mullitisation is almost complete. From these results, RBM 2 and 3 (more MREO) react faster than RBM 1 and 4. Samples in which the liquid phase forms first, will enjoy enhanced diffusion thus the rate of reaction (oxidation, mullitisation), is increased. This directly correlates with the level of MREO in the mixture.

Brandt and Lundberg (1996) showed low length expansion (2.8%). Mechnich et al. (1998) detected initial length increase at ≅ 700 °C and an overall 2.5-3.5 % length change. Such low expansion cannot compensate for sintering-induced shrinkage. They showed that Ce-doped RBM displayed a shrinkage of > 7 %. RBM 1-4 exhibit an initial length increase at ≅ 250 °C, 5-6 % length expansion but only 1.2-2.8 % shrinkage. The sintering shrinkage is less due to the higher expansion. Dilatometric measurements for RBM 5-9 samples (Fig. 4-9.) have similar tendencies to RBM 1-4 so discussion for shrinkage mechanism will now concentrate on RBM 1-4.

Diffusion-controlled shrinkage is proportional to $r^{-4/3}$ (particle size) and $t^{1/3}$ (sintering time) and dissolution- controlled shrinkage is proportional to r^{-1} and $t^{1/2}$ as

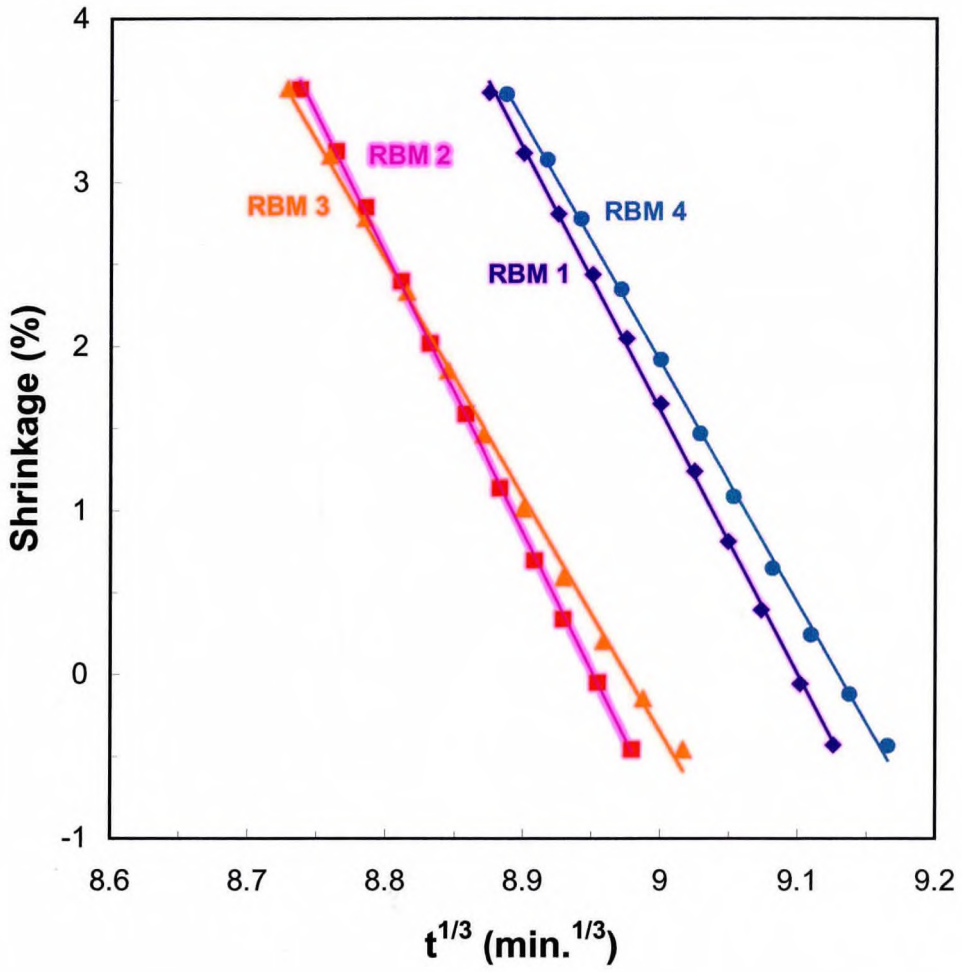

Fig. 4-10. Shrinkage vs. $t^{1/3}$ plots of RBM 1-4 samples.

mentioned in the literature review. Thus the diffusion-controlled process is more sensitive to particle size and exhibits faster reaction than the dissolution-controlled process. In the present results, shrinkage curves of all RBM were found to follow $t^{1/3}$ rather than $t^{1/2}$ (Fig. 4-10). The shrinkage of RBM is even faster than $t^{1/3}$. Therefore, RBM samples fit the diffusion-controlled shrinkage model.

4-1-4. Phase Evolution in the RBM Mixes

Si oxidizes to SiO_2 with temperature up to 1150 °C, so this temperature should be that of maximum expansion. This SiO_2 reacts with the Al_2O_3 present to give mullite. X-ray diffraction patterns for a series of quenched RBM 2 mixes are shown in Fig. 4-11. Oxidation-derived SiO_2, α-Al_2O_3 and low levels of mullite are present at 1250 °C, but no MREO peaks are observed. This may be because crystallization thereof took more time. Increasing temperature to 1290 °C, decreased the SiO_2 and α-Al_2O_3 levels and increased the mullite.

The X-ray diffraction pattern for Y_2O_3- and CeO_2-doped RBM quenched from 1300 °C to 1340 °C (Mechnich et al. (1998)) shows a trace of mullite. The X-ray patterns for the present work exhibit a higher intensity of mullite at a lower temperature (1200 °C – 1290 °C).

The X-ray diffraction patterns for all the RBM specimens (1-9) (after 1300 °C for 5 hours) are shown in Figs. 4-12 (RBM 1-4) and 4-13 (RBM 5-9). Intense mullite peaks with minor Al_2O_3 and SiO_2 are observed. α-Al_2O_3 and SiO_2 still exist in RBM 4 and 7

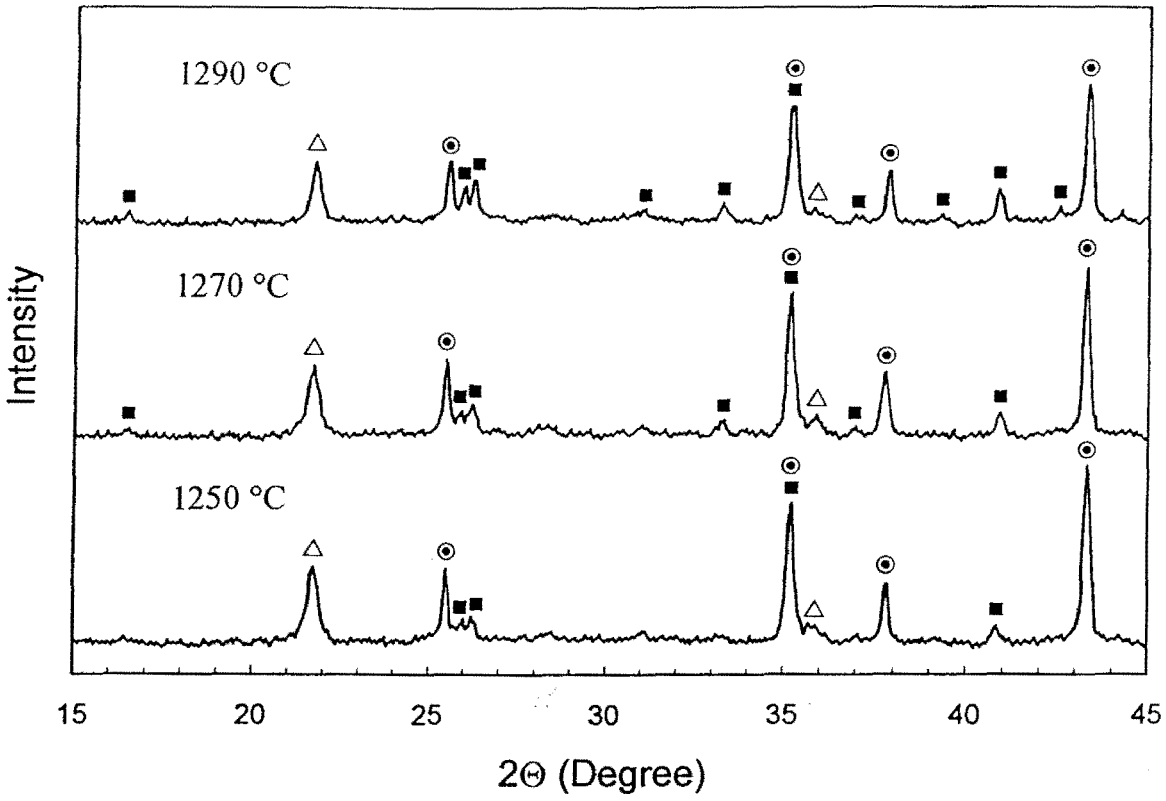

Fig. 4-11. X-ray diffraction patterns of RBM 2 Samples quenched from the indicated temperatures (■: Mullite, ⊙: α-Al_2O_3, △: Cristobalite).

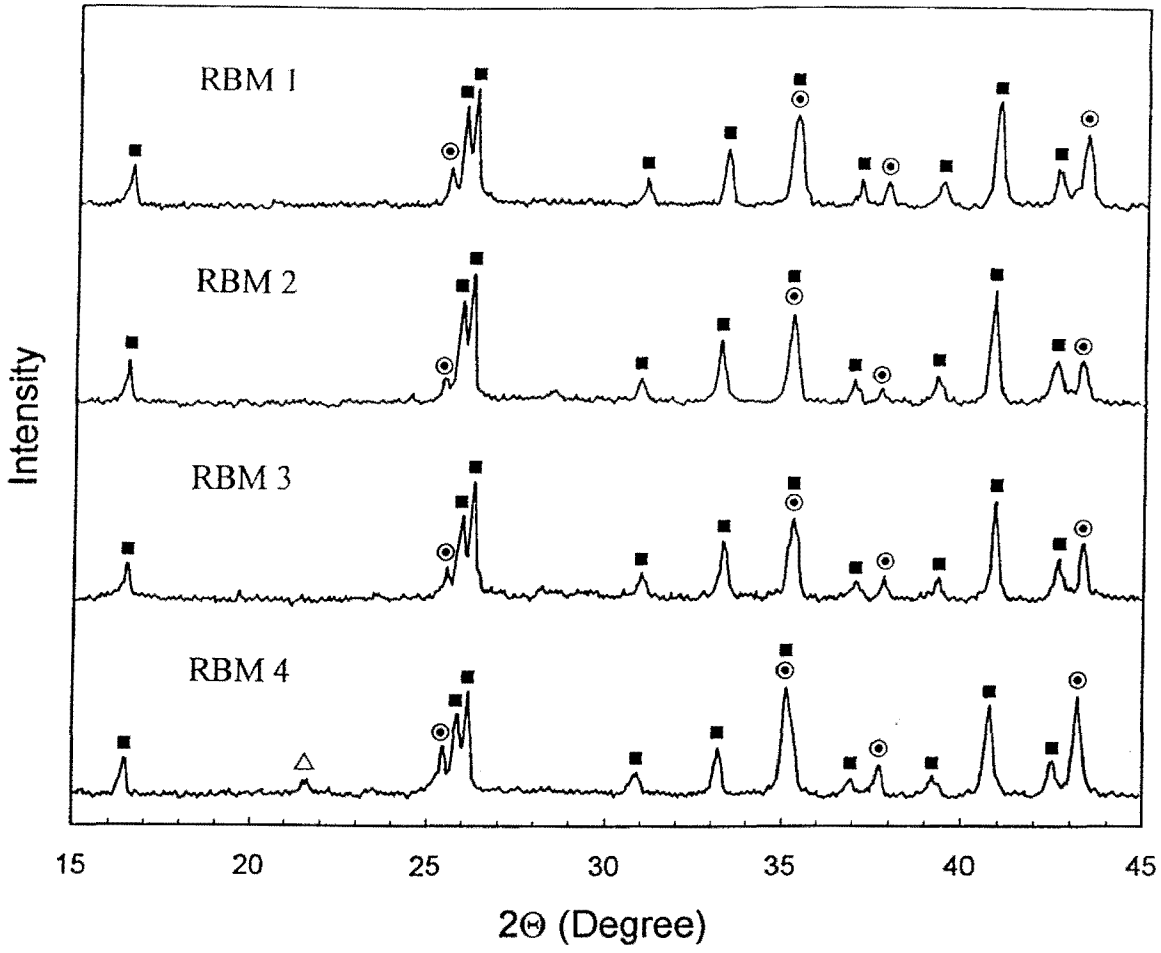

Fig. 4-12. X-ray diffraction patterns of RBM 1-4 samples after heating at 1300°C for 5 hrs (■: Mullite, ⊙: α-Al_2O_3, △: Cristobalite).

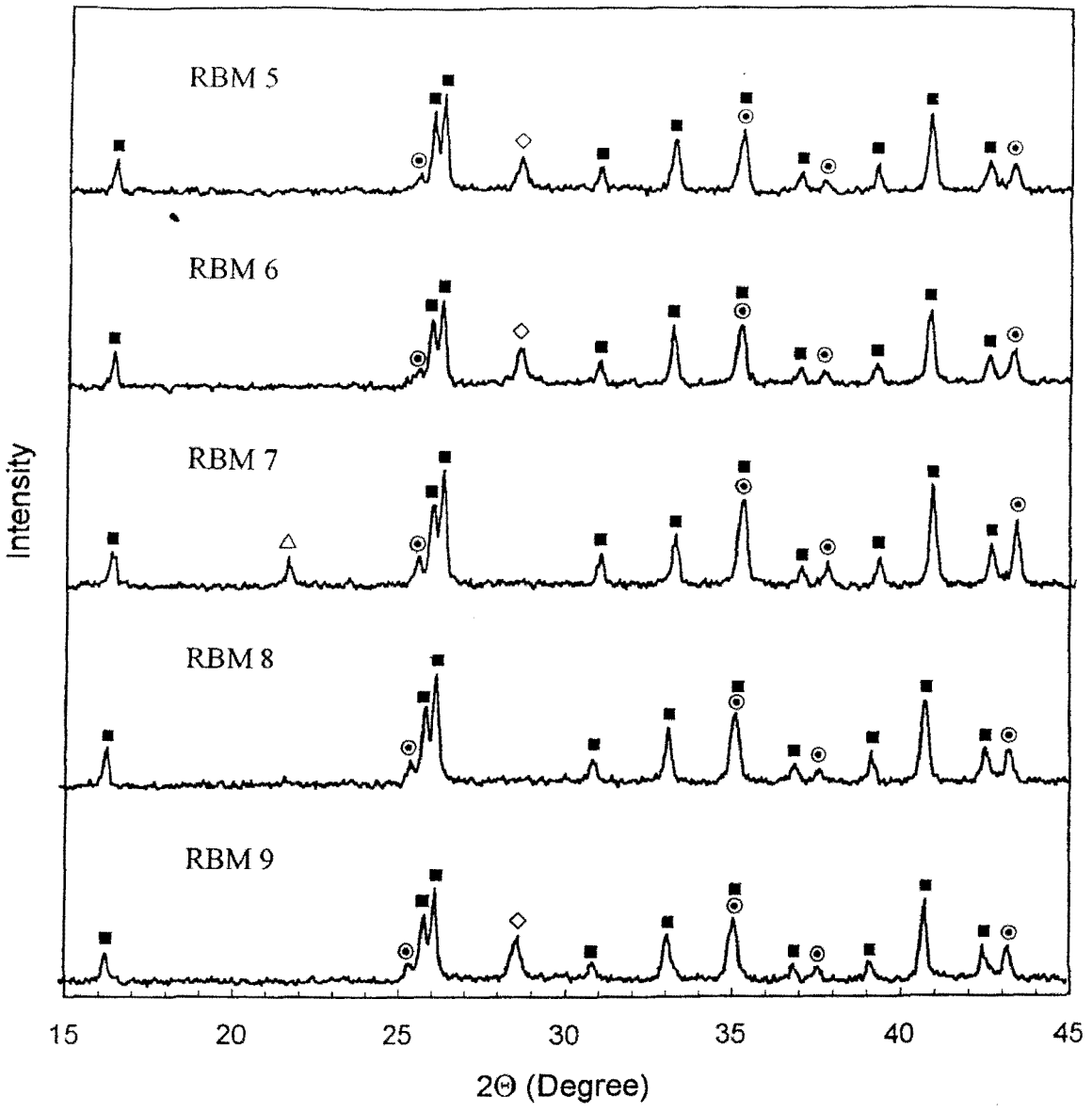

Fig. 4-13. X-ray diffraction patterns of RBM 5-9 samples after heating at 1300°C for 5 hrs (■: Mullite, ⊙: α-Al_2O_3, △: Cristobalite, ◇: REO).

but SiO_2 has completely disappeared from the rest. α-Al_2O_3 is present in all samples though the starting powders (Al_2O_3, SiO_2, Si, MREO, and mullite seeds) were formulated to produce stoichiometric mullite. Possible sources of the excess Al_2O_3 are alumina-ball-milling residue and pre-oxidized Si. RBM samples with > 7.5 w/o MREO show no REO peaks but RBM 5, 6 and 9 (10 w/o MREO) display one, ie; CeO_2 (CeO_2 is the major oxide (48 %) in MREO). RBM 2 contains the lowest residual Al_2O_3.

A major mullite peak was obtained at 1500 °C by Saruhan et al. (1996), by Lathabai and Hay (1996) at 1550 °C, by Mechnich et al. (1998) at 1350 °C and by Scheppokat et al. (1999) at 1500 °C. The present results proved the existence of major mullite ≤ 1300 °C.

4-1-5. Transmission Electron Microscope Observations of the Reactions in RBM Mixes

Fig. 4-14 are electron-micrographs of RBM 2 (7.5 MREO: 5 seeds: 69.08 Al_2O_3: 10.78 SiO_2: 7.64 Si) heat-treated at various temperatures ((a), (b), and (c) quenched from 1250°, 1270°, 1290°C, (d) is a 1300°C-sintered sample after 5 hours). Fig. 4-14 (a) shows small acicular mullite in an Al_2O_3/SiO_2 mixture. The electron diffraction pattern of the acicular phase, shows overlapped patterns of mullite and other phases because the reaction is incomplete (Al_2O_3, SiO_2, mullite seeds and liquid exist). X-ray diffraction data for this sample on quenching also shows a low volume fraction of mullite. Mullite grains (and growth thereof) are observed in the 1270°C-, and 1290°C-quenched specimens

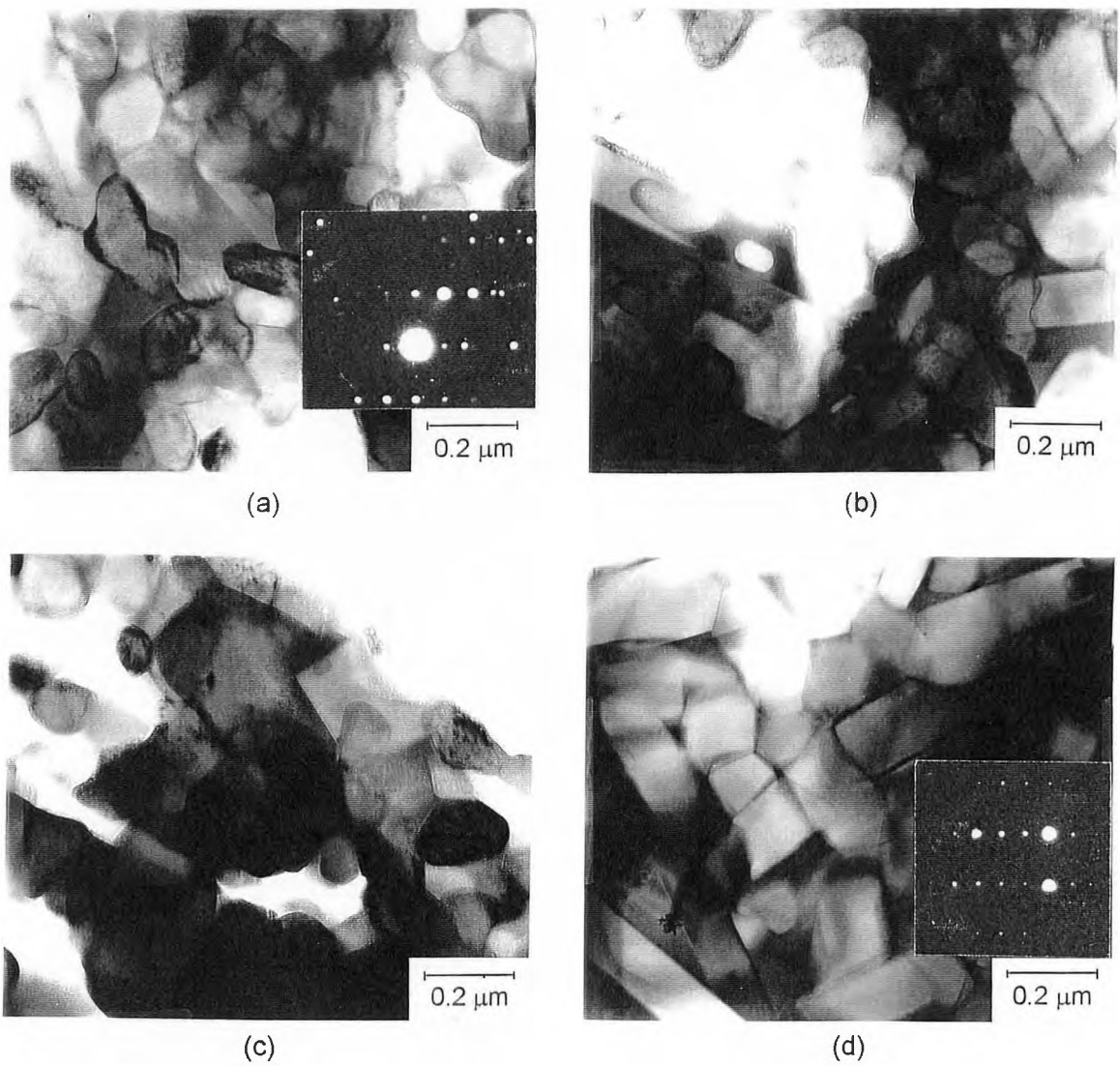

Fig. 4-14. Transmission electron micrographs of samples quenched at (a) 1250°C (inset electron diffraction pattern of Al_2O_3/mullite), (b) 1270°C, (c) 1290°C, and (d) RBM sample sintered at 1300°C for 5 hrs (inset electron diffraction pattern of mullite).

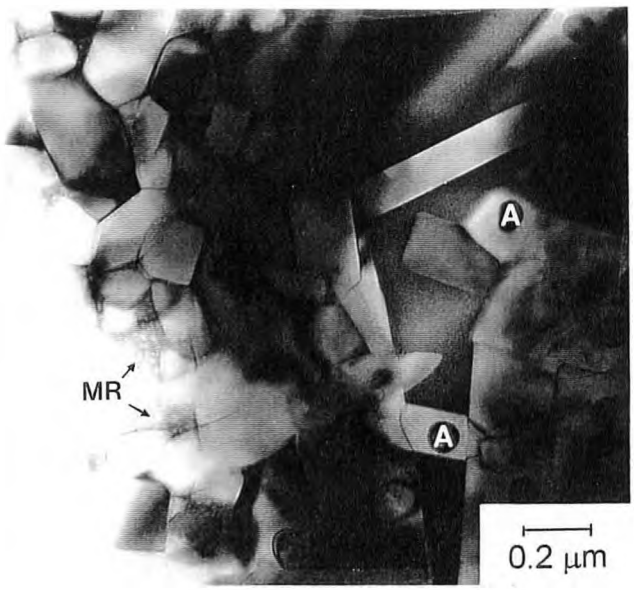

Fig. 4-15. Transmission electron micrograph of RBM 2 sample sintered at 1300°C for 5 hrs.

(Figs. 4-14. (b) and (c)). Fig. 4-14 (d) has 90 vol% mullite from quantitative X-ray analysis. The electron diffraction pattern (Fig. 4-14 (d)) spots were identified as mullite by simulation of low index patterns. The observed electron diffraction patterns are consistent with the X-ray results.

Sintered RBM 2 contains Al_2O_3 between the mullite grains and embedded therein. The latter are the result of grain growth of the former (Fig. 4-15). REO also precipitates on the mullite grain boundaries.

Holz et al. (1996) showed from TEM micrographs that RBM, after sintering at 1550 °C, is characterized by Al_2O_3 particles inside mullite grains. Mechnich et al. (1998) found CeO_2 precipitated along mullite grain boundaries in RBM sintered at 1350 °C. Thus, the microstructure of RBM 2 sintered at 1300 °C in the present study is similar to that reported by Holz sintered at 1550 °C and by Mechnich's sintered at 1350 °C.

The work reported herein was conducted to develop and synthesise reaction-bonded-mullite ≤ 1300 °C so it can serve as a matrix for Nextel 720 fibre-reinforced, mullite-matrix composites. Near-zero shrinkage is required. A near-net-shape process for the production of mullite matrix ceramic composites ≤ 1300 °C has been developed by reaction bonding Al_2O_3, silicon, mullite seeds and a eutectic of Al_2O_3/SiO_2/ mixed-rare-earth-oxides. The liquid phase developed facilitates silicon oxidation, mullite formation and sintering. Thermodynamic analysis of these reactions is discussed in the next section and the role of the liquid phase subsequently explored.

4-2 Thermodynamic Analysis of the RBM Reactions

The reactions involved in RBM are (a) the melting of the eutectic composition, (b) Si oxidation and (c) mullite formation, i.e.;

(b) $Si + O_2 \rightarrow SiO_2$

(c) $3Al_2O_3 + 2SiO_2 \rightarrow 3Al_2O_3 \cdot 2SiO_2$

Liquid phase is formed by the melting of eutectic at 1133 °C.

The free energy of Si oxidation, (ΔG) was calculated via FACT (Appendix A). ΔG at 1150 °C is negative (-6.58×10^5 J/mol), so the reaction proceeds.

Mullite formation plus Si oxidation is analysed as follows;

$3Al_2O_3 + 2Si + 2O_2 \rightarrow 3Al_2O_3 \cdot 2SiO_2$

It is assumed the rare earth oxides do not compound with Al_2O_3 and/or SiO_2. CeO_2 is a main phase (48 %) in the MREO and Mechnich et al. (1998) found it precipitates on mullite grain boundaries. Thus, MREO is regarded as a catalyst, i.e. it facilitates reaction without changing composition.

The solution for the reaction is given by the FACT program (Appendix B). The balance number is adjusted to produce 100 % mullite. ΔG is -2.581×10^6 J/mol, i.e.; mullite will form. Thermodynamic analysis thus shows Si-oxidation and mullite-formation will progress at 1150 °C and 1300 °C respectively.

4-3 Liquid Diffusion and Liquid Reaction Studies

4-3-1. The Morphology of the Interface between the Eutectic and Mixtures of Al_2O_3, SiO_2 and Si

Davis and Pask (1972) investigated the high temperature diffusion kinetics of the reaction and phase relations between SiO_2 and Al_2O_3 or SiO_2 and mullite. De Keyser (1965) also studied the reactions between SiO_2 and Al_2O_3 and Al_2O_3 and kaolinite. Staley and Brindley (1969) showed that mullite growth does not occur until the liquid phase is saturated with Al_2O_3, so the role of eutectic is important to mullite growth. The RBM reactions between the eutectic and the mixture of Al_2O_3 and Si (or SiO_2) have not been studied. Reaction kinetics of eutectic will clarify how it facilitates reactions for low temperature synthesis of mullite.

The morphology and kinetics of the reactions between the REO/Al_2O_3/SiO_2 eutectic and Al_2O_3 and Si (or SiO_2) were studied between 1175 °C and 1400°C for 5, 10, 30, 90 minutes. The layered pellets were sectioned and the microstructures in the diffusion zones (or Si) are gathered into Appendix C. Samples are shown in Figs. 4-16 to 4-19. Platinum paste was used as the marker and appears as black particles (1175 °C or 1200 °C) and white particles (1250 °C ~ 1400 °C). It "marks" the original position of the liquid-phase/solid-powder mixture interface. Sample identification is listed in Table 3-3. The bottom layer of each composite pellet is S1, S2, S3 or S4 and the top layer, the eutectic.

Fig. 4-16 (and Fig. C-3 Appendix C) shows the interface morphology for S1, S2, S3 and S4 after 1250 °C for various times. The eutectic layer (top) is porous (dark regions, melted) and has began to diffuse into the bottom layer. The diffusion zone can be clearly seen. The thickness increases with time and is different for each sample, i.e.; 35 μm for S1 after 1250 °C for 90 mins, 50 μm for S2, 30 μm for S3 and S4. The liquid phase in S2 diffuses fastest, ie. the eutectic composition reacts faster with the Al_2O_3/Si mixture of S2. This implies the Si oxidation and reaction of the resultant "SiO_2" increases the "wetting" process and draws the eutectic liquid into the layer.

Fig. 4-17 (and Fig.C-4) shows the interface morphology for S1-S4 after 1300 °C for various times. The diffusion zones are thicker than those of samples sintered at 1250°C. In S2 mullite grains grow in the diffusion layer after 1300 °C for 90 mins. They nucleate at the original interface and grow into the Al_2O_3/Si layer, i.e. the mullite initiates in the liquid and grows into the diffusion layer. This growth mechanism is proved by SEM micrographs of S1 and S2 after 1300 °C for 90 mins (see Fig. 4-20, Section 4-3-2).

Specimens heated at 1175 °C and 1200 °C exhibit no diffusion layer. To calculate Diffusion Coefficients and Activation Energies, at least three reaction-thickness data points are required. Therefore, higher temperatures were explored (1350 °C and 1400 °C). These temperatures were not explored for RBM synthesis as they are beyond the stability temperature of Nextel fibre.

The interface morphology for S1-S4 after 1350 °C for various times are shown in Fig. 4-18 (and Fig. C-5). Pores develop in the "molten" eutectic liquid (top). There are three possible sources thereof:

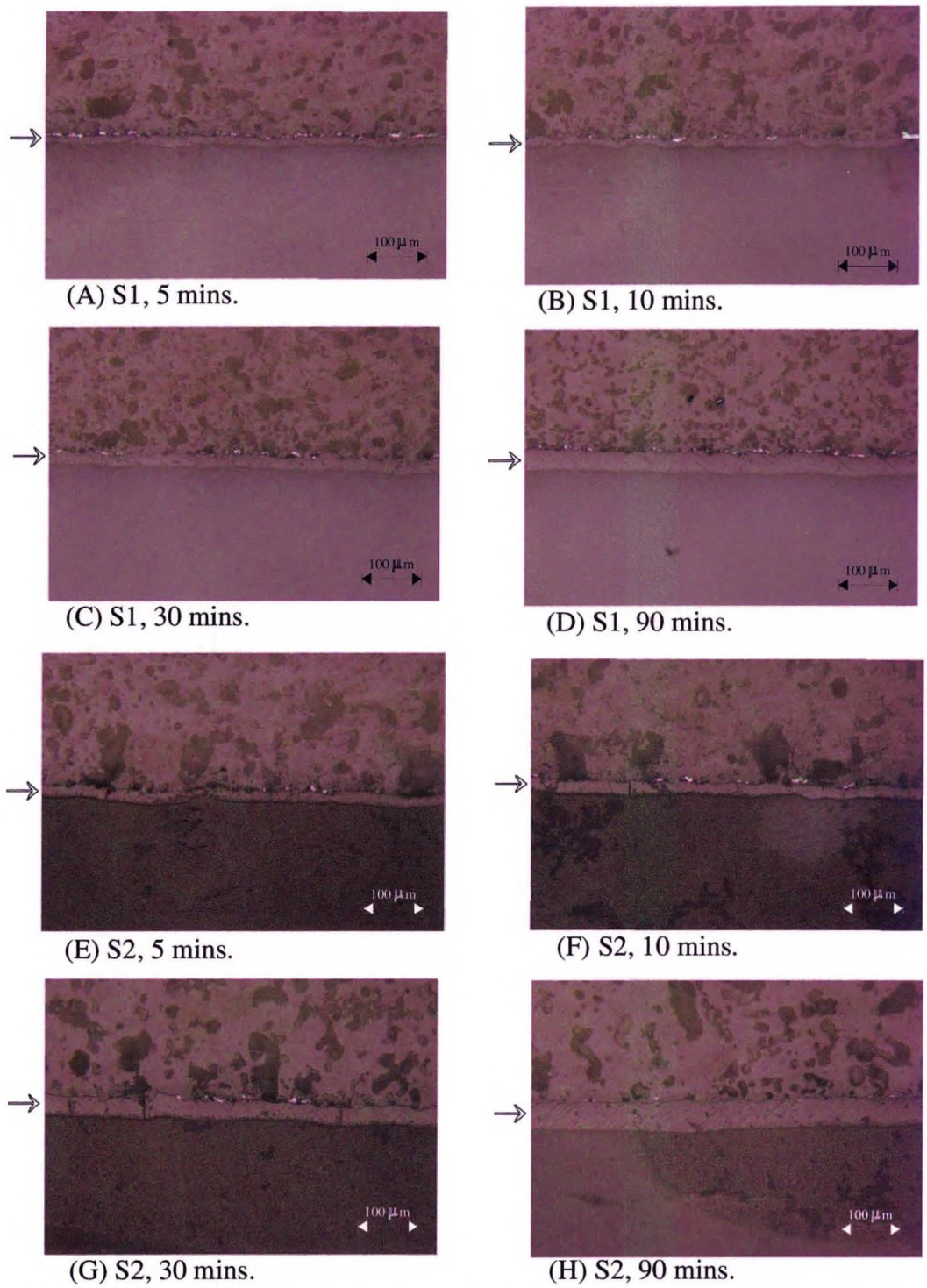

Fig. 4-16.The reaction interface between eutectic composition (top) and Al_2O_3 + SiO_2 (S1) (bottom) or Al_2O_3 + Si (S2) (bottom) after heating at 1250 °C for indicated time (Diffusion layer arrowed).

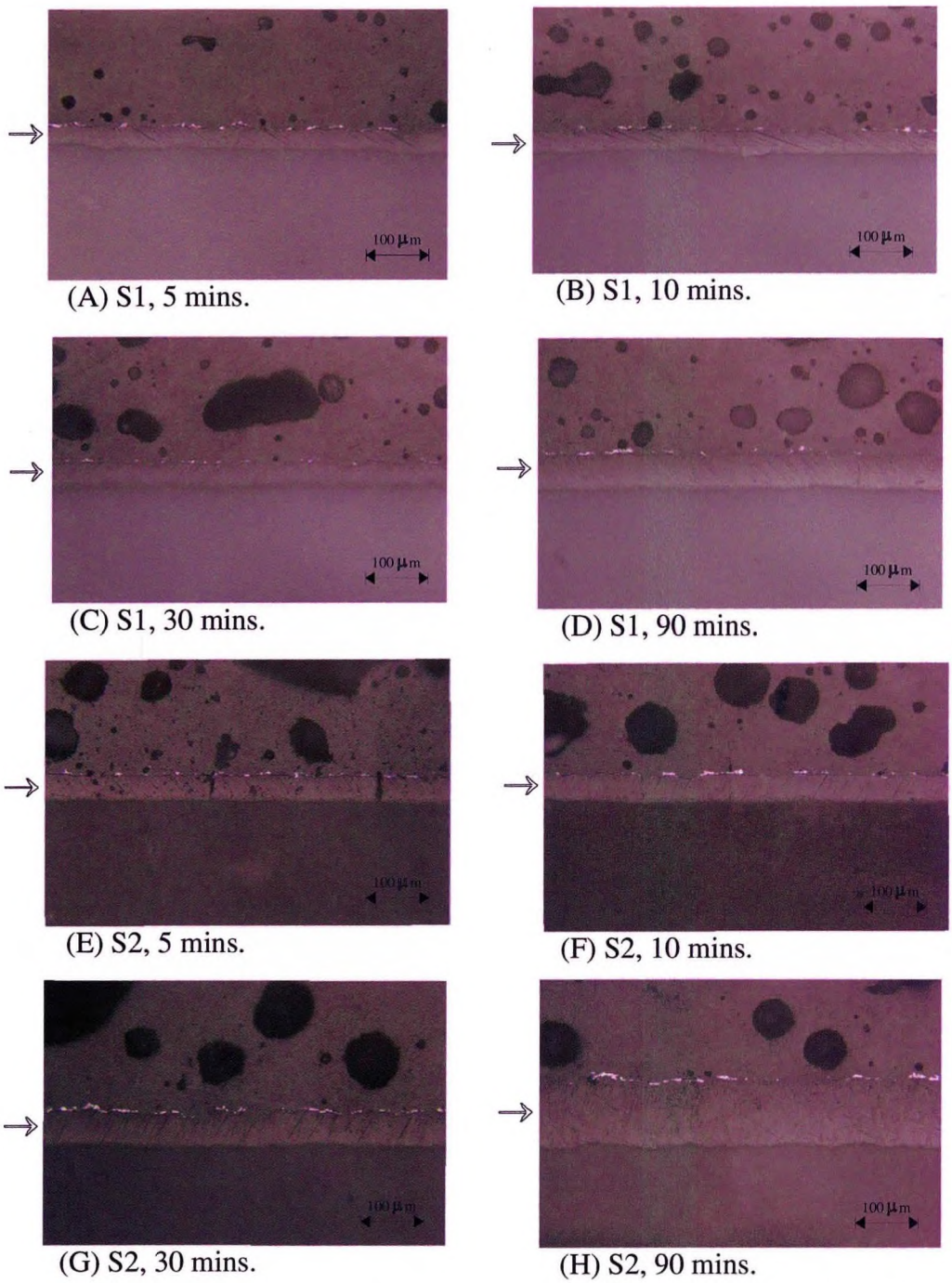

Fig. 4-17. The reaction interface between eutectic composition (top) and $Al_2O_3 + SiO_2$ (S1) (bottom) or Al_2O_3 + Si (S2) (bottom) after heating at 1300 °C for indicated time (Diffusion layer arrowed).

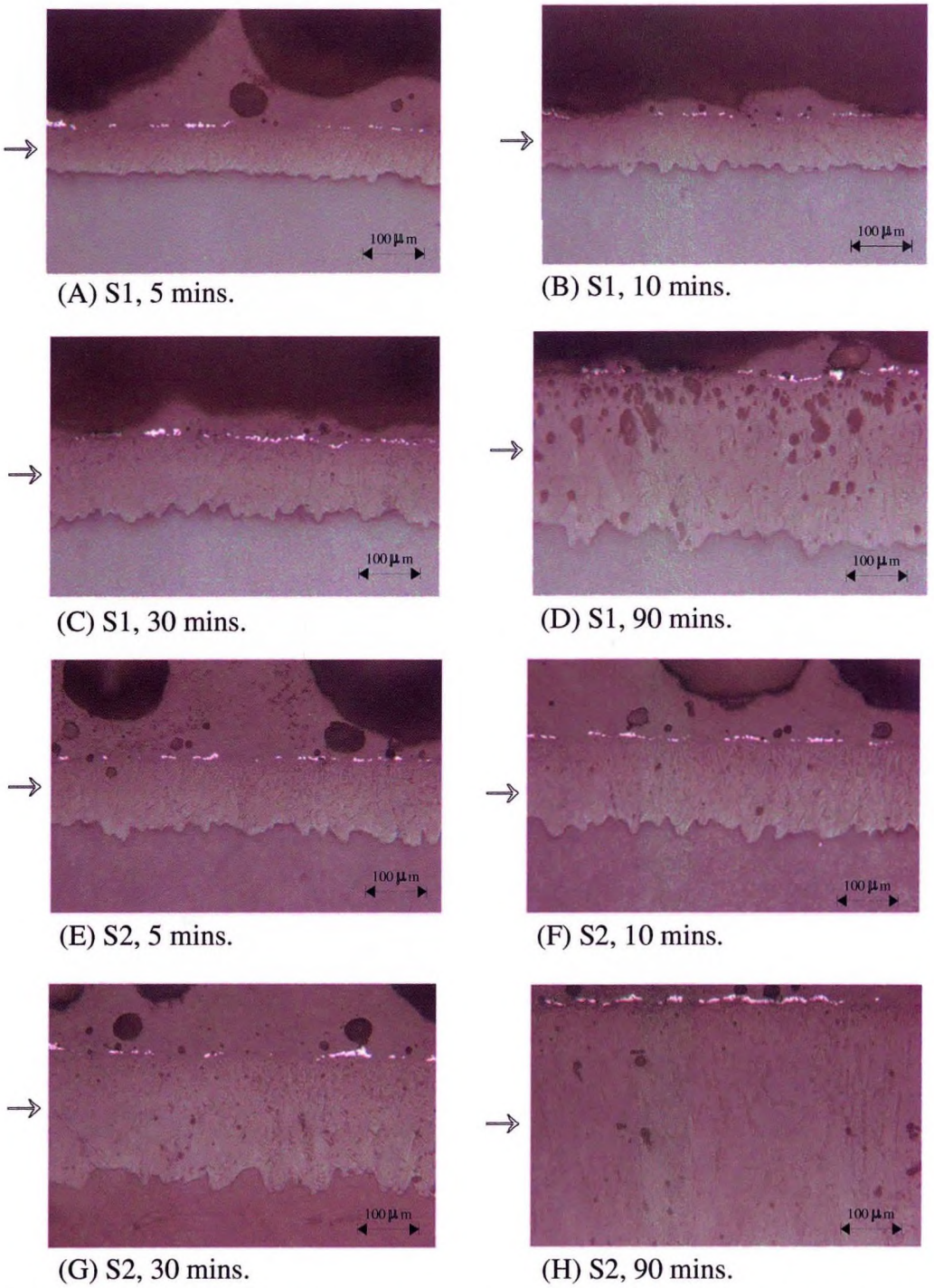

Fig. 4-18.The reaction interface between eutectic composition (top) and Al_2O_3 + SiO_2 (S1) (bottom) or Al_2O_3 + Si (S2) (bottom) after heating at 1350 °C for indicated time (Diffusion layer arrowed).

(a) coalescence of the porosity remnant in the eutectic powder following pressing

(b) exsolution of dissolved gases on cooling

(c) volume "vacated" by the liquid on egress into the Al_2O_3/Si layer.

The latter will occur if the liquid is "drawn" into the Al_2O_3/Si by surface energy and is too viscous to close consequent porosity. Source (a) is also possible if the liquid is viscous. Source (b) is however likely as gases (air) are known to dissolve in silicate liquids and have a positive temperature coefficient. As the pellets were quenched, dissolved gas will exsolve. Also of interest is the "roughness" of the reaction-layer/Al_2O_3 /Si interface. It suggests mullite growth in the diffusion-layer. The reaction layer of S2 is thicker than S1.

Fig. 4-19 (and Fig. C-6) shows the morphology of S1-S4 after 1400 °C for various times. Thick reaction layers occur in the S1 and S2 samples and all are mullite. The S3 and S4 samples do not contain mullite grains though the diffusion layer is thicker. Thus metastable liquid phase is necessary to form mullite (Davis (1972)).

S3 and S4 layers do not show large mullite grains though they contain mullite seeds. The sintering temperature of the seeds is 1550-1600 °C and the mullite formation temperature ≅1400 °C (Yaroshenko et al (2001)). Thus sintering of the oxidation product, (SiO_2) and the associated reduction of reactivity could be why mullite does not develop in the S3 and S4 samples.

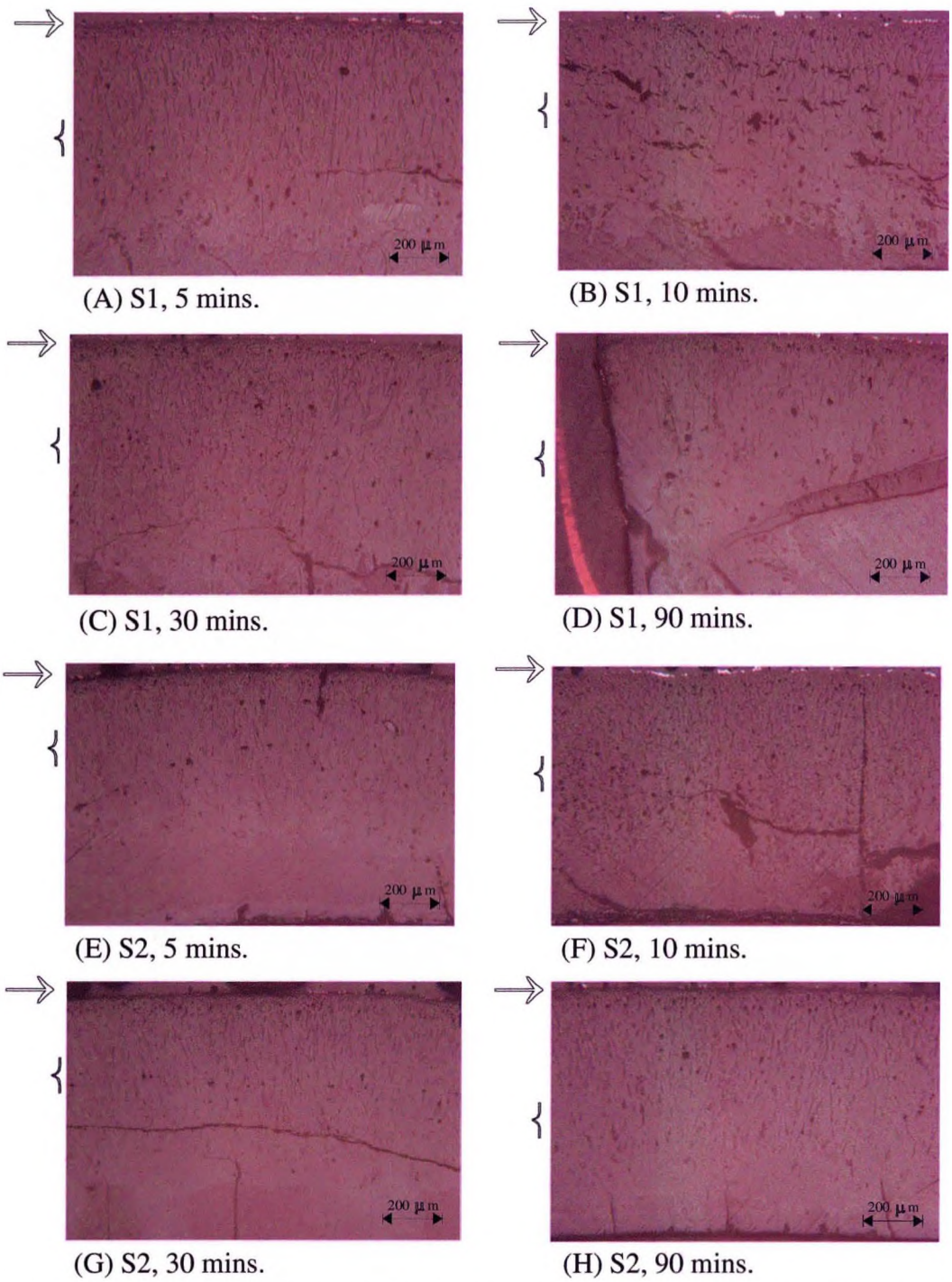

Fig. 4-19.The reaction interlayer between eutectic composition and Al_2O_3 + SiO_2 (S1) or Al_2O_3 + Si (S2) after heating at 1400 °C for indicated time (Pt particles arrowed).

4-3-2. SEM and EDX Line Profile Analyses of the Reaction Layers

SEM photographs and EDX line profiles were taken across the layers to observe mullite and compositional changes in the 1300 °C/90 mins samples. These samples were chosen with a view to Nextel stability. Fig. 4-20 shows SEM photographs of the interlayers in S1-S4. The thicknesses of S1-S4 are ≅ 65 μm, 120 μm, 67 μm and 68 μm, respectively. S2 has the thickest interlayer suggesting the diffusion and reaction-rate of the liquid therein is fastest. Large mullite crystals can be seen in S1 and S2, but S3 and S4 does not contain large mullite. Mullite initiation and growth is observed in the SEM micrographs of S1 and S2.

Fig.4-20 (b), an SEM micrograph of S2, shows the interlayer mullite grains with glassy phase. Mullite has developed more than in S1. The line of the intermediate layer is rough whilst in S1, S3 and S4 the interfaces are flat. This is explained by the faster mullite growth rate inducing a non-planar, rough, interface. The aspect of mullite growth in the diffusion layer implies it has been developed at a intermediate cooling rate. Aksay and Pask (1975) showed microstructures within the diffusion zone at cooling rates indicated in Fig. 2-6.

Mullite initiation and growth in S1 can be seen in the SEM micrograph Fig. 4-20 (a) and two regions can be distinguished, i.e.; that close to the original interface and that close to the Al_2O_3/SiO_2 layer. Mullite is growing in the former, whereas the latter exhibits none. The former has been in contact with the Al_2O_3/SiO_2 for a longer time thus dissolves more and precipitates mullite whereas the liquid had just reached the remnant Al_2O_3/SiO_2

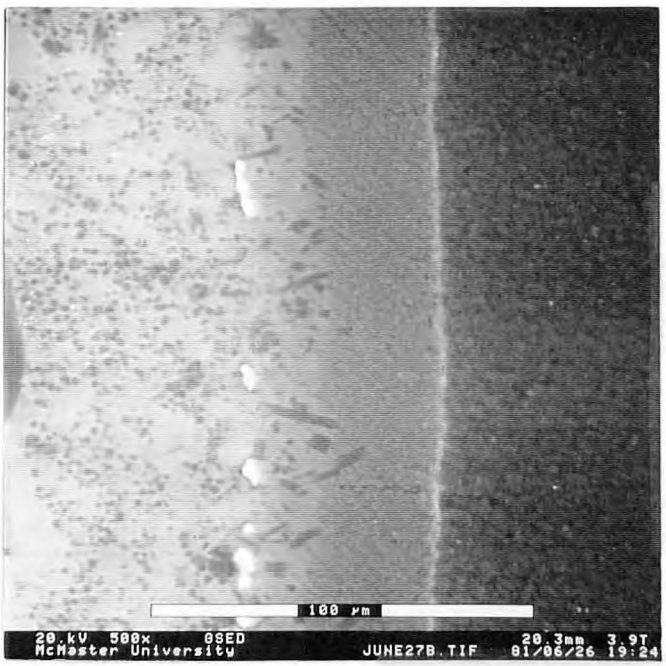

(a)

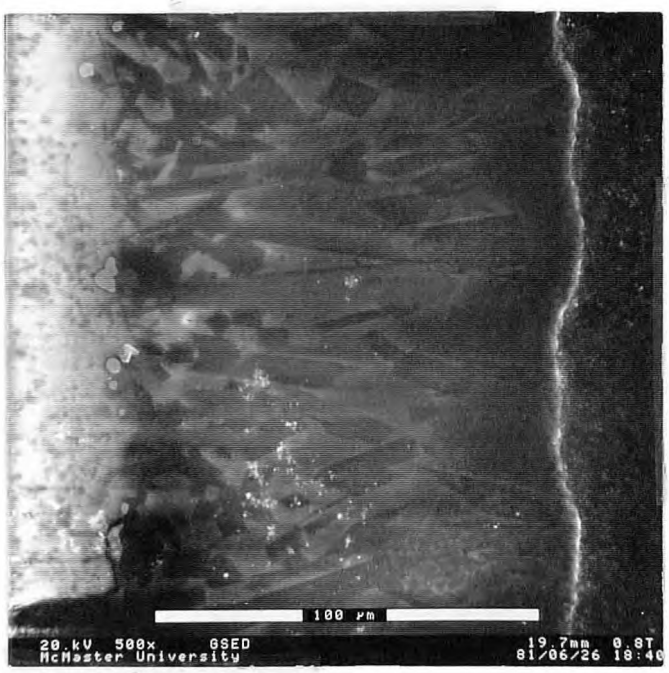

(b)

Fig. 4-20 SEM micrograph of interlayer heat-treated at 1300 °C for 90 mins in (a) S1, (b) S2, (c) S3 and (d) S4


100 µm
20.kV 500x GSED
McMaster University
RBM3.TIF
19.0mm 3.3T
01/07/25 18:51

(c)

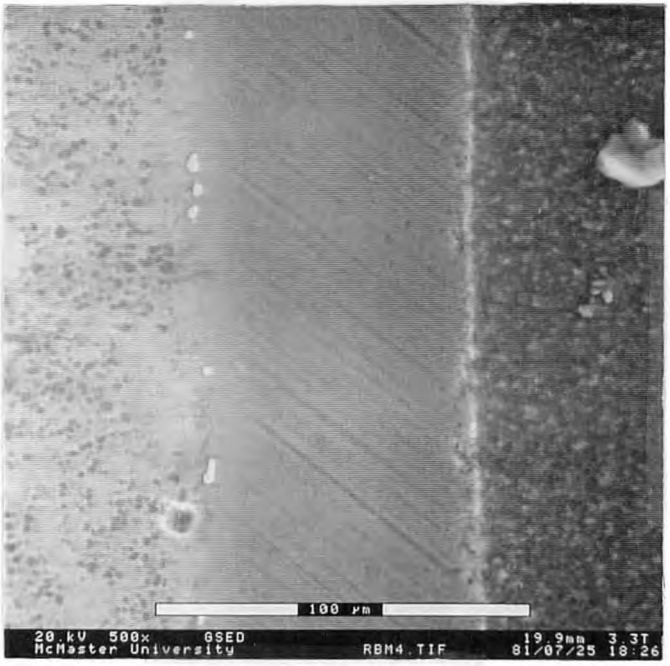
100 µm
20.kV 500x GSED 19.9mm 3.3T
McMaster University RBM4.TIF 81/07/25 18:26

(d)

layer (on the right) when the experiment was terminated. Thus no mullite has yet formed. This two-layer morphology is clearer in sample S2 (Fig 4-20 (b)). No mullite is observed in the interlayer of samples S3 and S4 (Figs. 4-20 (c) and (d)). S3 and S4 contain mullite seeds and less SiO_2 and Si than S1 and S2 (see Table 3-3 Pg. 55). Mullite cannot form with the small amount of SiO_2 and the mullite seeds make these specimens more refractory.

EDX line profile analysis was performed to investigate compositional changes across the reaction layer. The results are shown in Figs. 4-21 (a) - (d). The composition profiles for four elements (Al, Si, Ce, La) are scanned. CeO_2 and La_2O_3 are the main components of the mixed rare earth oxide. All samples exhibit a composition gradient as the eutectic penetrates. The composition thereof is 22 wt% Al_2O_3 /46 wt% SiO_2/32 wt% MREO. The compositions of the other layers are [71.8 wt% Al_2O_3 /28.2 SiO_2] (S1), [89.3 wt% Al_2O_3 /10.7 wt% Si] (S2), [75 wt% Al_2O_3 /19.2 SiO_2 /5.8 wt% mullite seeds] (S3) and [83.5 wt% Al_2O_3 /9.6 wt% Si / 6.5 mullite seeds] (S4). All layers have a larger amount of Al_2O_3 and a smaller amount of Si than the initial eutectic layer. Al increases and Si decreases as one moves from the eutectic into the Al_2O_3 /SiO_2 layer (Fig 4-21 (a)). Ce and La are low but decrease into the Al_2O_3/SiO_2 layer. Fluctuations in the Al and Si level in the eutectic layer are probably associated with the porosity therein. The "white" line observed ahead of the diffusion layer (Figs. 4-21) corresponds to Al and Si minima and is probably due to separation of the liquid-layer and the Al_2O_3/SiO_2 layer by differential contraction on cooling.

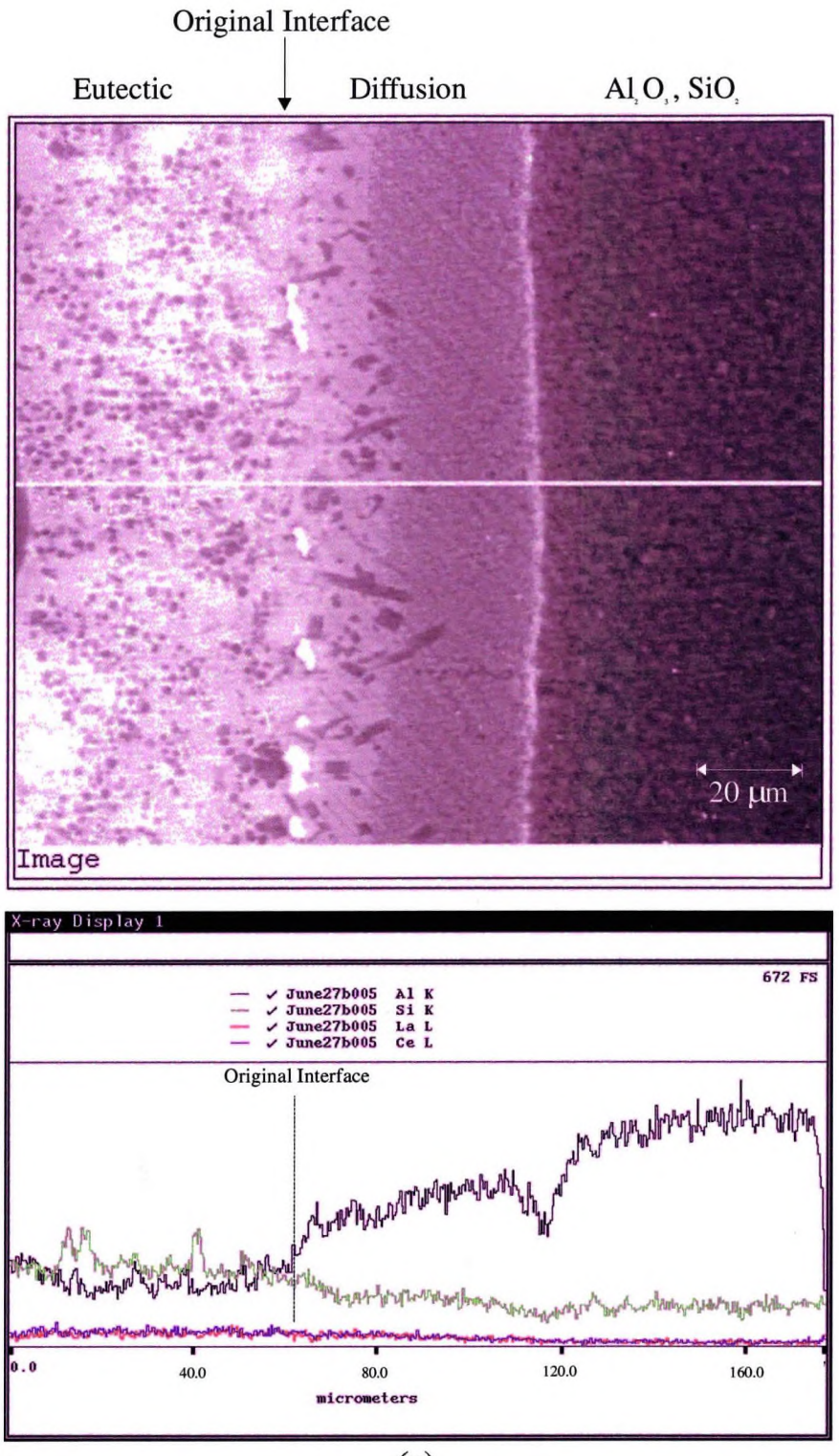

(a)

Fig. 4-21. SEM micrographs and corresponding elemental profiles for Al, Si, La, Ce for the interlayer heat-treated at 1300 °C for 90 mins. in (a) S1, (b) S2, (c) S3 and (d) S4

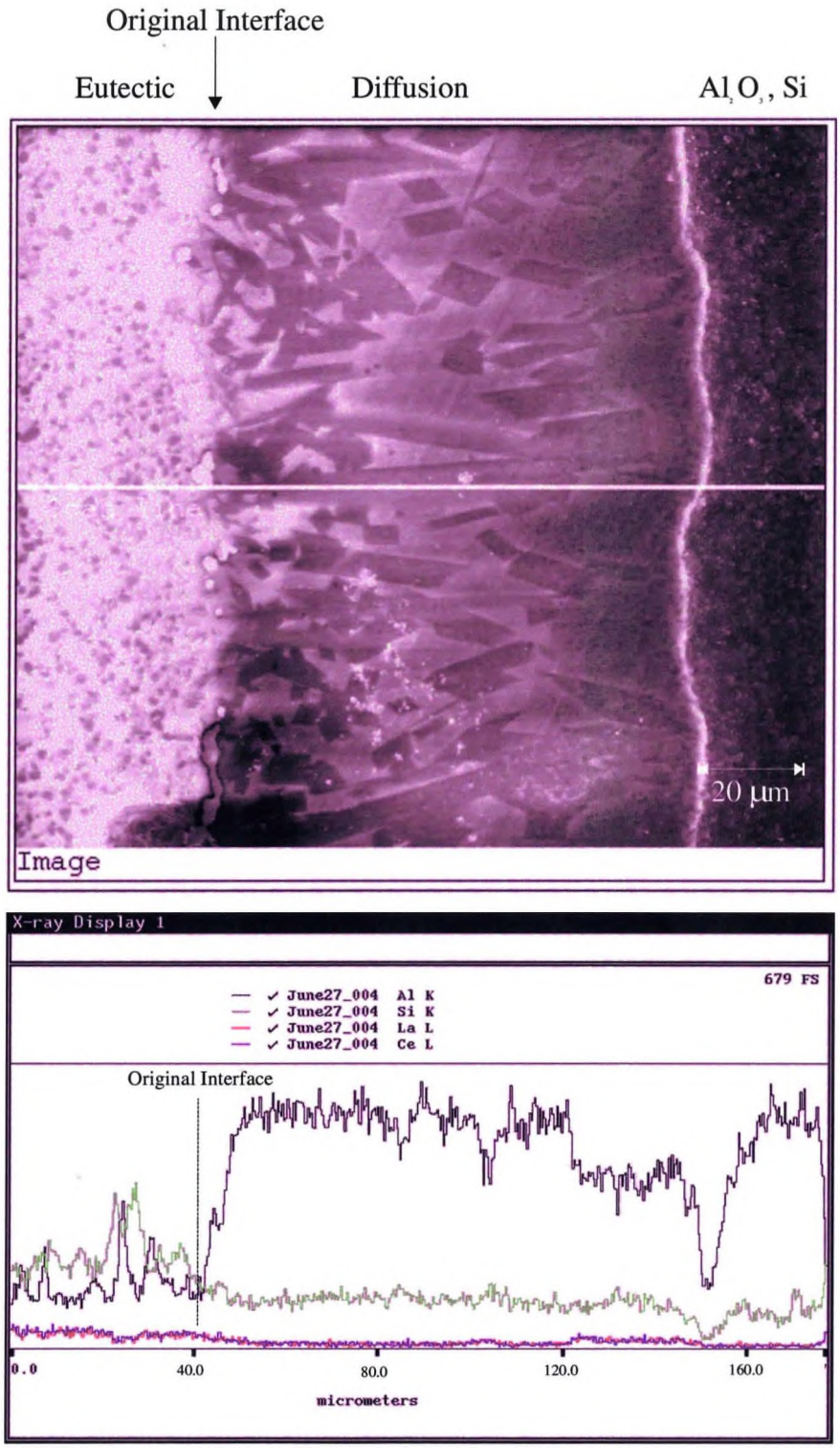
Original Interface
Eutectic
Diffusion
Al_2O_3, Si
20 μm
Image
X-ray Display 1
679 FS
June27_004 Al K
June27_004 Si K
June27_004 La L
June27_004 Ce L
Original Interface
0.0
40.0
80.0
120.0
160.0
micrometers

(b)

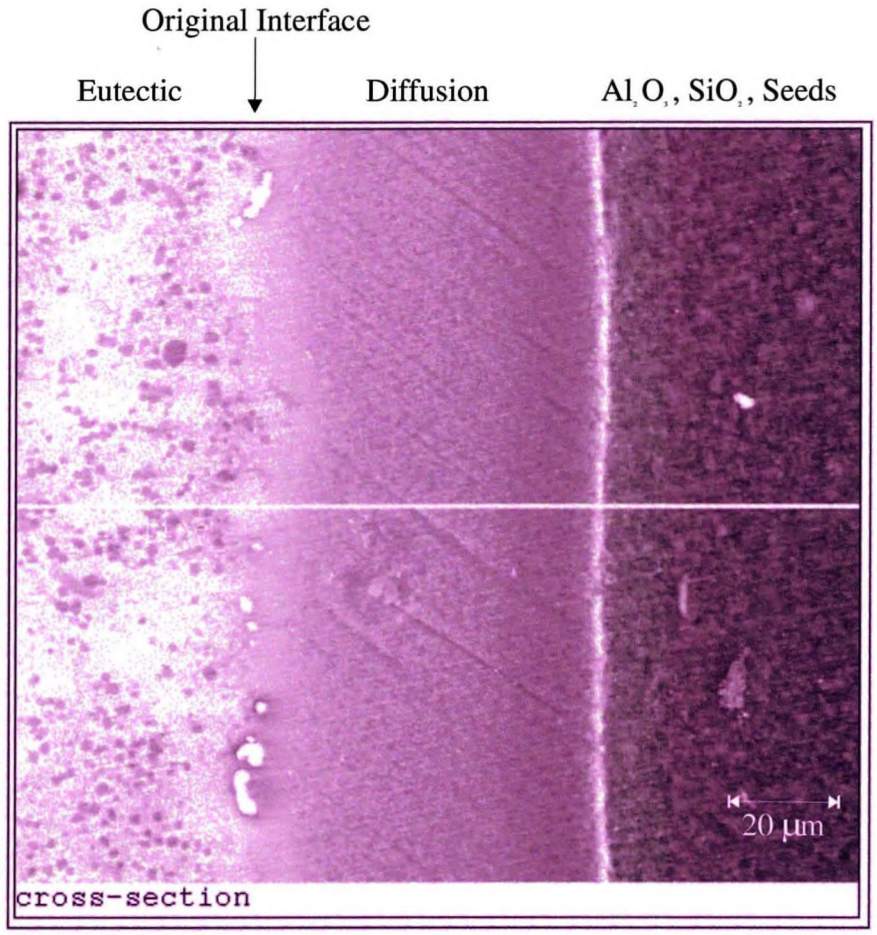
Original Interface
Eutectic
Diffusion
Al_2O_3, SiO_2, Seeds
20 μm
cross-section

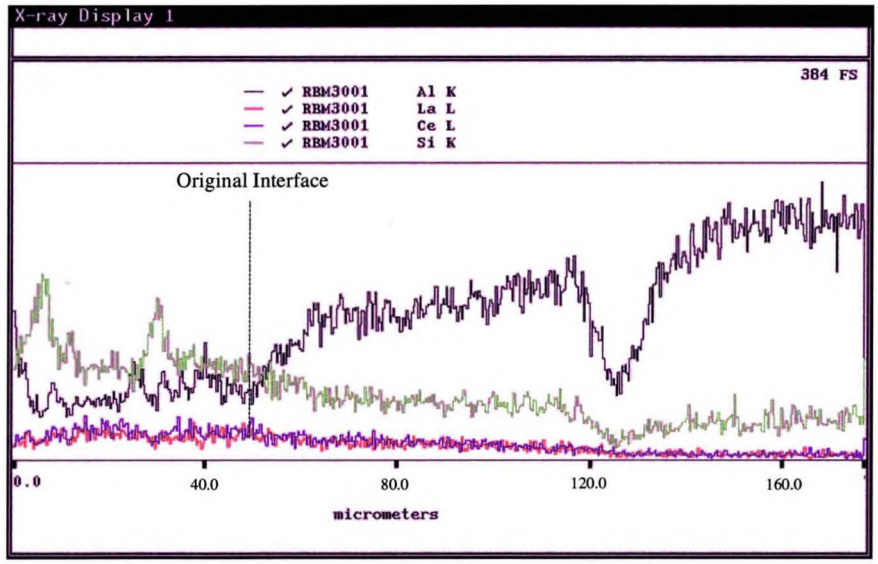
X-ray Display 1
384 FS
RBM3001 Al K
RBM3001 La L
RBM3001 Ce L
RBM3001 Si K
Original Interface
0.0
40.0
80.0
120.0
160.0
micrometers

(c)

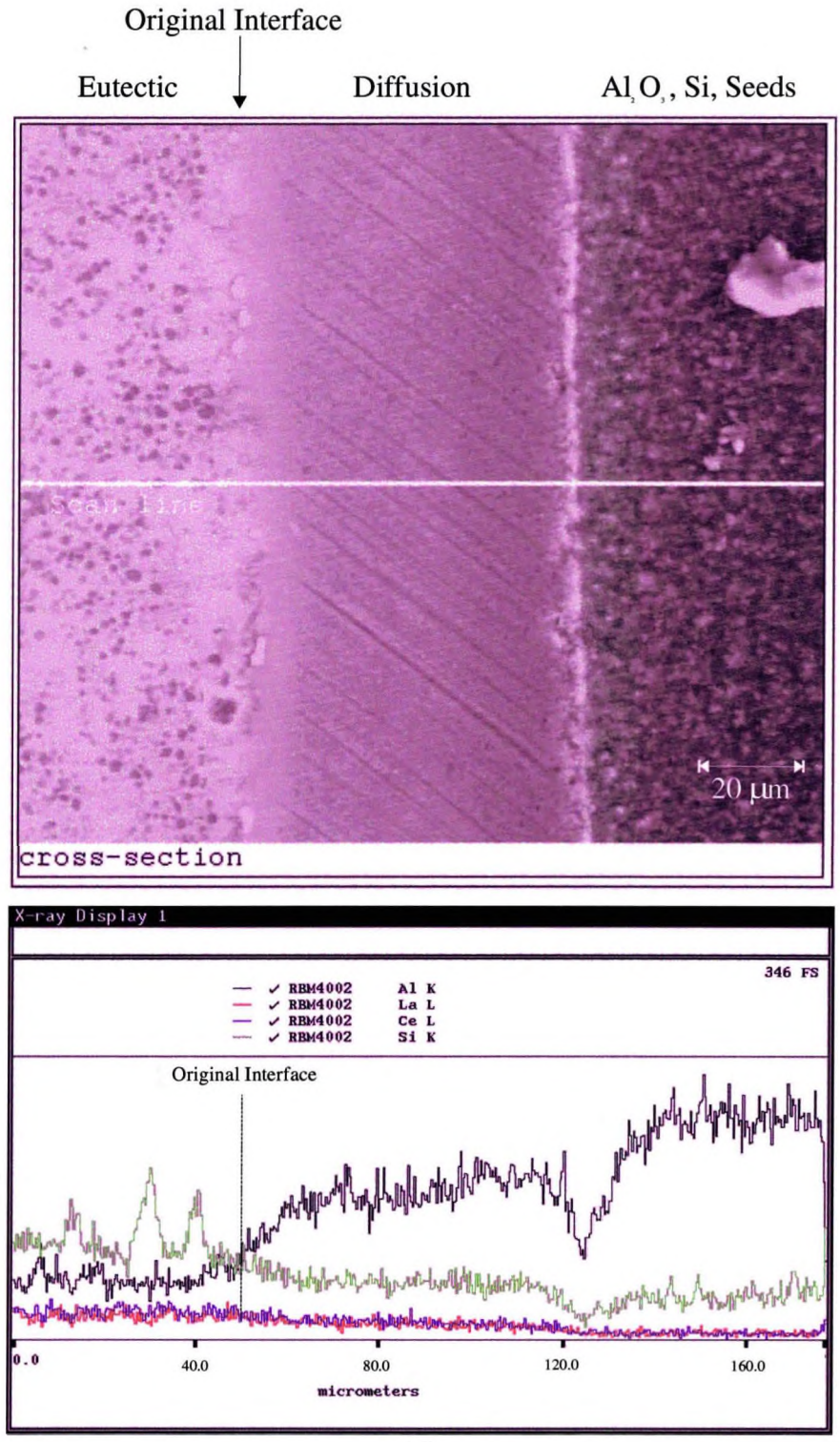
Original Interface
Eutectic
Diffusion
Al2O3, Si, Seeds
Scan Line
20 µm
cross-section
X-ray Display 1
346 FS
RBM4002 Al K
RBM4002 La L
RBM4002 Ce L
RBM4002 Si K
Original Interface
0.0
40.0
80.0
120.0
160.0
micrometers

(d)

4-3-3. The Growth Rate of the Reaction Layer in the Bilayer Laminates

Plots of the square of reaction layer thickness (from Figs. 4-16, 17, 18, 19 and Appendix C) vs. time for S1, S2, S3 and S4 are shown in Figures 4-22 to 4-25. In Fig. 4-22, every sample displays a linear slope suggesting diffusion-control of the reaction at 1250 °C. The diffusion rate in S2 is highest. The order is S2 > S1 > S4 > S3. All samples exhibit no mullite at this temperature (This was also observed in Fig 4-16 and C-3).

Fig. 4-23 shows the square of thickness vs. time plots for S1-S4 at 1300 °C. At this temperature the data for S2 deviates from linearity. Physical diffusion of the liquid into the Al_2O_3/SiO_2 is complicated by mullite formation and the interfacial reaction layer thickens by diffusion and by reaction (mullite formation), so its thickness increases more rapidly than by diffusion alone. It is likely the liquid "wets" the mullite more than the Al_2O_3/Si (SiO_2) therefore, the mullite "draws" the liquid, i.e. enhances its diffusion. This is also suggested by the shape of the reaction layer interface with the Al_2O_3 /Si (SiO_2) (Fig 4-17 and C-4). Mullite starts to show in S2 after 1300 °C for 90 mins. This sample has a rough reaction interface line and a thicker reaction layer. The other samples have a flat interface and similar diffusion layer thickness. Thus mullite formation and growth enhances diffusion and promotes reaction. Samples S1, S3 and S4 at 1300 °C have linear thickness^2 vs. time characteristics thus exhibit diffusion-control.

Plots of the square of thickness vs. time for S1-S4 at 1350 °C are shown in Fig. 4-24. S2 exhibits nonlinearity, S1 initially does so.

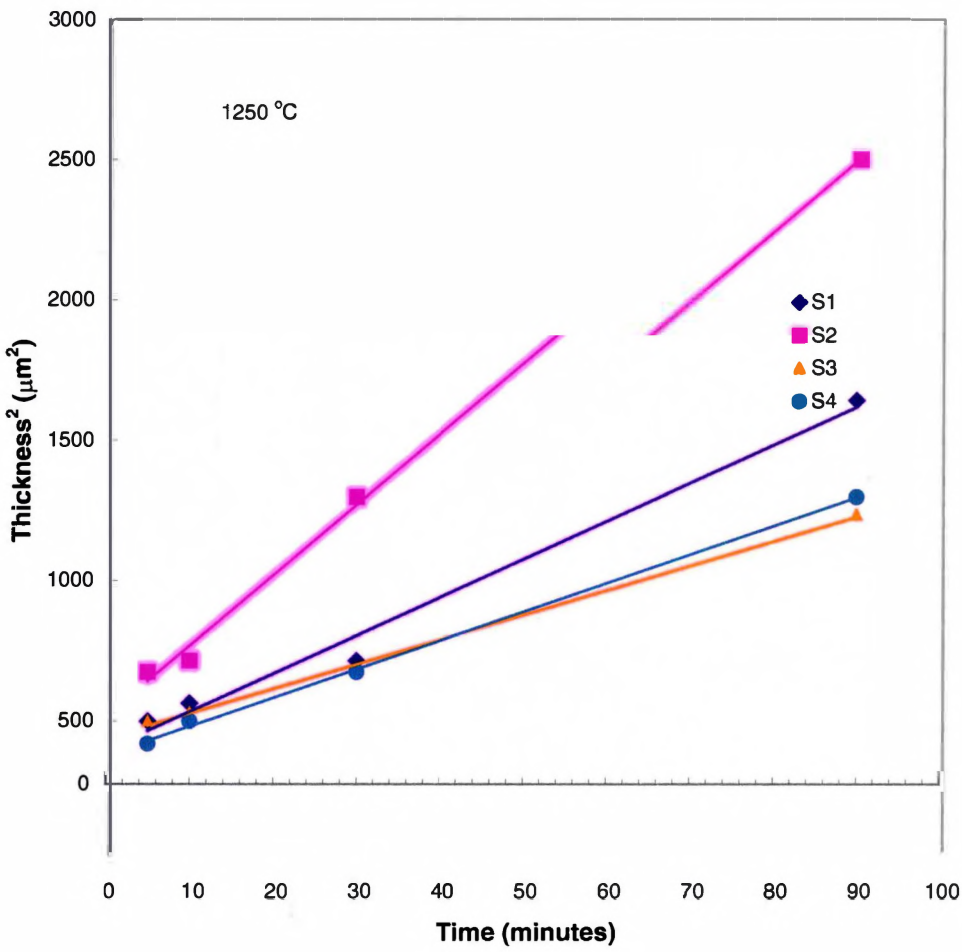

Fig. 4-22. The penetration of liquid phase at 1250 °C into each sample.

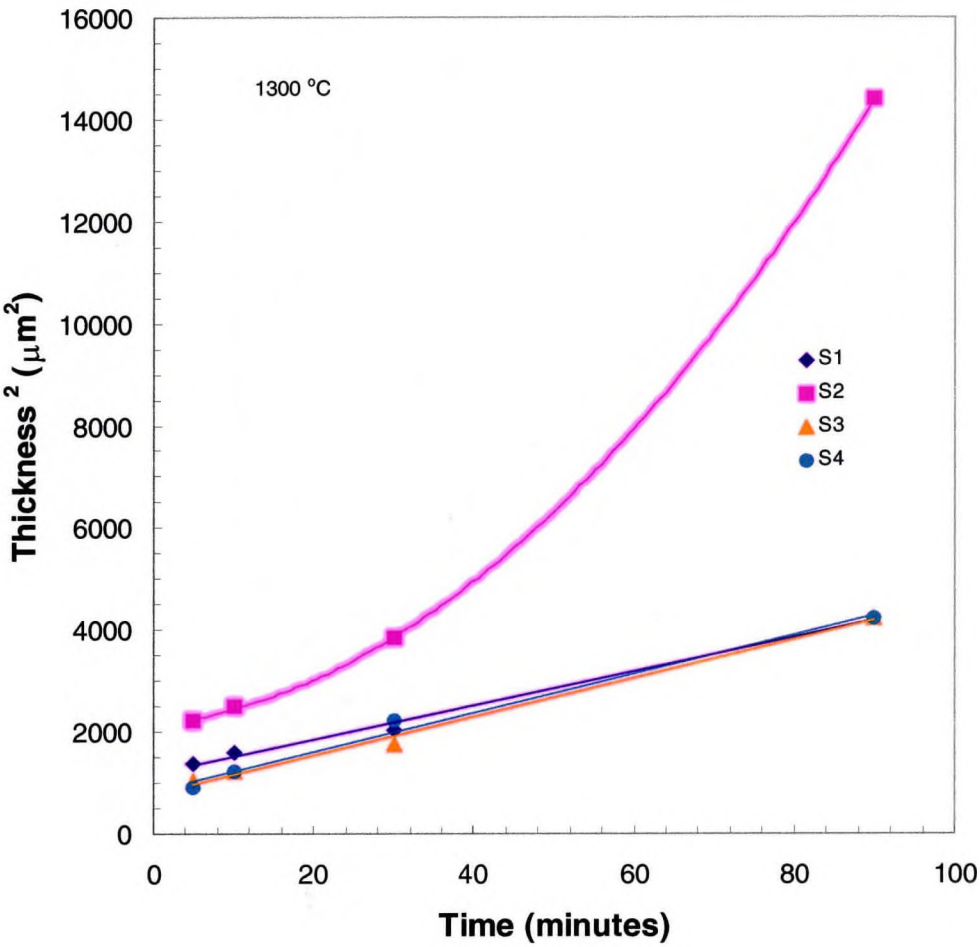

Fig. 4-23. The penetration of liquid phase at 1300 °C into each sample.

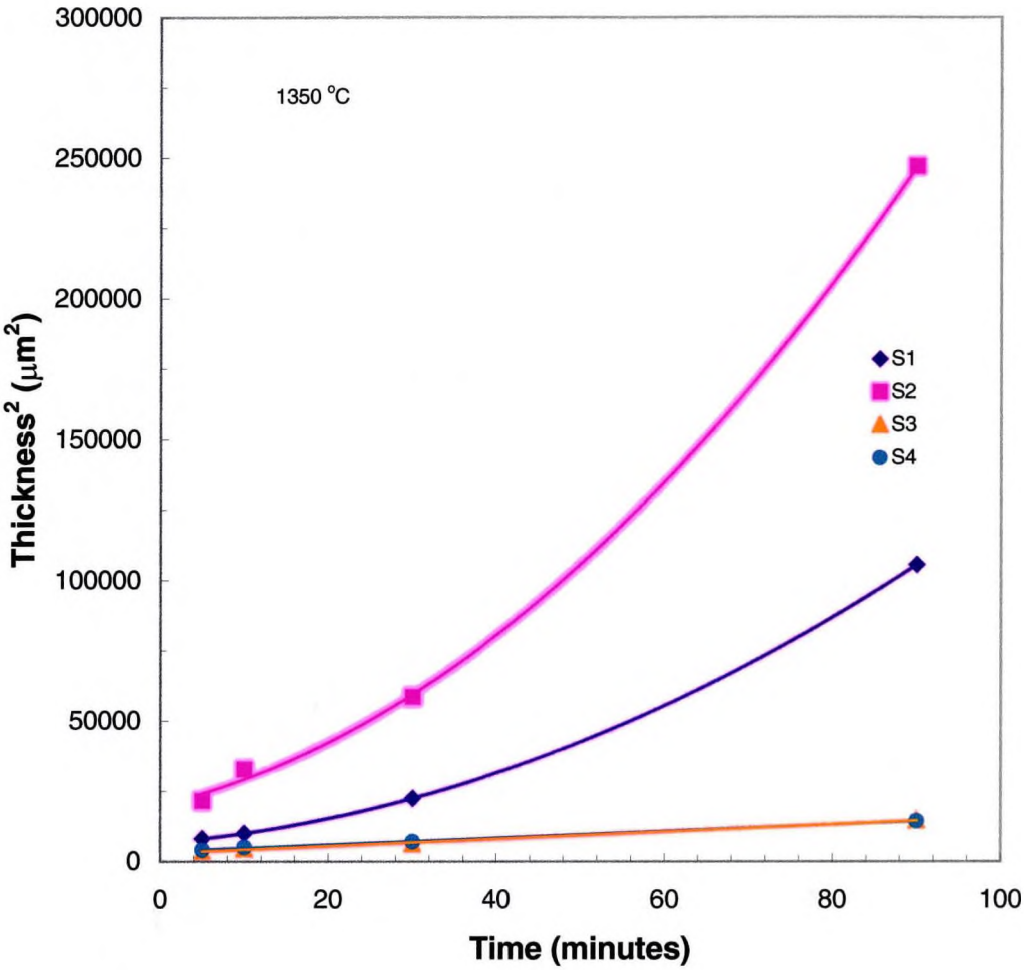

Fig. 4-24. The penetration of liquid phase at 1350 °C into each sample.

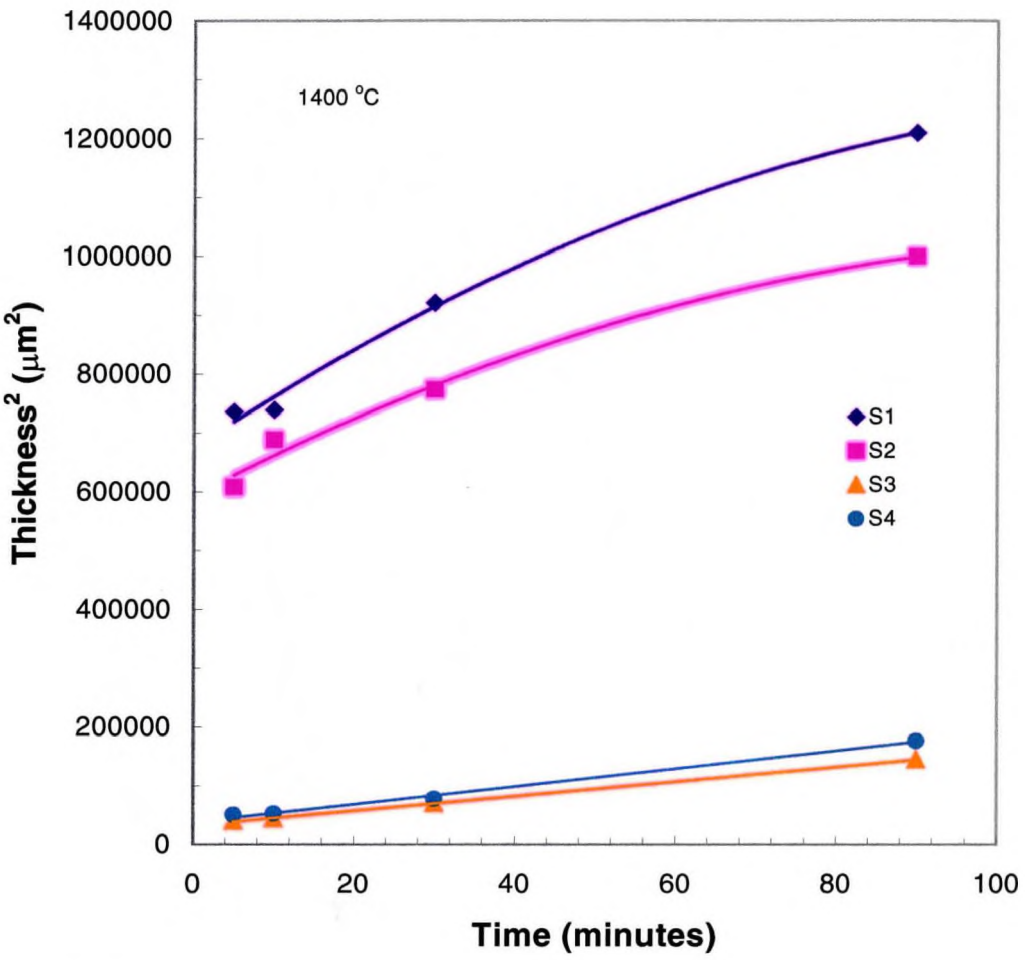

Fig. 4-25. The penetration of liquid phase at 1400 °C into each sample.

Fig. 4-25 shows the square of thickness vs. time plots for S1-S4 at 1400 °C. S3 and S4 exhibit a linear relationship. S1 and S2 display a different relationship compared with the previous temperature (1350 °C) because the liquid has penetrated the specimen thickness.

The diffusion coefficient D for the eutectic liquid can be calculated via;

$$\frac{\sqrt{Dt}}{x} = \text{constant}$$

$$\text{or; } D = \text{constant} \times \frac{x^2}{t}$$

where x = interlayer thickness and t = time.

When plots of thickness^2 vs. time are linear, the slope gives the diffusivity at that temperature. The resultant diffusivity of the liquid phase for S3 and S4 is plotted vs reciprocal temperature in Fig. 4-26. S1 and S2 are not plotted as their thickness^2 vs. time plots > 1300 °C and 1350 °C are non-linear. The values of Diffusion Coefficient 10^{-9} – 10^{-7} cm^2/sec are similar to those obtained by Frischat (1975) for Si diffusion in a slag-glass (4.7×10^{-8} - 1.1×10^{-7} cm^2/sec).

The temperature dependence of the diffusion is;

$$D = D_o \exp\left(-\frac{\Delta E}{RT}\right).$$

where D_o is the temperature-independent preexponential, ΔE is the Activation Energy, T the absolute temperature, R the gas constant.

Taking natural logarithms,

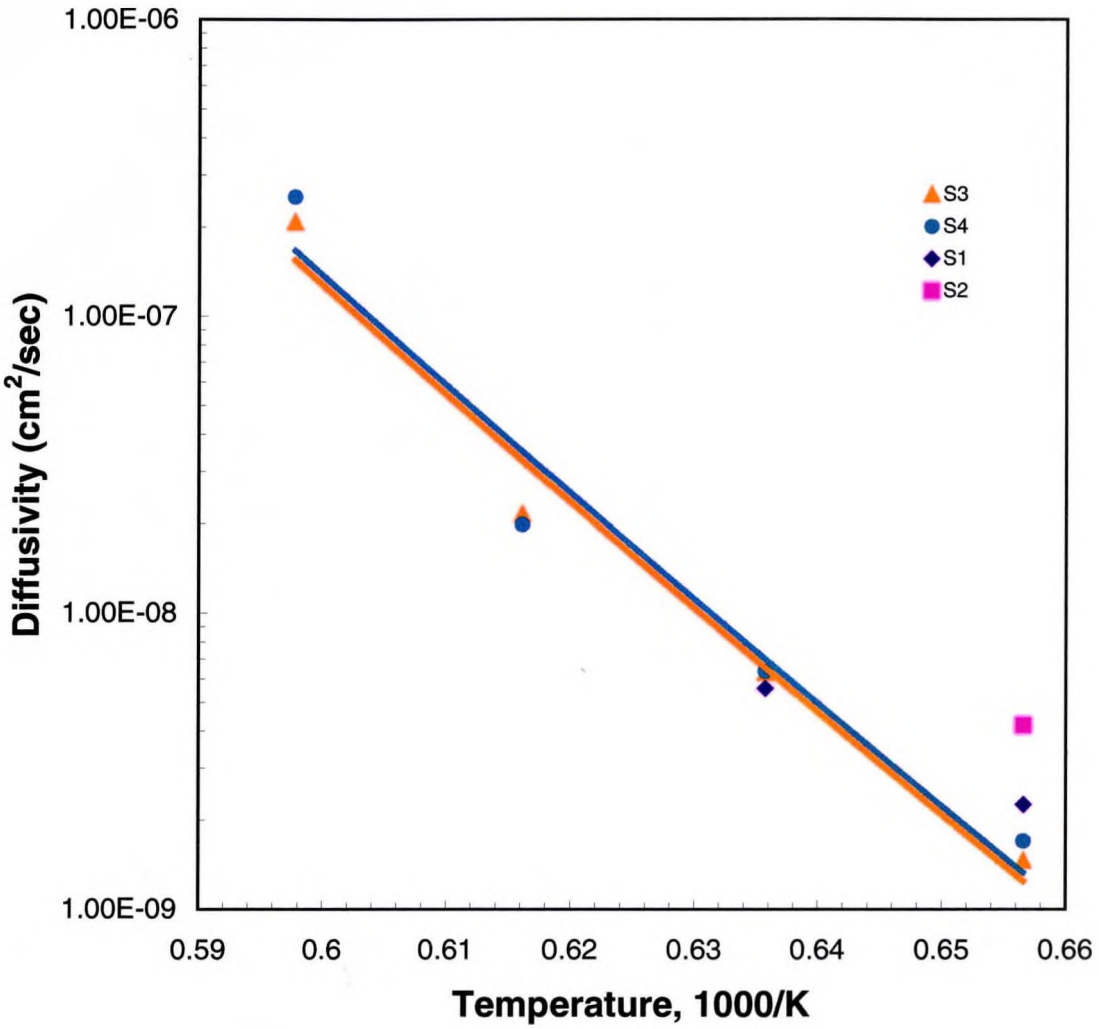

Fig. 4-26. Diffusivity of liquid phase in each sample with temperature.

$$LnD = LnD_0 - \frac{\Delta E}{R}\left(\frac{1}{T}\right).$$

Thus the activation energy can be obtained from the slope of ln D vs. T^{-1} plots. The plots for S3 and S4 have the same slope and give an activation energy for liquid phase diffusion into the Al_2O_3/Si (SiO_2) layer of 579.3 kJ/mol. This diffusion result can be compared with other liquid diffusion values into porous solids. Neretnieks et al. (1987) showed diffusivities of iodide with porosity in porous rock. When porosity is 40 %, D = 7.7×10^{-7} cm^2/sec. This value is compatible with the present results so the result of eutectic layer diffusion is nearly consistent with other liquid state diffusion and is responsible for the fast reaction rate.

4-3-4. Exploration of the Reaction Sequences during the Reaction Bonding of Mullite

The RBM reaction sequence between Al_2O_3, Si, eutectic and mullite seeds will now be established (Fig. 4-27). During the initial heat treatment, Si grains develop amorphous SiO_2 layers. These act as diffusion barriers to further oxygen (see TGA curves, Fig. 4-6 and 4-7) and thus slow oxidation. When the eutectic melts, it dissolves the amorphous SiO_2 layer facilitating continued oxidation and dissolution of the product. The liquid in the system will exert a capillary pressure on the contact points of the Al_2O_3 particles inducing dissolution thereof. This capillary pressure is ($-2\ \gamma/r$) where γ is the liquid/Al_2O_3 surface energy and r the radius of the liquid/air interface. The contact area is

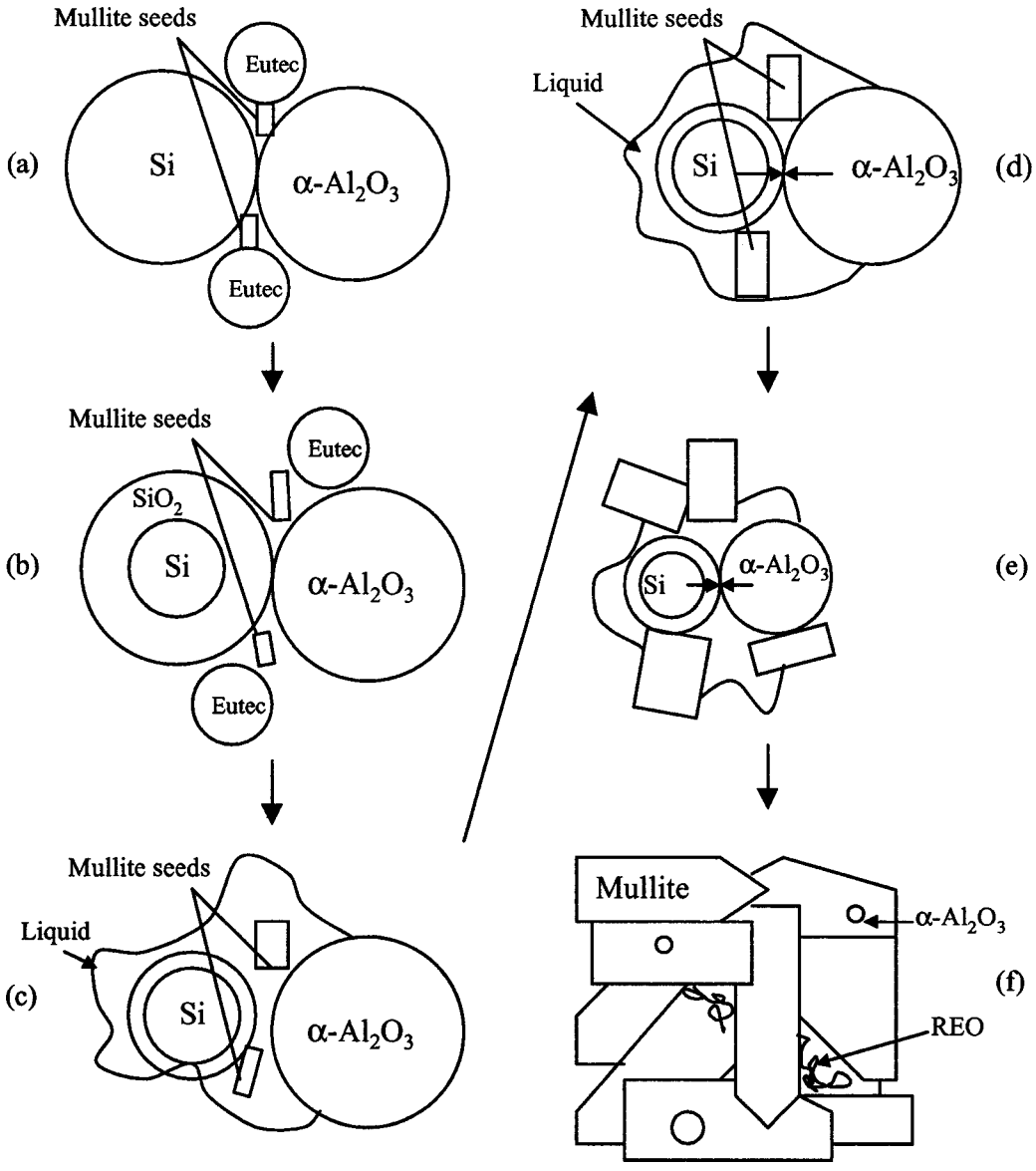

Fig. 4-27. Schematic of the reaction sequence of RBM via Al_2O_3/Si/eutectic composition with mixed rare earth oxide, and mullite seeds.

μm^2, so the stress is ($P/\mu m^2$) where P is the pressure. This pressure can be calculated via particle size of TMDAR Al_2O_3, which is 0.21 μm (2R), and surface energy for a silicate liquid on Al_2O_3, which is ≅ 0.7 J/m^2 (Kingery et al. (1976)). r depends on how much liquid wets two solid particles. The pore (in liquid) radius is fixed by the packing of Al_2O_3. If we assume the Al_2O_3 is spherical and close-packed, the interstitial pore is r = 0.22 R,

$$r = 0.22 \times (0.21\mu m/2) = 0.023\ \mu m$$

$$\text{Stress} = \frac{(2 \times 0.7\ J/m^2)}{0.023\mu m}$$

$$= 61\ \text{MPa compression}$$

Extra Al_2O_3 will dissolve in the liquid due to this stress. Thus, at the contact point, the liquid becomes supersaturated with Al_2O_3. Away from the contact point the Al_2O_3 level in the liquid is the equilibrium value, i.e. an Al_2O_3 concentration gradient develops between the particle contacts and the liquid away therefrom. Al_2O_3 will diffuse down this gradient and precipitate in a stress free region due to the supersaturation thereat. As it exsolves it will react with the "SiO_2" and "grow," mullite on the mullite seeds. The latter act as a catalyst for mullite formation.

4-4. Definition of the Roles of the Eutectic and the Mullite Seeds in the RBM Process

4-4-1. Definition of the MREO Eutectic Role in the RBM Protocol

A series of experiments were undertaken on sandwich pellets, i.e. two layers divided by platinum foil. The top layer was Al_2O_3/Si and the bottom layer, Al_2O_3/Si/eutectic powder. The geometry was designed to identify the influence of the eutectic on Si oxidation, mullite formation, and pellet densification. After sintering at 1300 °C for 5 hrs, X-ray diffraction was conducted on the top and bottom layers (Fig. 4-28).

The top layer was found to be Al_2O_3 and Si with a trace of SiO_2. No mullite was detected. The X-ray diffraction pattern of the bottom layer (Al_2O_3, Si, and eutectic) shows major mullite with minor Al_2O_3 and REO (CeO_2) phases. No Si or SiO_2 were detected. Thus the eutectic liquid promotes oxidation of the Si particles to SiO_2 and promotes mullite formation. The density of the top layer was 89.1 %TD, the bottom one, 93.0 %TD. As expected, the density improved with presence of eutectic liquid.

4-4-2. Definition of the Role of Mullite Seeds in the RBM Protocol

Again sandwich pellets with 2 layers divided by Pt foil were explored, i.e. (Al_2O_3 + Si)/ (Pt)/(Al_2O_3 + Si + 5 w/o mullite seeds). These pellets were heat-treated at 1300 °C for 5 hours.

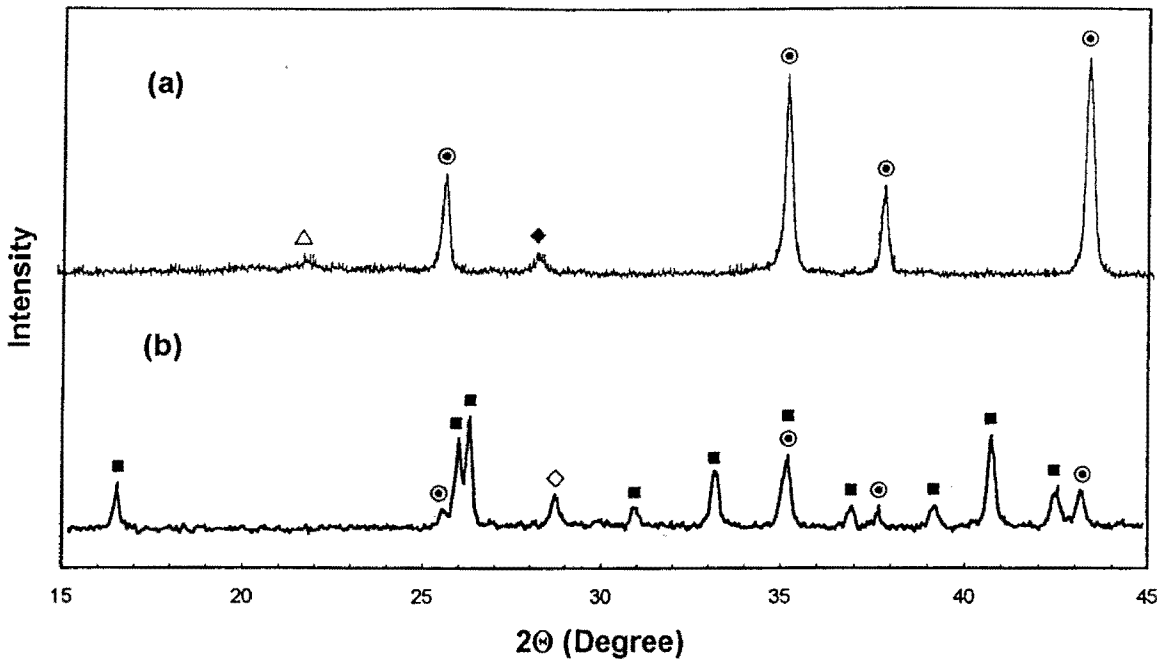

Fig. 4-28. X-ray diffraction patterns (a) Al_2O_3 + Si and (b) Al_2O_3 + Si +eutectic layers after heating at 1300°C for 5 hrs (■: Mullite, ◉: α-Al_2O_3, △: Cristobalite, ◆: Si, ◇: REO).

The XRD of the top layer detected SiO_2 (Fig. 4-29 (a)), whereas the bottom layer exhibited SiO_2 and Al_2O_3 with mullite. The mullite peaks are small (Fig.4-29 (b)). To check their source, the top layer was ground, mixed with the same level of mullite seeds, then XRD taken to check whether the mullite detected is the original seeds. The result is shown in Fig 4-29 (c), and there are no mullite peaks. This suggests the mullite seeds in the bottom layer promoted some mullite formation. The density of the top layer was 89.1 %TD, the bottom layer 86.2 %TD. The density of the bottom layer is lower as the mullite (seeds) have a lower density (3.15 g/cc) than the Al_2O_3 (3.97 g/cc) and also render the mixture more refractory.

4-3-3. The Combined Role of the Eutectic and the Mullite Seeds in the RBM Protocol

A third pellet was explored wherein the 2 layers were (Al_2O_3 + Si + 5 w/o mullite seeds) and (Al_2O_3 + Si + eutectic + 5 w/o mullite seeds). Again the layers were divided by Pt foil. The X-ray diffraction pattern of the top layer shows Al_2O_3, SiO_2, and minor mullite (Fig 4-28) (as per Figure 4-34 (b)). The bottom layer exhibits major mullite with minor Al_2O_3 and REO (CeO_2) illustrating that the eutectic plays the major role in the Si oxidation and mullite formation (between the Al_2O_3 and SiO_2). The top layer density was 86.2 %TD, the bottom layer 91.0 %TD, i.e.; the liquid phase also promotes densification.

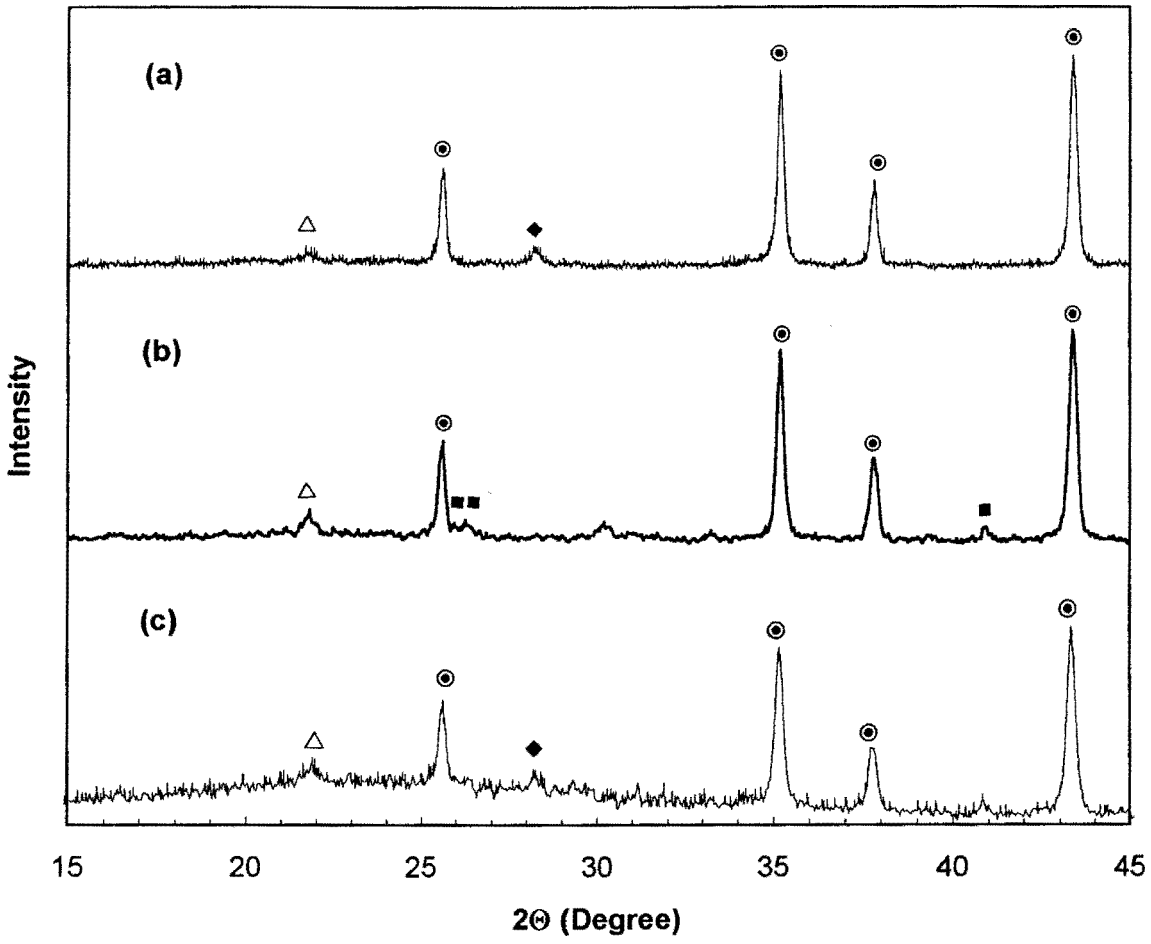

Fig. 4-29. X-ray diffraction patterns (a) Al_2O_3 + Si, (b) Al_2O_3 + Si + mullite seeds after heating at 1300°C for 5 hrs and (c) Ground (a) + mullite seeds (■: Mullite, ⊙: α-Al_2O_3, △: Cristobalite, ◆: Si).

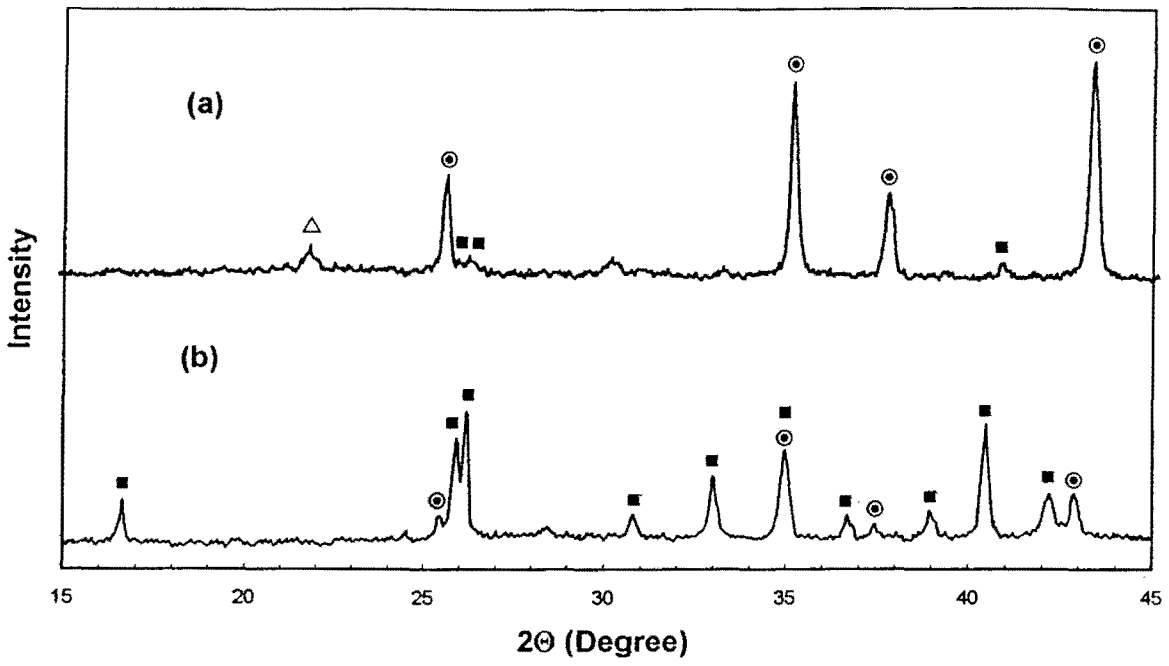

Fig. 4-30. X-ray diffraction patterns (a) Al_2O_3 + Si + mullite seeds and (b) Al_2O_3 + Si + eutectic + mullite seeds layers after heating at 1300°C for 5 hrs (■: Mullite, ◉: α-Al_2O_3, △: Cristobalite).

CHAPTER 5

Conclusions

Dense, high mullite content, reaction-bonded-mullite ceramics have been synthesized at less than 1300 °C using mullite seeds and a eutectic liquid of Al_2O_3, SiO_2 and mixed rare earth oxide. The new feature of this project is the eutectic composition involving mixed rare earth oxide.

Liquid phase present during the synthesis of RBM influences reactions therein. The processing temperature for fibre-reinforced, mullite-matrix composites must be lower than 1300 °C because of fibre degradation (Nextel 720). Thus low liquid formation temperature is required. The eutectic point of Al_2O_3/SiO_2/MREO is 1175 °C. Pure rare earth oxide based eutectic composition have higher eutectic points; 1224 °C for Pr_6O_{11}/ Al_2O_3/SiO_2, and 1259 °C for $Eu_2O_3/Al_2O_3/SiO_2$.

The density of RBM increased with MREO and decreased with mullite seeds. Final densities of RBM were from 78.6 %TD to 92.6 %TD and with a shrinkage range from +0.88 ~ -3.76 %. All RBM specimens had low shrinkage, i.e.; the sintering shrinkage was compensated by Si-oxidation expansion. Thus an effective process has been developed to solve the sintering shrinkage problem faced by mullite-fiber-reinforced/mullite-matrix composites. When the RBM include 7.5 wt% MREO, 5 wt% mullite seeds and the

balance Al_2O_3 and Si, > 90 % theoretical density was achieved with > 90 % mullite and 2.2 % of shrinkage.

Silicon oxidation is almost complete after 1300 °C for 5 hrs, but the final weight gain is different from theoretical because of pre-oxidation of the Si.

The rates of oxidation and mullitisation depend on the amount of liquid phase present and a critical value should not be exceeded.

The level of α-Al_2O_3 and SiO_2 decreases and mullite increases with temperature at 1250-1290 °C but all samples sintered at 1300 °C for 5 hrs had intense mullite peaks with minor residual α-Al_2O_3. A possible reason for the latter is alumina milling residue and pre-oxidized Si in the starting powder. RBM 2 develops 90 % mullite with 10 % α-Al_2O_3.

Transmission electron microscopy showed mullite grains grow and other phases decrease as the reactions proceed. RBM2 sintered at 1300 °C for 5 hrs has small Al_2O_3 particles between and embedded in, the mullite grains during grain growth.

The eutectic phase was found to diffuse into the Al_2O_3/Si layer, forming an intermediate reaction layer. The latter thickness increases with temperature and time. When the liquid phase diffuses into the Al_2O_3/Si layer, the reaction layer thickens faster than when it diffuses into other layers investigated (Al_2O_3 + SiO_2, Al_2O_3 + SiO_2 + mullite seeds, Al_2O_3 + Si + mullite seeds). At low temperatures, the reaction layer thickness is diffusion controlled, but deviates from diffusion control when mullite starts to form. However, the (Al_2O_3 +SiO_2 + mullite seeds) and (Al_2O_3 + Si +mullite seeds) layers display linear thickness^2 vs. time curves i.e.; they follow diffusion-controlled reaction

kinetics up to 1400 °C. The activation energy for diffusion of the liquid was 579.3 kJ/mol.

The reaction mechanism within RBM was determined via a series of model experiments. After Si oxidation, the MREO/Al_2O_3/SiO_2 eutectic melts, dissolves the amorphous SiO_2 diffusion barrier on the remaining Si, and exerts a capillary pressure on the contact points of the Al_2O_3 particles. Liquid at the latter supersaturates with Al_2O_3, and a concentration gradient of Al_2O_3 develops in the liquid. The Al_2O_3 diffuses down this concentration gradient to precipitate on mullite seeds in stress-free regions, i.e.; mullite formation and growth is catalysed.

Layers with and without eutectic and/or mullite seeds confirm the role of eutectic and mullite seeds in the RBM protocol. In pellets of (Al_2O_3 +Si) and (Al_2O_3 + Si + eutectic), the latter shows major mullite and minor α-Al_2O_3, whilst the former exhibits α-Al_2O_3, Si and SiO_2 phases. Si is not oxidized in the former. The density of the layer with eutectic (93.0 %TD) is higher than any other layer. Thus it can be concluded the eutectic liquid promotes Si oxidation, mullite formation and densification.

The layer sample that included both eutectic and mullite seeds exhibits mullite and minor α-Al_2O_3, whilst the sample with seeds alone was still α-Al_2O_3, Si and SiO_2. The density of the former (91.0 %TD) is higher than the latter (86.2 %TD). Therefore, it can be concluded the transient liquid eutectic plays a major role in Si oxidation, mullite formation (between Al_2O_3 and SiO_2) and densification.

REFERENCES

Aksay, I. A. and Pask, J. A., "Stable and Metastable Equilibria in the System SiO_2-Al_2O_3," J. Am. Ceram. Soc., 58, 507-512 (1975).

Aksay, I. A. and Pask, J. A., "The Silica-Alumina System: Stable and Metastable Equilibria at 1.01.0 Atmosphere," Science, 183, 69 (1974).

Aksay, I. A., Dabbs, D. M. and Sarikaya, M., "Mullite for Structural, Electronic, and Optical Application," Am. Ceram. Soc., 74 [10] 2342-2358(1991).

Albano-Muller, L., Thummler, F. and Zapf, G., "High-Strength Sintered Iron-Base Allows by using Transition Metal Carbides," Powder Met., 16, 236-256 (1973).

Aramaki, S. and Roy, R., "The mullite-Corundum Boundary in the System MgO-Al_2O_3-SiO_2," J. Am. Ceram. Soc., 42, 644-645 (1959).

Atalla, M. M., "Properties of Elemental and Compound Semiconductors," edited by Gatos, H., Interscience Publishers, Inc., New York, Vol.5, 163-181 (1960).

Baek, W. H., "Development of Transient Liquid Phase Sintering of Iron-Titanium," Ph.D Thesis, Rensselaer Polytechnic Institute, Troy, NY (1985).

Banerjee, S., Genenetzis, V. and Thummler, F., "Liquid Phase Formation During Sintering of Low-Alloy Steels with Carbide-Base master Alloy Additions," Powder Met., 23, 126-129 (1980).

Berry, D. F., "Factors Affecting the Growth of 90/10 Copper/Tin Mixes Based on Atomized Powders," Powder met., 5, 247-266 (1972).

Boch, P. and Giry, F. P., "Preparation and Properties of Reaction-Sintered Mullite-ZrO_2 Ceramics," Mater. Sci. Eng., 71, 39-48 (1985).

Boch, P. and Giry, F. P., "Zirconia-Toughened Mullite Ceramics-The Role of Zircon Disassociation," Ceramic Transactions, Vol. 6, Mullite and Mullite Matrix Composites., Edited by Somiya, S., Davis, R. F. and Pask, J. A., Am. Ceram. Soc. Westerville, OH, 473-494 (1990).

Boch, P., Giry, F. P. and Rodrigo, P. D. D., "Reaction Sintering of Mullite-Based Ceramics," in Advances in Ceramics, Vol. 24, Science and Technology of Zirconia III, Edited by Somiya, S., Yamamoto, N. and Yanagida, H., Am. Ceram. Soc., Westerville, OH, 1107-11119 (1988).

Bondar,I. A. and Galakhov, F. Ya. , " Phase Equilibria in the System Y_2O_3-Al_2O_3-SiO_2," Izv. Akad. Nauk SSSR, Ser. Khim., 7, 1325-1326(1964).

Bowen, N. L. and Greig, j. W., "The system Al_2O_3-SiO_2," J. Am. Ceram. Soc., 7, 238,410 (1924).

Bowen, N. L., Greig, j. W. and Zies, E. G.,"Mullite, a Silicate of Alumina," J. Wash. Acad. Sci., 14, 183-191 (1924).

Brandt, J. and Lundberg, R., "Processing of Mullite-Based Long-Fibre Composites via Slurry Routes and by Oxidation of an Al-Si Alloy Powder," J. Eur. Ceram. Soc., 16, 261-267(1996).

Burnham, C. W., Crystal Structure of Mullite, Carnegie Inst. Washington Yearb. 63, 223-227 (1964).

Cameron, W.E., "Mullite: a substituted alumina," Am. Mineral., 62, 747-755 (1977).

Cannon, H. S. and Lenel, F. V. in Plansee Proceedings, Beresovsky, F. (editor), Metalwerk plansee, Reutee., 106 (1953).

Chiang, Y.-M., Haggerty, J. S., Messner, R. P. and Demetry, C., "Reaction-Based Processing Methods for Ceramic-Matrix Composites," Am. Ceram. Soc. Bull., 68, 420-428 (1989).

Claussen, N. and Jahn, J., " Mechanical Properties of Sintered, In Situ Reacted Mullite-Zirconia Composites," J. Am. Ceram. Soc., 63, 228-229 (1980).

Claussen, N. and Wu, S., "Processing and Properties of Reaction-Bonded Al_2O_3 (RBAO) and Mullite Composites," Ceramic Transactions, Ceramic Powder Sci. IV, 631-645 (1991).

Claussen, N., Janssen, R. and Holz, D., "Reaction Bonding of Aluminum Oxide (RBAO)," J. Ceram. Soc. Jpn., 103, 749-758 (1995).

Claussen, N., Le, T. and Wu, S., "Low-Shrinkage Reaction-Bonded Alumina," J. Eur. Ceram. Soc., 5, 29-35 (1989).

Claussen, N., Travitzky, A. J. and Wu, S., "Tailoring of Reaction-Bonded Al_2O_3 (RBAO) Ceramics," Ceram. Eng. Sci. Proc., 11, 806-820 (1990).

Claussen, N., Wu, S. and Holz, D., "Reaction Bonding of Aluminum Oxide (RBAO) Composites: Processing, Reaction Mechanisms, and Properties," 14, 97-109 (1994).

Coble, R. L., "Reactive Sintering," Sintering-Teeory and Practice, Kolar, D., Pejovnik, S. and Ristic, M. M. (Eds.), Elsevier Scientific, Amsterdam, Netherlands, 145-151 (1982).

Coble, R. L., "Sintering Crystalline Solids. I. Intermediate and Final State Diffusion Models," J. Appl. Phy., 32, 787-792 (1961).

Davis, R. F. and Pask, J. A., "Diffusion and Reaction Studies in the System Al_2O_3-SiO_2," J. Am. Ceram. Soc., 55, 525-531 (1972).

De Keyser, W. L., "Reactions at the Point of Contact Between SiO_2 and Al_2O_3," in Science of Ceramics, Vol.2, Edited by Stewart, G. H., Academic Press, Inc., New York, 243-257 (1965).

De Portu, G. and Henney, J. W., "The Microstructure and Mechanical Properties of Mullite-Zirconia Composites," Br, Ceram. Trans. J., 83, 69-72 (1984).

Deal, B.E. and Grove, A. S., "General Relationship for the Thermal Oxidation of Silicon," J. Appl. Phy., 36, 3770-3778 (1965).

Derjaguin, B., "Concerning the Paper: 'The Effect of Capillary Liquid on the Force of Adhesion between Spherical Solid Particles," J. Colloid Interface Sci., 26, 253 (1968).

Di Rupo, E. I. and Anseau, M. R., "Solid State Reactions in the ZrO_2-SiO_2-Al2O_3 System," J. Mater. Sci., 15, 114-118 (1980).

Emi, H., Endo, S., Kanaoka, C. and Kawai, S., "Measurement of Forces due to a Liquid Bridge between Spherical Solid Particles," Int. Chem. Eng., 19, 300-306 (1979).

Evans, U. R., "Velocity of Film-Growth," The Corrosion and Oxidation of Metals, Edward Arnold and Company, London, 819-859 (1960).

Evans, U. R., Trans. Electrochem. Soc.,46, 247 (1924).

Frischat, G. H., "Ionic Diffusion in Oxide Glasses," Trans Tech Publications, Germany, 1975.

German, R. L., "Liquid Phase Sintering," Plenum Press, NY (1985).

German, R. L., "Sintering Teory and Practice," John Wiley and Sons Inc., NY (1996).

Gillespie, T. and Settineri, W. J., "The Effect of Capillary Liquid on the Force of Adhesion between Spherical Solid Particles," J. Colloid and Interface Sci. 24, 199-202 (1967)

Göring, J. and Schneider, H., "Creep and Subcritical Crack Growth of Nextel 720 Aluminosilicate Fibers As Received and after Heat Treatment at 1300 °C," Ceram. Eng. Sci. Proc., 18, 95-102 (1997).

Haggerty, J. S. and Chiang, Y.-M., "Reaction-Based Processing Methods for Ceramics and Composites," Ceram. Eng. Sci. Proc., 11, 757-794 (1990).

Heady, R. B. and Cahn, J. W., "An Analysis of the Capillary Forces in Liquid-Phase Sintering of Spherical Particles," Metall. Trans., 1, 185-189 (1970).

Hoge, C. E. and Pask, J. A., "Thermodynamics of Solid State Sintering," Physics of Sintering, 5, 109-142 (1973).

Holz, D., Pagel, S., Bowen, C., Wu, S. and Claussen, N., "Fabrication of Low to Zero Shrinkage Reaction-Bonded Mullite Composites," J. Eur. Ceram. Soc., 16, 255-260 (1996).

Holz, D., Wu, S., Scheppokat, S. and Claussen, N., "Effect of Processing Parameter on Phase and Microstructure Evolution in RBAO Ceramics," J. Am. Ceram. Soc., 77, 2509-2517 (1994).

Ishibashi, N., Tahara, K., Kobayshi, H., Mitamura, T. and Akiba, T., "Effect of Metallic Salt Aditives on the Properties of Mullite Sintered Body," Extended Abstracts of Annual Meeting, The Ceram. Soc. Jpn., 2C48, 233 (1989)

Ismail, M. G. M. U. and Somiya, S., "Properties of Zirconia-Toughened Mullite Synthesized by the Sol-Gel Method," in Advances in Ceramics, Vol. 24, Science and

Technology of Zirconia III, Edited by Somiya, S., Yamamoto, N. and Yanagida, H., Am. Ceram. Soc., Westerville, OH, 119-125 (1988).

Jangg, G., "Amalgams from the Point of View of Powder Metallurgy and Sintering Technology," Powder Met, 7, 241-250 (1964).

Jorgensen, P. J., "Effect of an Electric Field on Silicon Oxidation," J. Chem. Phys. 37, 874-879 (1962).

Kamiaka, H., Yamagishi, C. and Asaumi, J., "Mechanical Properties and Microstructure of Mullite-SiC-ZrO_2 Particulate Composite," Ceramic Transactions, Vol. 6, Mullite and Mullite Matrix Composites., Edited by Somiya, S., Davis, R. F. and Pask, J. A., Am. Ceram. Soc. Westerville, OH, 509-518 (1990).

Kehl, W. and Fischmeister, H. F., "Liquid Phase Sintering of Al-Cu Compacts," Powder Met. 23, 113-119 (1980).

Kingery, W. D., "Densification during Sintering in the Presence of a Liquid Phase. I. Theory," J. Appl. Phy., 30, 301-310 (1959).

Klug, F. J., Prochazka, S. and Doremus, R. H., "Alumina-Silica Phase Diagram in the Mullite Region," J. Am. Ceram. Soc., 70, 750-759 (1987).

Kohno, T. and Koczak, M. J., "Sintering and Dimensional control of Mixed Elemental Bronze Powders," Prog. Powder Met., 38, 463-481 (1982).

Kooner, S., Westby W. S., C., Watson, M. A. and Farries P. M., "Processing of Nextel™ 720/Mullite Composition Composite using Electrophoretic Deposition," J. Eur. Ceram. Soc., 20, 631-38 (2000).

Koyama, T., Hayashi, S., Yasumori, A. and Okada, K., "Preparation and Characterization of Mullite-Zirconia Composites from Various Starting Materials," J. Eur. Ceram. Soc., 14, 295-302 (1994).

Kubota, Y., Yamamoto, S., Mori, T., Yamamura, H. and Mitamura, "Changes of Microstructure and High Temperature Strength of Ceramic Composite in the Mullite-ZrO_2-Al_2O_3 System Unsig an in-situ Reaction between Synthetic Zircon and Al_2O_3," J. Ceram. Soc. Jpn. Int. Ed., 102, 94-99 (1994).

Kuczynski, G. C., "Self Diffusion in the sintering of Metallic Particles," Trans. of AIME, 2, 169-177 (1949).

Kurihira, T., Horiuchi, M., Kuribayashi, A., Takeuchi, Y. and Wakabayashi, S., "Effict of Additives on the Sinterability of Mullite Ceramics for Insulating Substrates," Extended Abstracts of Annual Meeting, The Ceram. Soc. Jpn., 3b42, 486 (1989)

Lathabai, S., Hay, D. G., Wagner, F. and Claussen, N., "Reaction-Bonded Mullite/Zirconia Composites," J. Am. Ceram. Soc., 79, 248-256 (1996).

Lee, D. J. and German, R. M., "SIntering Behavior of Iron-Aluminum Powder Mixes," Inter. J. Powder Met. Powder Tech., 21, 9-21 (1985).

Lenel, F. V., Trans. Am. Inst. Mining Met. Engrs., 175, 878 (1948).

Leriche, A., Deletter, M. and Cambier, F., "Relations among Microstructure and Mechanical Properties in Reaction-Sintered Mullite-Zirconia Composites," in Advances in Ceramics, Vol. 24, Science and Technology of Zirconia III, Edited by Somiya, S., Yamamoto, N. and Yanagida, H., Am. Ceram. Soc., Westerville, OH, 1083-1089 (1988).

Ligenza, J. R. and Spitzer, W. G., J. Phys. Chem. Solids, 14, 131 (1960).

Mechnich, P., Schmücker, M., and Schneider, M., "Reaction Sequence and Micerstructural Development of CeO_2-Doped Reaction-Bonded Mullite," J. Am. Ceram. Soc., 82, 2517-22(1999).

Mechnich, P., Schneider, H., Schmücker, M., and Saruhan, B., "Accelerated Reaction Bonding of Mullite," J. Am. Ceram. Soc., 81, 1931-1937(1998).

Moya J. S. and Osendi, M. I., " Effect of ZrO_2 (ss) in Mullite on the Sintering and Mechanical Properties of Mullite/ZrO_2 composites," J. Mater. Sci. Lett., 2, 599-601 (1983).

Moya, J. S. and Osendi, M. I., "Microstructure and Mechanical Properties of Mullite/ZrO2 Composites," J. Mater. Sci., 19, 2909-2914 (1984).

Nakahira, A. and Niihara, K., "SIntering Behaviorsand Consolidation Process for Al_2O_3/SiC nanocomposites," J. Ceram. Soc. Jpn. Int. Edt., 100, 448-463 (1992).

Neretnieks, I., Abelin, H., Birgersson, L., Moreno, L., Rasmuson, A. and Skagius, K., "Chemical Tansport in Fractured Rock," in Advances in Transport Phenomena in Porous Media, Edited by Bear, J. and Corapcioglu, Y., Dordrecht, Martnus Nijhoff Publishers, P518-523 (1987).

Nextel, 3M, Ceramic Fiber Technical Notebook, 1997

Orange, G., Fantozzi, G., Cambier, F., Leblud, C., Anseau, M. R. and Leriche, A., "High Temperature Mechanical Properties of Reaction-Sintered Mullite/Zirconia and Mullite/Alumina/Zirconia Composites," J. Mater. Sci., 20, 2533-2540 (1985).

Oschartz and Wächter (1847) cited in: Litzow, K. Keramische Technik. Vom Irdengut zum Porzellan. Callwey, Munich (1984).

Peissker, E., "Pressing and Sintering Characteristics of Powder Mixtures for Sintered Bronze 90/10 Containing Diffedrent Amounts of Free Tin," Modern Developments in Powder Metallurgy, Hausner, H. H. and Smith, W. E. (editers), Metal Powder Industries Federation, Princeton, NJ, 7, 597-614 (1974).

Pena, P., Moya, J. S., De Aza, S., Cardinal, E., Cambier, F., Leblud, C. and Anseau, M. R., "Effect of Magnesia Additions on the Reaction Sintering of Zircon-Alumina Mixtures to Produce Zirconia Toughened Mullite," J. Mater. Sci. Lett., 2, 772-774 (1983).

Petry, M. D. and Mah, T., "The effect of Thermal exposures on the Strengths of Nextel™ 550 and 720 Filaments," J. Am. Ceram. Soc., 82, 2801-2807(1999).

Princen, H. M., "Comments on 'The efffect of Capillary Liquid on the Force of Adhesion between Spherical Solid Particles," J. Colloid Interface Sci., 26, 249-253 (1968)

Pliskin, W. A. and Gnall, R. P., "Evidence for Oxidation Growth at the Oxide-Silicon Interface from Controlled Etch Studies," J. Electrochem. Soc. 111, 872-874 (1964).

Prochazka, S. and Klug, F. J.,"Infrared Transparent Mullite Ceramic," J. Am. Ceram. Soc., 66, 874-880 (1983).

Prochazka, S., Wallace, J. S. and Claussen, N., "Microstructure of Sintered Mullite-Zirconia Composites," J Am. Ceram. Soc., 66, C125-C127 (1983).

Rincon, J. M., Dinger, T. R., Thomas, G. Moya, J. S. and Osendi, M. I., " Microstructure of Mullite/ZrO_2 and Mullite/Al_2O_3/ZrO_2 Though Ceramic Composites," Acta Metall., 35, 1155-1179 (1987).

Rundgren, K., Elfving, P., Pompe, R., Lagerlöf, K. P. D. and Larsson, B., "Comparative Study of Sol-Gel Prepared Mullite and Mullite-ZrO_2 Composites With and Without Y_2O_3," Advances in Ceramics, Vol 24B, Science and Technology of Zirconia III., Edited

by Somiya, S., Yamamoto, N. and Yanagida, H., Am. Ceram. Soc., Westerville, OH, 1043-51 (1988).

Rundgren, K., Elfving, P., Tabata, H., Kanzaki, S. and Pompe, R., "Microstructures and Mechanical Properties of Mullite-Zirconia Composites Made from Inorganic Sols and Salts," Ceramic Transactions, Vol. 6, Mullite and Mullite Matrix Composites., Edited by Somiya, S., Davis, R. F. and Pask, J. A., Am. Ceram. Soc. Westerville, OH, 553-566 (1990).

Saalfeld, H., "A modification of Al_2O_3 with sillimanite structure. In: Transactions VIIIth International Ceramic Congress, Copenhagen, 71-74 (1962).

Saruhan, B., Luxem, W. and Schneider H., "Preliminary Results on a Novel Fabrication Route for α–Al_2O_3 Single Crystal Monofilament-Reinforced Reaction-Bonded Mullite(RBM)," J. Eur. Ceram. Soc., 16, 269-273 (1996).

Scheppokat, S., Janssen, R. and Claussen, N., "In-Situ Synthesis of Mullite-A Route to Zero Shrinkage," Am. Ceram. Soc. Bull., 78, 67-69 (1998).

Scheppokat, S., Janssen, R. and Claussen, N., "Phase Development and Shrinkage of Reaction-Bonded Mullite Composites with Silicon Carbide of Different Particle Sizes," J. Am. Ceram. Soc., 82, 319-324 (1999).

Schneider, H., "Transition Metal Distribution in Mullite," Ceramic Transactions, Vol. 6, Mullite and Mullite Matrix Composites., Edited by Somiya, S., Davis, R. F. and Pask, J. A., Am. Ceram. Soc. Westerville, OH, 135-157 (1990).

Schneider, H., Okada, H. and Pask, J. A., "Mullite and Mullite Ceramics," Wiley, Chichester, U.K., 1994.

She, J. H., Schneider, H., Inoue, T., Suzuki, M., Sodeoka, S. and Ueno, K., "Fabrication of Low Shrinkage Reaction-Bonded Alumina-Mullite Composites," Mat. Chem. and Phy., 68, 105-109 (2001).

Shepherd, E. S., Rankin, G. A. and Wright, W., "The Binary System of Aluminum and Silica, Lime and Magnesia," Am. J. Sci., 28[166], 293-333 (1909).

Shiga, H., Ismail, M. G. M. U. and Katayama, K., "Sintering of ZrO_2 Toughened Mullite Ceramics and Its Microstructure," J. Ceram. Soc. Jpn., Int. Ed., 99, 782-786 (1991).

Srikrishna, K., Thomas, G. and Moya, J. S., "Sintering Additives for Mullite/Zirconia Composites," in Advances in Ceramics, Vol. 24, Science and Technology of Zirconia III, Edited by Somiya, S., Yamamoto, N. and Yanagida, H., Am. Ceram. Soc., Westerville, OH, 276-286 (1988).

Staley, Jr., W. G. and Brindley, G. W., "Development of Noncrystalline Material in Subsolidus Reactions Between Silica and Alumina," J. Am. Ceram. Soc., 52, 616-619 (1969).

Stearns, L. C., Zhao, J. and Harmer, M. P., "Processing and Microstructure development in Al_2O_3-SiC 'Nanocomposites'," J. Eur. Ceram. Soc., 10, 473-477 (1992).

Vernadsky, W. I. (1890) cited in Pask, J. A., "Critical review of phase equilibria in the Al_2O_3-SiO_2 system," Ceram. Trans. 6, 1-13 (1990).

Wallace, J. S., Petzow, G. and Claussen, N., " Microstructure and Property Development in In-Situ-Reacted Mullite-ZrO_2 Composites," in Advances in Ceramics, Vol. 12, Science and Technology of Zirconia. Edited by Claussen, N., Ruhle, M. and Heuer, A. H., Am. Ceram. Soc., Westerville, OH, 436-442 (1984).

Westby, W. S., Kooner, S., Farries, P. M., Brother P. and Shatwell, R. A., "Processing of Nextel 720/Mullite Composition Composite using Electrophoretic Deposition," J. Mat. Sci., 34, 5021-5031(1999).

Wilson, D. M., "Statistical Tensile Strength of Nextel™ 610 and Nextel™ 720 Fibres," J. Mater. Sci., 32, 2535-2542 (1997).

Wilson, D. M., Lieder, S. L. and Luenebureg, D. C., "Microstructure and High Temperature Properties of Nextel 720 Fibres," Ceram. Eng. Sci. Proc. 16, 1005-1014 (1995).

Wu, S. and Claussen, N., "Fabrication and Properties fo Low-Shrinkage Reaction-Bonded Mullite," J. Am. Ceram. Soc., 74, 2460-2463 (1991).

Wu, S. and Claussen, N., "Reaction Bonding and Mechanical Properties of Mullite/Silicon Carbide Composites," J. Am. Ceram. Soc., 77, 2898-2904 (1994).

Wu, S. and Claussen, N., "Reaction-Bonding of ZrO_2-Containing Al_2O_3," in Solid State Phenomena, Vol. 25 and 26, edited by Chaklader, A. C. D. and Lund, J. A. (1992).

Wu, S., Gesing, A. J., Travitzky, N. A. and Claussen, N., "Fabrication and Properties of Al-infiltrated RBAO-based Composites," J. Eur. Ceram. Soc., 7, 277-281 (1991).

Wu, S., Holz, D. and Claussen, N., "Mechanism and Kinetics of Reaction-Bonded Aluminum Oxide Ceramics," J. Am. Ceram. Soc., 76, 970-980 (1993).

Yaroshenko, V. and Wilkinson D. S., "Sintering and Microstructure Modification of Mullite/Zirconia Composites Derived from Silica-Coated Alumina Powders," J. Am. Ceram. Soc., 84, 850-880 (2001)

APPENDIX

Appendix A

```
Si + O2 = SiO2
(T,P,S1)(T,P,G)(T,P,S6)
                    Units: T(K), P(atm), Energy(J), Mass(mole)
*******************************************************************************
      T          P        Delta H      Delta G     Delta V     Delta S     Delta Cp
     (K)        (atm)       (J)          (J)         (l)       (J  /K)       (J)
*******************************************************************************
* 1 * 0
   5526.65  1.0000E+00   -851169.3          0.0 -0.453E+03   -154.012       9.648
1423 1
   1423.00  1.0000E+00   -899033.9    -657610.2 -0.117E+03   -169.658       7.993
```

Appendix B

```
                                                          McMaster University - LAN
3 Al2O3 + 1.949491 Si + 1.949491 O2              =
(298.15K,1ATM,S4) (298.15K,1ATM,S1) (298.15K,1ATM,G)

   0.00000      mol    (  0.15257E-08      SiO
                      +  0.63234E-09      O2
                      +  0.26099E-09      O
                      +  0.27072E-15      AlO
                      +  0.93493E-17      Al
                      +  0.37940E-18      AlO2
                      +  0.60391E-19      Si
                      +  0.46173E-21      Al2O
                      +  0.41969E-21      (AlO)2
                      +  0.76761E-22      O3)
                         ( 1573.00 K, 1.0000     atm, gas_ideal, a=0.24190E-08)

+   4.9495       mol    (  0.60612          Al2O3
                      +  0.39388          SiO2)
                         ( 1573.00 K, 1.0000     atm, Mullite)

                      +  0.00000     mol  Al6Si2O13
                         ( 1573.00 K, 1.0000     atm, S1, a=0.97312    )

                      +  0.00000     mol  Al2O3
                         ( 1573.00 K, 1.0000     atm, S4, a=0.70611    )

                      +  0.00000     mol  SiO2
                         ( 1573.00 K, 1.0000     atm, S4, a=0.68154    )

                      +  0.00000     mol  SiO2
                         ( 1573.00 K, 1.0000     atm, S6, a=0.68099    )

                      +  0.00000     mol  SiO2
                         ( 1573.00 K, 1.0000     atm, S2, a=0.63869    )

                      +  0.00000     mol  Al2SiO5
                         ( 1573.00 K, 1.0000     atm, S2, a=0.54292    )

                      +  0.00000     mol  Al2O3
                         ( 1573.00 K, 1.0000     atm, S2, a=0.47390    )

                      +  0.00000     mol  Al2SiO5
                         ( 1573.00 K, 1.0000     atm, S1, a=0.47199    )

                      +  0.00000     mol  Al2O3
                         ( 1573.00 K, 1.0000     atm, S3, a=0.44787    )

                      +  0.00000     mol  Al2O3
                         ( 1573.00 K, 1.0000     atm, S1, a=0.33452    )

                      +  0.00000     mol  SiO2
                         ( 1573.00 K, 1.0000     atm, S7, a=0.30097    )

                      +  0.00000     mol  Al2SiO5
                         ( 1573.00 K, 1.0000     atm, S3, a=0.23838    )

                      +  0.00000     mol  SiO2                          T
```

```
                    ( 1573.00 K, 1.0000     atm, S1, a=0.16594    )

                +   0.00000     mol  SiO2                              T
                    ( 1573.00 K, 1.0000     atm, S5, a=0.20650E-01)

                +   0.00000     mol  SiO2                              T
                    ( 1573.00 K, 1.0000     atm, S3, a=0.45379E-02)

                +   0.00000     mol  SiO2
                    ( 1573.00 K, 1.0000     atm, S8, a=0.37851E-02)

                +   0.00000     mol  (Al2O3)(SiO2)2
                    ( 1573.00 K, 1.0000     atm, S1, a=0.69507E-09)

                +   0.00000     mol  Si
                    ( 1573.00 K, 1.0000     atm, S1, a=0.10927E-11)

                +   0.00000     mol  Al                                T
                    ( 1573.00 K, 1.0000     atm, S1, a=0.13310E-12)

 The cutoff concentration has been specified to 1.000E-30

 Data on  4 product species identified with "T" have been extrapolated

 ********************************************************************************
   DELTA H     DELTA G     DELTA V     DELTA S     DELTA U    DELTA Cp     PROD V
     (J)         (J)         (l)        (J/K)        (J)        (J/K)        (l)
 ********************************************************************************
 -S4---S1---G1-----------------------------------------------------------------
 -1.125E+06 -2.581E+06 -4.780E+01  4.485E+02 -1.120E+06  2.060E+02  0.000E+00
 ================================== last line ===================================
```

Appendix C

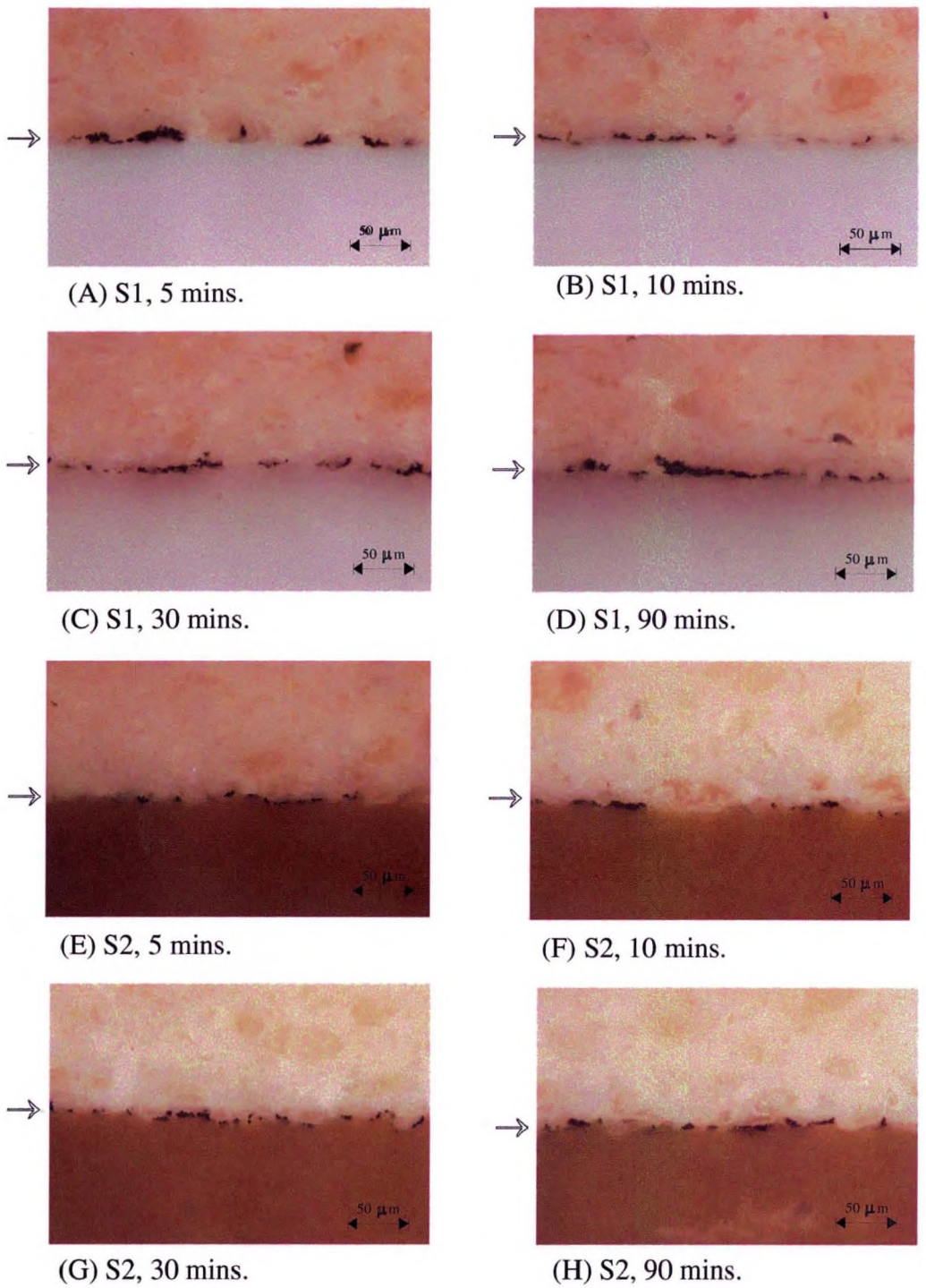

Fig. C-1. The reaction interface between eutectic composition (top) and Al_2O_3 + SiO_2 (S1) (bottom) or Al_2O_3 + Si (S2) (bottom) after heating at 1175 °C for indicated time (Diffusion layer arrowed).

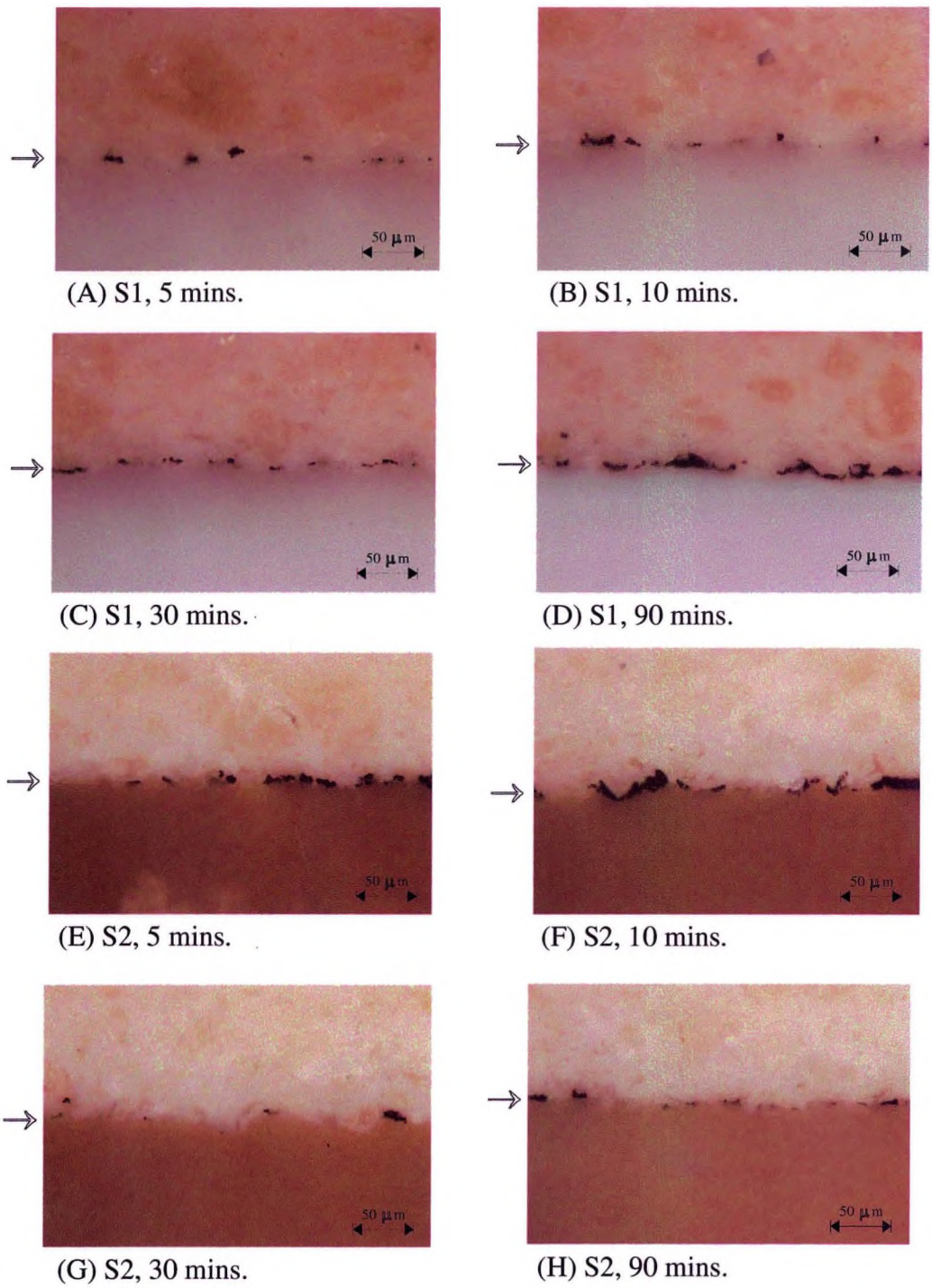

Fig. C-2.The reaction interface between eutectic composition (top) and $Al_2O_3 + SiO_2$ (S1) (bottom) or Al_2O_3 + Si (S2) (bottom) after heating at 1200 °C for indicated time (Diffusion layer arrowed).

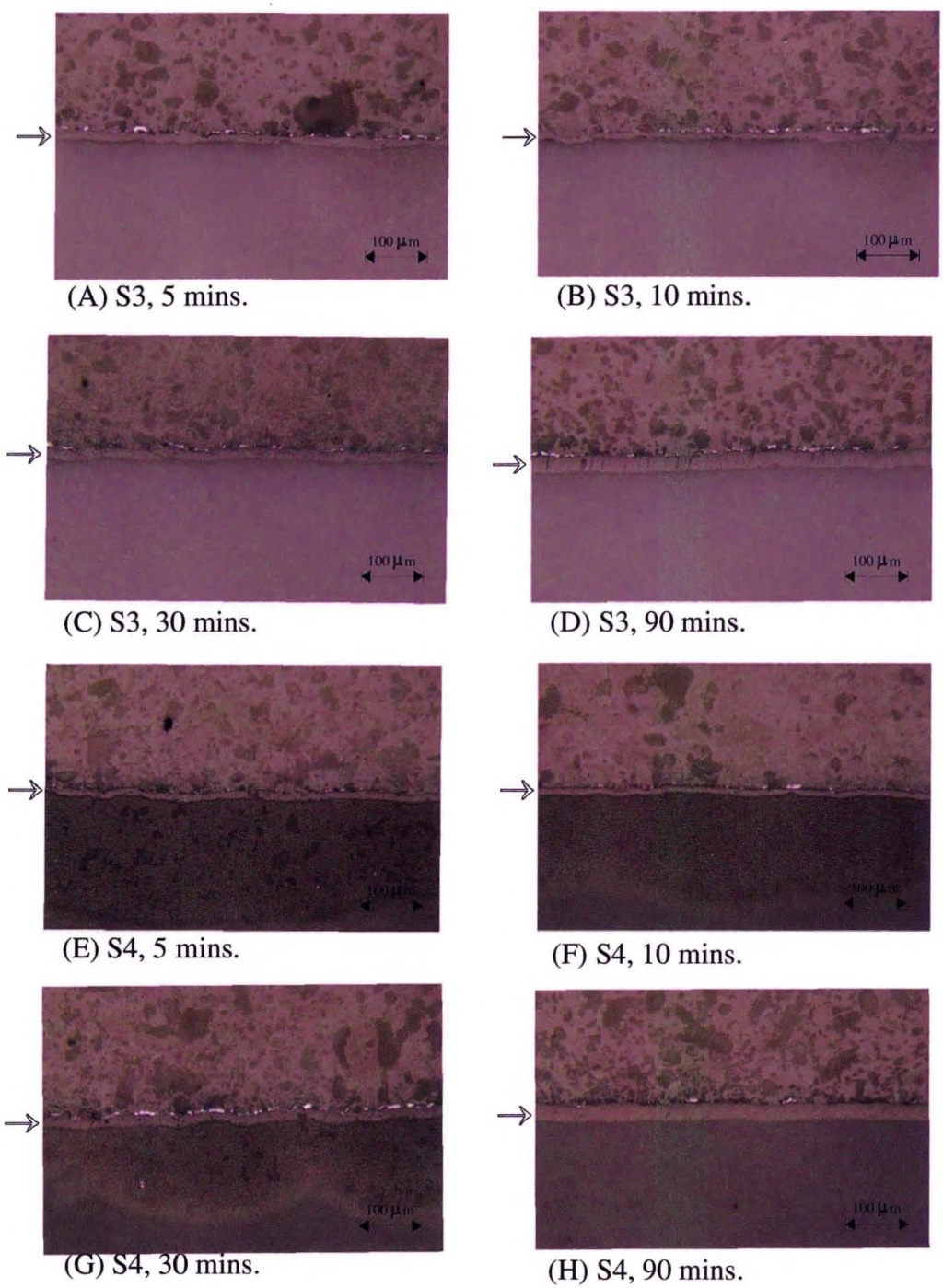

Fig. C-3.The reaction interface between eutectic composition (top) and Al_2O_3 + SiO_2 + seeds (S3) (bottom) or Al_2O_3 + Si + seeds (S4) (bottom) after heating at 1250°C for indicated time (Diffusion layer arrowed).

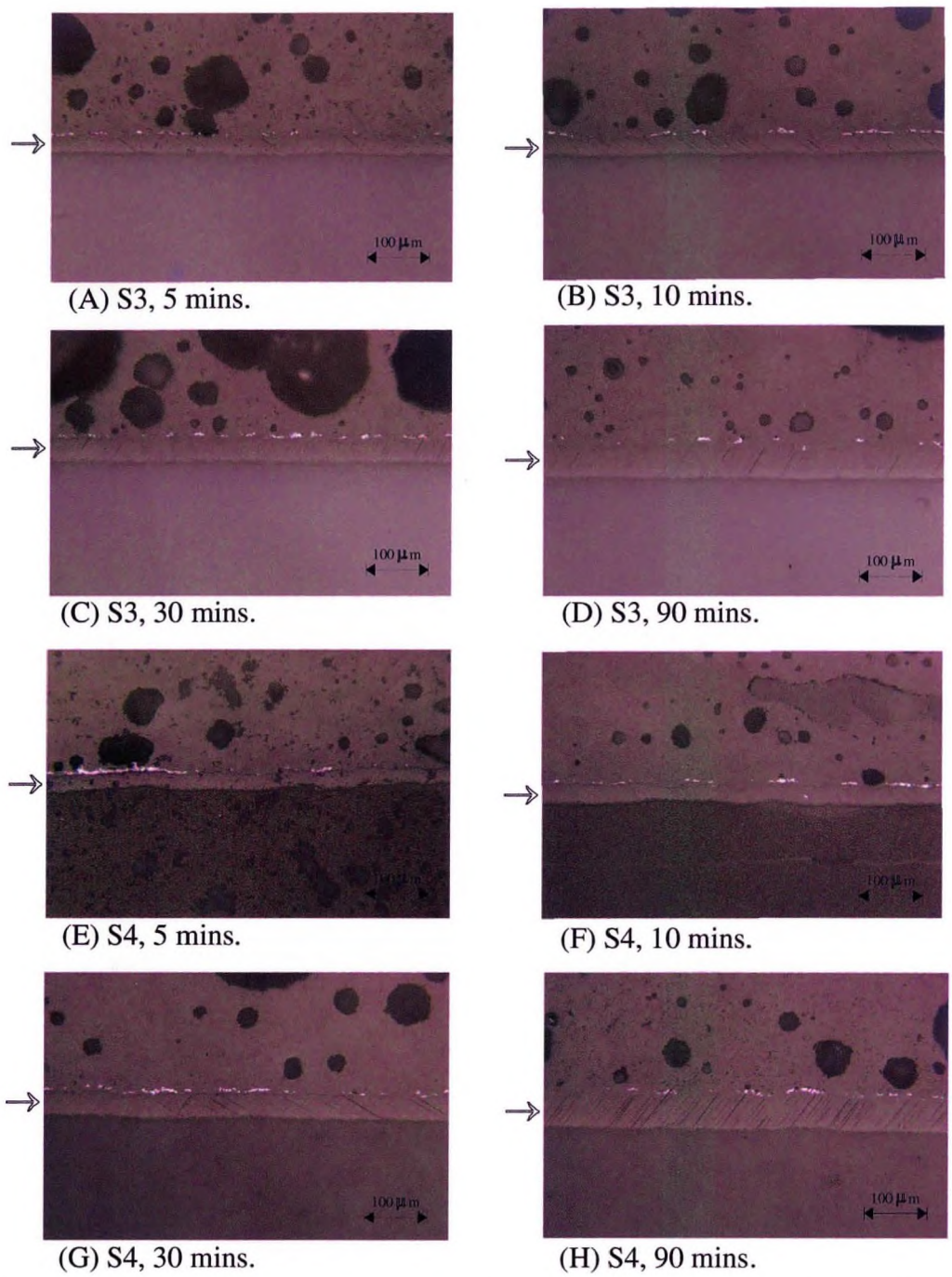

Fig. C-4.The reaction interface between eutectic composition (top) and Al_2O_3 + SiO_2 + seeds (S3) (bottom) or Al_2O_3 + Si + seeds (S4) (bottom) after heating at 1300 °C for indicated time (Diffusion layer arrowed).

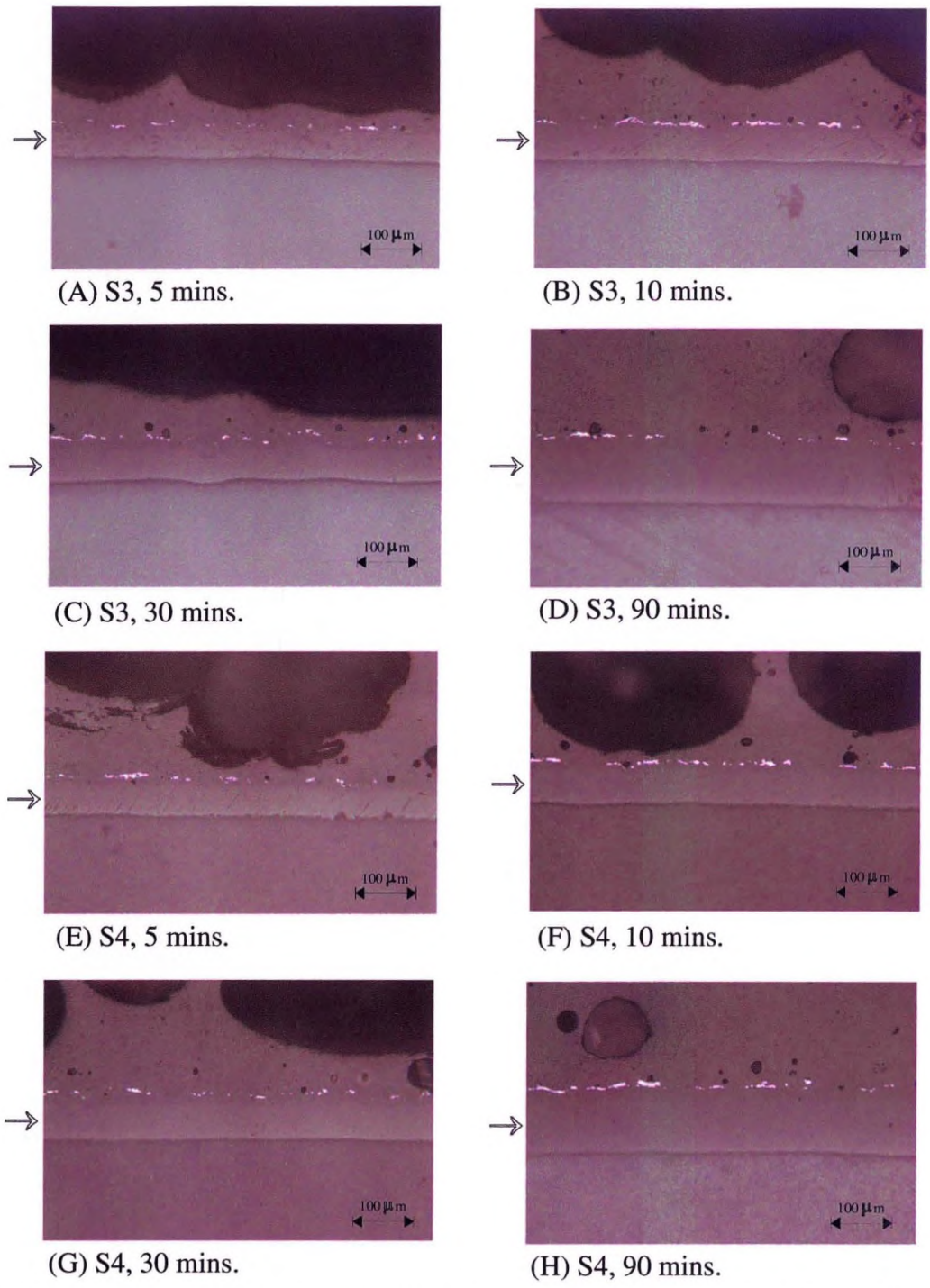

Fig. C-5.The reaction interface between eutectic composition (top) and Al_2O_3 + SiO_2 + seeds (S3) (bottom) or Al_2O_3 + Si + seeds (S4) (bottom) after heating at 1350 °C for indicated time (Diffusion layer arrowed).

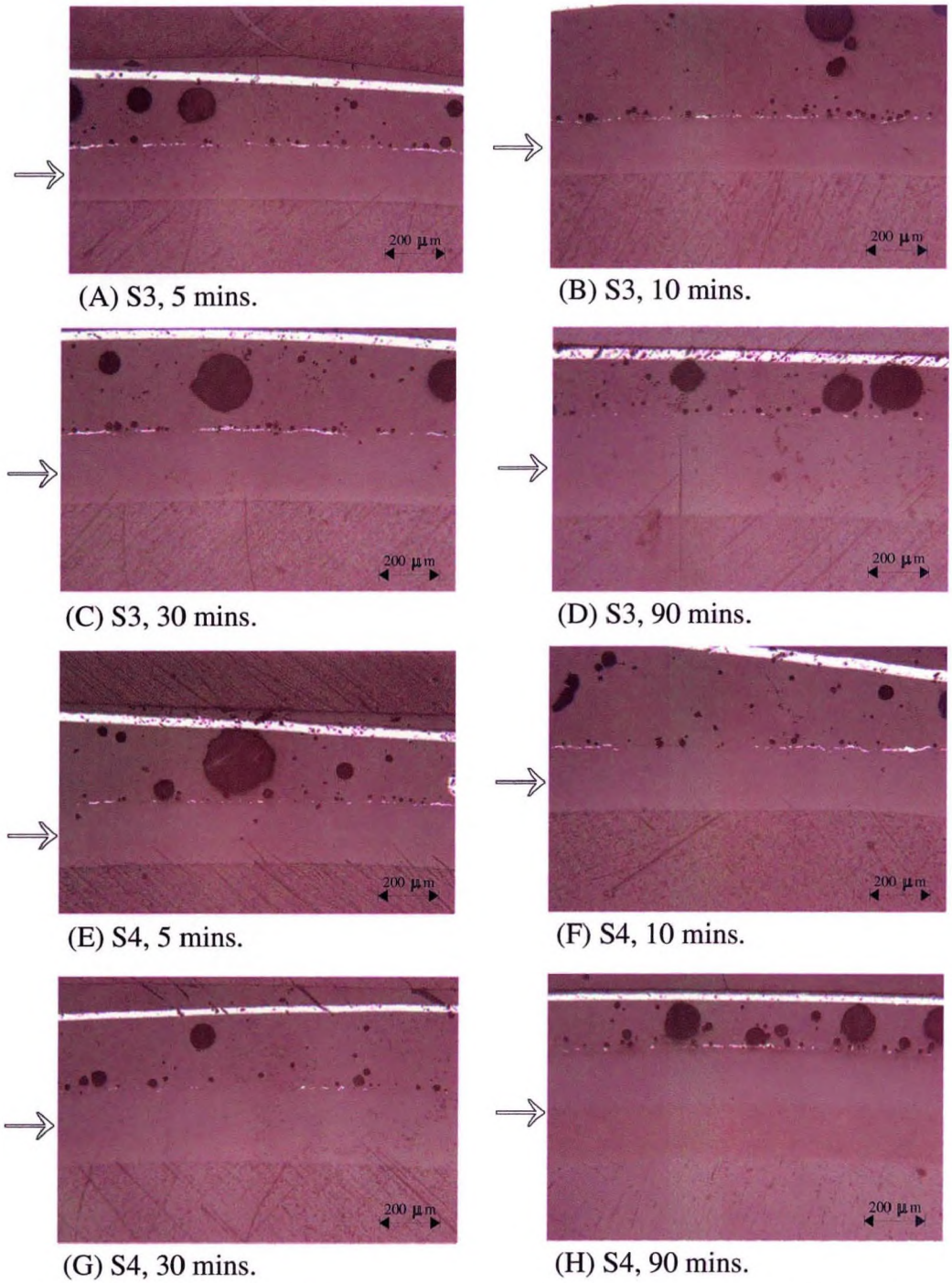

Fig. C-6.The reaction interface between eutectic composition (top) and Al_2O_3 + SiO_2 + seeds (S3) (bottom) or Al_2O_3 + Si + seeds (S4) (bottom) after heating at 1400 °C for indicated time (White line is Pt foil, Diffusion layer arrowed).